ANNALS OF THE UNIVERSITY OF CRAIOVA
ANNALES DE L'UNIVERSITÉ DE CRAIOVA

ANALELE UNIVERSITĂȚII DIN CRAIOVA

SERIA: INGINERIE ELECTRICĂ
SERIE: ELECTRICAL ENGINEERING
SÉRIE: INGÉNIERIE ÉLECTRIQUE
Anul/Year/Année 46
No. 46, Vol. 46, Issue 1, 2022

December 2022

ISSN 1842-4805 (print)
ISSN 2971-9852 (online)
ISSN-L 1842-4805

EDITURA UNIVERSITARIA

ANNALS OF THE UNIVERSITY OF CRAIOVA

13, A.I. Cuza Str., CRAIOVA 200585
ROMANIA

We exchange publications with similar institutions of country and from abroad

ANNALES DE L'UNIVERSITÉ DE CRAIOVA

Rue A.I. Cuza, No. 13, CRAIOVA 200585
ROUMANIE

On fait des échanges des publications avec les institutions similaires du pays et de l'étranger

---

This journal is published by the Faculty of Electrical Engineering from the University of Craiova.
The authors are fully responsible for the originality of their papers and for accuracy of their notes.

Editorial board

Prof.dr.ing. Ioan POPA – editor in chief, University of Craiova, Romania
Conf.dr.ing. Mircea DRIGHICIU – editor in chief, University of Craiova, Romania
Prof.dr.ing. Dan MIHAI, University of Craiova, Romania
Prof.dr.ing. Marian CIONTU, University of Craiova, Romania
Prof.dr.ing. Lucian MANDACHE, University of Craiova, Romania
Prof.dr.sc. Ivan YATCHEV, Technical University of Sofia, Bulgaria
Prof.dr.ing. Leszek CZARNECKI, Life Fellow IEEE, Louisiana State University, USA
Prof.dr.ing. Slavoljub ALEKSIC, University of Nic, Serbia
Prof.dr.ing. Sergey RYVKIN, Control Sciences Institute "V.I.Trapeznikov", Russia
Prof.dr.ing. Mihai IORDACHE, University "Politehnica" of Bucharest, Romania
Prof.dr.ing. Victor ŞONTEA, Technical University of Moldova, Moldova
Prof.dr.ing. Iuliu DELEŞEGA, University "Politehnica" of Timişoara, Romania
Prof.dr.ing. Dumitru-Marcel ISTRATE, "Gh. Asachi" Technical University of Iaşi, Romania
Prof.dr.ing. Miroslav PRSA, University of Novisad, Serbia
Prof.dr.ing. Maria BROJBOIU, University of Craiova, Romania
Prof.dr.ing. Mihai GAVRILAŞ, "Gh. Asachi" Technical University of Iaşi, Romania
Prof.dr.ing. Daniela DANCIU, University of Craiova, Romania
Prof.dr.ing. Nicolae MUNTEAN, University "Politehnica" of Timişoara, Romania
Prof.dr.ing. Călin MUNTEANU, Technical University of Cluj-Napoca, Romania
Prof.dr.ing. Leonardo-Geo MĂNESCU, University of Craiova, Romania
Prof.dr.ing. Camelia PETRESCU, "Gh. Asachi" Technical University of Iaşi, Romania
S.l.dr.ing. Ioana Gabriela SÎRBU, University of Craiova, Romania

REVIEWERS COMMITTEE

Lia-Elena ACIU – *Transilvania University of Braşov,* Romania
Maricel ADAM – *"Gh. Asachi" Technical University of Iaşi,* Romania
Mihaela ALBU – *University "Politehnica" of Bucharest,* Romania
Slavoljub ALEKSIC – *University of Nis,* Serbia
Horia BĂLAN – *Technical University of Cluj-Napoca,* Romania
Gheorghe BĂLUŢĂ – *"Gh. Asachi" Technical University of Iaşi*, Romania
Alexandru BITOLEANU – *University of Craiova, Romania*
Maria BROJBOIU – *University of Craiova,* Romania
Emil CAZACU – *University "Politehnica" of Bucharest,* Romania
Aurel CÂMPEANU – *University of Craiova,* Romania
Mihai CERNAT – *Transilvania University of Braşov,* Romania
Marian CIONTU – *University of Craiova,* Romania
Daniel Cristian CISMARU – *University of Craiova,* Romania
Grigore CIVIDJIAN – *University of Craiova,* Romania
Zlata CVETCOVIC – *University of Nis,* Serbia
Leszek CZARNECKI – *Louisiana State University*, USA
Daniela DANCIU – *University of Craiova,* Romania
Sonia DEGERATU – *University of Craiova,* Romania
Iuliu DELEŞEGA – *University "Politehnica" of Timişoara,* Romania
Silvia-Maria DIGĂ – *University of Craiova,* Romania
Peter DINEFF – *Technical University of Sofia,* Bulgaria
Radu DOBRESCU – *University "Politehnica" of Bucharest,* Romania
Mircea-Adrian DRIGHICIU – *University of Craiova,* Romania
Laurentiu Marius DUMITRAN – *University "Politehnica" of Bucharest,* Romania
Sorin ENACHE – *University of Craiova,* Romania
Virgiliu FIRETEANU – *University "Politehnica" of Bucharest,* Romania
Dan FLORICĂU – *University "Politehnica" of Bucharest,* Romania
Cristian FOŞALĂU – *"Gh. Asachi" Technical University of Iaşi*, Romania
Teodor Lucian GRIGORIE – *Military Technical Academy "Ferdinand I",* Romania
Mircea-Dan GUSA – *"Gh. Asachi" Technical University of Iaşi*, Romania
Stefan HĂRĂGUŞ – *University "Politehnica" of Timişoara,* Romania
Elena HELEREA – *Transilvania University of Braşov,* Romania
Eugen HNATIUC – *"Gh. Asachi" Technical University of Iaşi,* Romania
Kemal HOT – *Polytechnic of Zagreb,* Croaţia
Eugen IANCU – *University of Craiova,* Romania
Nathan IDA – *University of Akron,* USA
Maria IOANNIDES – *National Technical University of Athens,* Greece
Valentin IONIŢĂ – *University "Politehnica" of Bucharest,* Romania
Mihai IORDACHE – *University "Politehnica" of Bucharest,* Romania
Marcel ISTRATE – *"Gh. Asachi" Technical University of Iaşi*, Romania
Wilhelm KAPPEL – *National Research and Development Institute for Electrical Engineering (ICPE – CA) Bucharest,* Romania
Liviu KREINDLER – *University "Politehnica" of Bucharest,* Romania
Gheorghe LIVINŢ – *"Gh. Asachi" Technical University of Iaşi*, Romania
Dumitru Dorin LUCHACHE – *"Gh. Asachi" Technical University of Iaşi*, Romania
Lucian MANDACHE – *University of Craiova,* Romania
Gheorghe MANOLEA – *University of Craiova,* Romania
Andrei MARINESCU – *Romanian Academy of Technical Science, Craiova Branch,* Romania
Iliana MARINOVA – *Technical University of Sofia,* Bulgaria
Claudia MARTIŞ – *Technical University of Cluj-Napoca,* Romania

Ernest MATAGNE – *Université Catholique de Louvain,* Belgium
Leonardo-Geo MĂNESCU – *University of Craiova,* Romania
Dan MIHAI – *University of Craiova,* Romania
Alexandru MOREGA – *University "Politehnica" of Bucharest,* Romania
Mihaela MOREGA – *University "Politehnica" of Bucharest,* Romania
Nazih MOUBAYED – *Lebanese University,* Lebanon
Călin MUNTEANU – *Technical University of Cluj-Napoca,* Romania
Florin MUNTEANU – *"Gh. Asachi" Technical University of Iaşi,* Romania
Valentin NĂVRĂPESCU – *University "Politehnica" of Bucharest,* Romania
Mitică Iustinian NEACĂ – *University of Craiova,* Romania
Ciprian NEMEŞ – *"Gh. Asachi" Technical University of Iaşi*, Romania
Petre-Marian NICOLAE – *University of Craiova,* Romania
Dragoş NICULAE – *University "Politehnica" of Bucharest,* Romania
Petru NOTINGHER – *University "Politehnica" of Bucharest,* Romania
Teodor PANĂ – *Technical University of Cluj-Napoca,* Romania
Camelia PETRESCU – *"Gh. Asachi" Technical University of Iaşi*, Romania
Ioan POPA – *University of Craiova,* Romania
Dan POPESCU – *University of Craiova,* Romania
Daniela POPESCU – *University of Craiova,* Romania
Mihaela POPESCU – *University of Craiova,* Romania
Miroslav PRSA – *University of Novi-Sad,* Serbia
Mircea M. RĂDULESCU – *Technical University of Cluj Napoca,* Romania
Victoriţa RĂDULESCU – *University "Politehnica" of Bucharest,* Romania
Benoit ROBYNS – *Ecole des Hautes Etude d'Ingénieur de Lille,* France
Constantin ROTARU – *Military Technical Academy "Ferdinand I",* Romania
Alex RUDERMAN – *Elmo Motion Control Ltd,* USA
Sergey RYVKIN – *Trapeznikov Institute of Control Sciences,* Russia
Alexandru SĂLCEANU – *"Gh. Asachi" Technical University of Iaşi*, Romania
Cristina Gabriela SĂRĂCIN – *University "Politehnica" of Bucharest,* Romania
Constantin SĂRMAŞANU – *"Gh. Asachi" Technical University of Iaşi,* Romania
Dan SELIŞTEANU – *University of Craiova,* Romania
Victor ŞONTEA – *Technical University of Moldova,* Moldova
Alexandru STANCU – *"A.I. Cuza" University of Iaşi,* Romania
Viorel STOIAN – *University of Craiova,* Romania
Ryszard STRZELECKI – *University of Technology Gdansk,* Poland
Flavius-Dan ŞURIANU – *University "Politehnica" of Timişoara,* Romania
Lorand SZABO – *Technical University of Cluj-Napoca,* Romania
Radu-Adrian TÎRNOVAN – *Technical University of Cluj-Napoca,* Romania
Tiberiu TUDORACHE – *University "Politehnica" of Bucharest,* Romania
Raina TZENEVA – *Technical University of Sofia*, Bulgaria
Ioan VADAN – *Technical University of Cluj-Napoca*, Romania
Viorel VARVARA – *"Gh. Asachi" Technical University of Iaşi*, Romania
Ion VLAD – *University of Craiova*, Romania
Ivan YATCHEV – *Technical University of Sofia*, Bulgaria

CONTENTS

DOI: 10.52846/AUCEE.2022.01

Dynamic Processes of Electric Motors for Operating some Aircraft Equipment

Sorin Enache, Ion Vlad and Monica-Adela Enache
University of Craiova/Faculty of Electrical Engineering, Craiova, Romania, senache@em.ucv.ro

***Abstract* – In this paper are detailed some results obtained within a European program in the field of avionics. The objectives of the program and the implementation team are briefly presented. A number of technical details are provided regarding the electric motor used to steer an airplane's running gear: advantages, comparative densities between the motor used (HDD) and the competitive motors, cross-section of the used motor, winding scheme of the motor, motor scheme with partial short-circuit. The mathematical model of the motor is presented, Simulink scheme of a simulation program in case of using a voltage inverter and a series of simulations obtained with its help (MSMP supplied by a voltage inverter, transmission ratio 1000, inertia10000 Nm^2 and MSMP supplied by an inverter with prescribed currents, transmission ratio 1000, inertia 10000 Nm^2). The paper concludes with the conclusions obtained by conducting the research. It is mentioned that the following notable results were obtained: decrease with 30% of the production and maintenance costs, decrease with 10% of the airship weight, carrying out a drive with a probability to lose the functionality.**

Cuvinte cheie: *avionica, motor electric, model matematic, program Simulink, simulări.*

Keywords: *airplane, electric motor, mathematic model, Simulink program, simulations.*

I. INTRODUCTION

The problems developed in this paper are of great practical interest. They refer to the electrical operation of various systems in the equipment of aircraft [1], [2], [3], [4], [5].

A team from the University of Craiova, Faculty of Electrical Engineering, was part of the European project team STREP (Specific Target REsearch Project) DRESS - Distributed and Redundant Electro-mechanical nose wheel Steering System, no. 030841, team coordinated by Prof. eng. PhD Sergiu Ivanov [6].

This project was financed by the European Commission by the financing program PC6.

The project had thirteen partners; their surveys are presented in the following table [7].

The objectives of DRESS consisted in:

- study and validation of a redundant electromechanical actuator;

- study and validation of a control system based on a distributed architecture.

A special attention was paid to the shimmy phenomenon (new systems of oscillations damping by using an electromechanical system).

TABLE I.
PROJECT PARTICIPANTS

No.	Participant name	Country	Tasks
1	MESSIER-BUGATTI	FR	Management Specifications & assessments System architecture design Technology education
2	Saab Avionics	S	Actuator design, integration & validation
3	AIRBUS UK	UK	Specification Final tests
4	MESSIER-DOWTY	FR	Landing gear & test rig design Landing gear actuator integration & validation Shimmy damping analysis
5	INSA Toulouse	FR	Research & optimum design of actuator & complex test rig
6	UC Louvaine	B	Research & optimum design of power electronics
7	University of Craiova	RO	Research & optimum design of electric motors
8	Universite Alsace	FR	Research & optimum design of system control
9	Budapest UTE	H	Research & optimum design of distributet architecture Safety analysis
10	TTTech	A	Manufacture of RDC & power electronics prototype
11	Equip Aero	FR	Manufacture of mechanical parts for the prototype
12	Stridsberg PT	S	Manufacture electrical motor prototype
13	Institut of aviation	PL	Manufacture of dummy nose landing gear test rig

The electrical drive was preferred for the front alighting gear of the airships for replacing the classical variants, with a lot of drawbacks, variants consisting in an electro-hydraulic drive with pinion - cremaillere or push-pull system (for large airships).

The implementation of the electromechanical technology for the front alighting gear has a series of advantages [8]:

- the decrease of the total weight of the airships and of the time necessary for standing and maintenance;

- the decrease of the production and maintenance costs;

- the traffic improvement and the safety increase during the ground operation, even in conditions of poor visibility, up to the limit of zero visibility;

- possibility to integrate in a completely automatic future system of ground guidance.

The simulations validation has been made by means of some tests on a prototype.

The test was carried out on a testing stand with a simplified alighting gear, connected to the control system, stand carried out in the project.

The research collective of the University of Craiova was involved in three work packages (WorkPackages):

WP 340 - Shimmy damping control;

WP420 - Electric motor / power card technology study and modelling;

WP430 - Thermal analysis and modelling.

The researches carried out by this collective have been used by the work package WP410 (Power architectures studies/Actuator sizing), which finished the architecture and dimensioned the electromechanical system, as well as by the package WP710 (Modelling evaluation), which integrated the models of all subsystems (automatic control, power electronics, motor, mechanical demultiplier, alighting gear, airplane) for the simulation of the whole system of the airplane.

For driving the electromechanical system we studied, owing to the high density of delivered power, there has been chosen the variant of permanent-magnet synchronous motor.

From the multitude of variants of such motors, taking into account the previous experience of two partners (SAAB AB and Stridsberg Powertrain AB), the option was the motor produced by Stridsberg Powertrain AB type HDDb09N [9].

This motor is a special type of permanent-magnet synchronous motor, with independent phases, characterized, according to its producer, by a four-six times higher power density over the classical synchronous motors (Fig. 1).

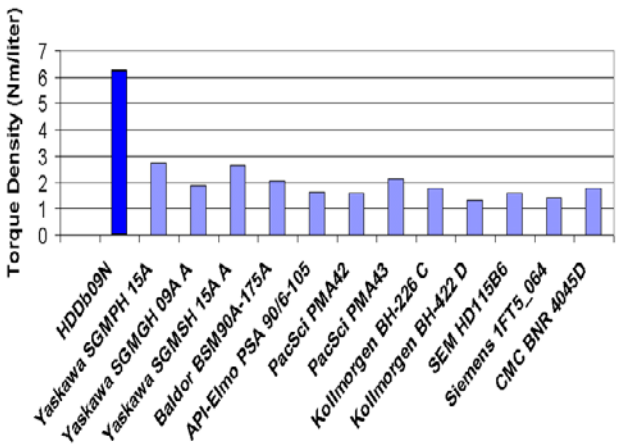

Fig. 1. Comparative densities between the motor used (HDD) and the competitive motors [2].

II. TECHNICAL DETAILS

From constructive point of view, the phase windings of the used motor does not coexist in the slots, so, on one hand, the phases are magnetically separated and, on the other hand, the solution redundance is improved (Fig. 2).

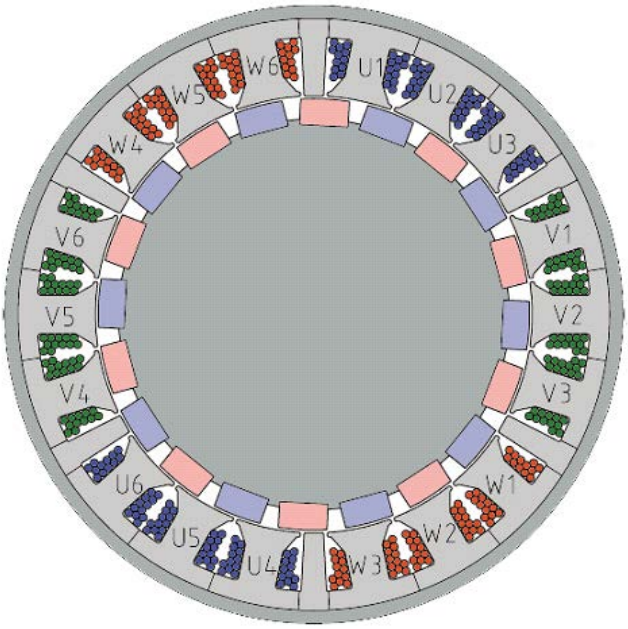

Fig. 2. Cross-section of the used motor [2].

In addition, it is equiped with six half-phases which are physically and magnetically separated and which can be each supplied to a bridge one-phase inverter (Fig. 3).

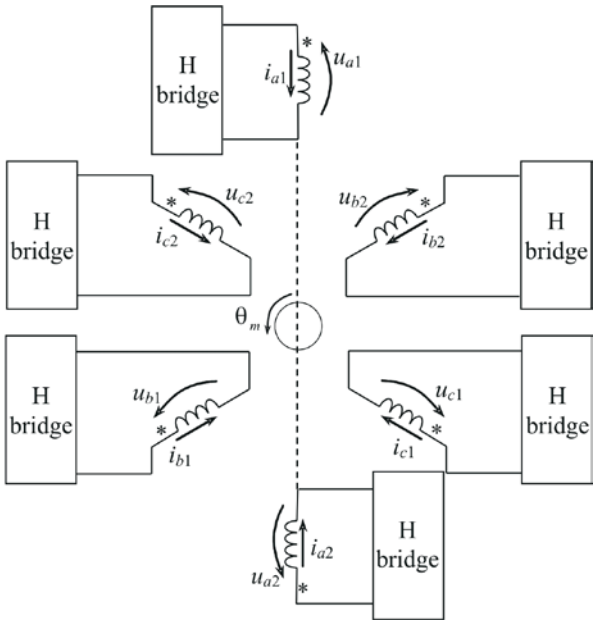

Fig. 3. Winding scheme of the motor [1].

As we can note, the motor model is obtained by concatenating two machines without mutual inductances between phases, with an angular displacement of 180°.

Among possible damages of the motor, there has been analyzed the case of the partial shortcircuit of a few turns.

In this case, the equivalent circuit is presented in the following figure.

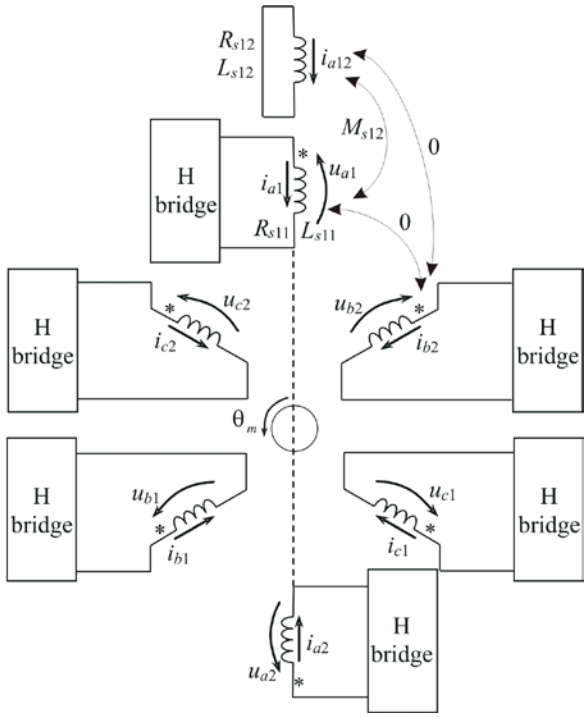

Fig. 4. Motor scheme with partial shortcircuit [6].

III. MOTOR EQUATIONS

The machine equations in this case, according to [9], become:

$$\begin{bmatrix} u_{a1} \\ u_{c2} \\ u_{b1} \\ u_{a2} \\ u_{c1} \\ u_{b2} \\ 0 \end{bmatrix} = [\mathbf{R}] \begin{bmatrix} i_{a1} \\ i_{c2} \\ i_{b1} \\ i_{a2} \\ i_{c1} \\ i_{b2} \\ i_{a12} \end{bmatrix} + [\mathbf{L}] \frac{d}{dt} \begin{bmatrix} i_{a1} \\ i_{c2} \\ i_{b1} \\ i_{a2} \\ i_{c1} \\ i_{b2} \\ i_{a12} \end{bmatrix} + \tag{1}$$

$$+K_T \dot{\theta}_m \begin{bmatrix} 0 \\ -\sin\left(P\theta_m - \frac{\pi}{3}\right) \\ -\sin\left(P\theta_m - \frac{2\pi}{3}\right) \\ -\sin\left(P\theta_m - \pi\right) \\ -\sin\left(P\theta_m - \frac{4\pi}{3}\right) \\ -\sin\left(P\theta_m - \frac{5\pi}{3}\right) \\ 0 \end{bmatrix} + \dot{\theta}_m \begin{bmatrix} K_{T11}\left(-\sin P\theta_m\right) \\ 0 \\ 0 \\ 0 \\ 0 \\ 0 \\ K_{T12}\left(-\sin P\theta_m\right) \end{bmatrix}$$

where:

$$[\mathbf{R}] = \begin{bmatrix} R_{s11} & 0 & 0 & 0 & 0 & 0 & 0 \\ 0 & R_s & 0 & 0 & 0 & 0 & 0 \\ 0 & 0 & R_s & 0 & 0 & 0 & 0 \\ 0 & 0 & 0 & R_s & 0 & 0 & 0 \\ 0 & 0 & 0 & 0 & R_s & 0 & 0 \\ 0 & 0 & 0 & 0 & 0 & R_s & 0 \\ 0 & 0 & 0 & 0 & 0 & 0 & R_{s12} \end{bmatrix} \tag{2}$$

$$[\mathbf{L}] = \begin{bmatrix} L_{s11} & 0 & 0 & 0 & 0 & 0 & M_{s12} \\ 0 & L_s & 0 & 0 & 0 & 0 & 0 \\ 0 & 0 & L_s & 0 & 0 & 0 & 0 \\ 0 & 0 & 0 & L_s & 0 & 0 & 0 \\ 0 & 0 & 0 & 0 & L_s & 0 & 0 \\ 0 & 0 & 0 & 0 & 0 & L_s & 0 \\ M_{s12} & 0 & 0 & 0 & 0 & 0 & L_{s12} \end{bmatrix} \tag{3}$$

The notations used are the classic ones used for supply voltages, currents through equivalent windings and motor parameters.

The electromagnetic torque expression is:

$$T_{em} = -K_T \left(i_{c2} \sin\left(P\theta_m - \frac{\pi}{3}\right) + i_{b1} \sin\left(P\theta_m - \frac{2\pi}{3}\right) + \right.$$
$$\left. + i_{a2} \sin\left(P\theta_m - \pi\right) + i_{c1} \sin\left(P\theta_m - \frac{4\pi}{3}\right) + i_{b2} \sin\left(P\theta_m - \frac{5\pi}{3}\right) \right) +$$
$$+ K_{T11}\left(-i_{a1} \sin P\theta_m\right) + K_{T12}\left(-i_{a12} \sin P\theta_m\right). \tag{4}$$

As we can note, the motor can also be used as three-phase machines without star connection of the phases, its supply being ensured by three one-phase inverters, bridge or star, supplied to a three-phase inverter.

IV. SIMULINK PROGRAMS

The Matlab-Simulink [10] programs carried out in the frame of this project enable the simulation of several combinations motor-controller.

For each combination, there can be simulated different damages which could occur in different operation conditions.

For example, there is presented the Matlab-Simulink block scheme of a program for simulating the operation of such a motor (Fig. 5).

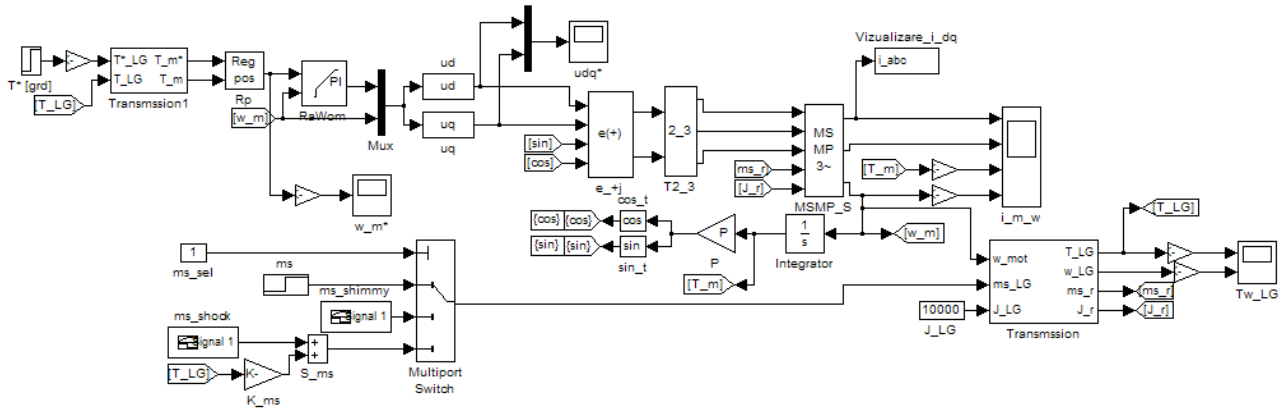

Fig. 5. Simulink scheme of a simulation program in case of using a voltage inverter [8].

V. SIMULATIONS

By means of such a progam, there have been obtained a series of simulations; a few of them are presented below, figures 6 and 7.

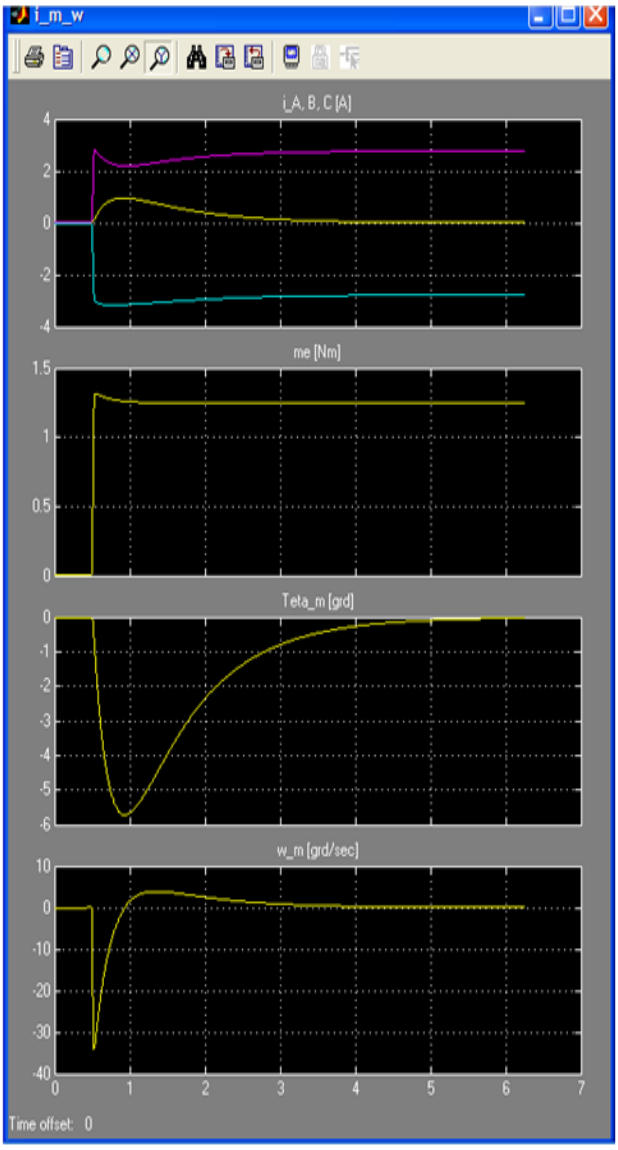

a)

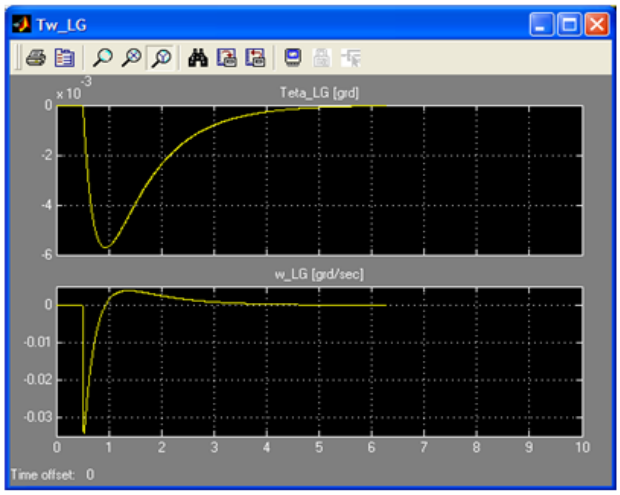

b)

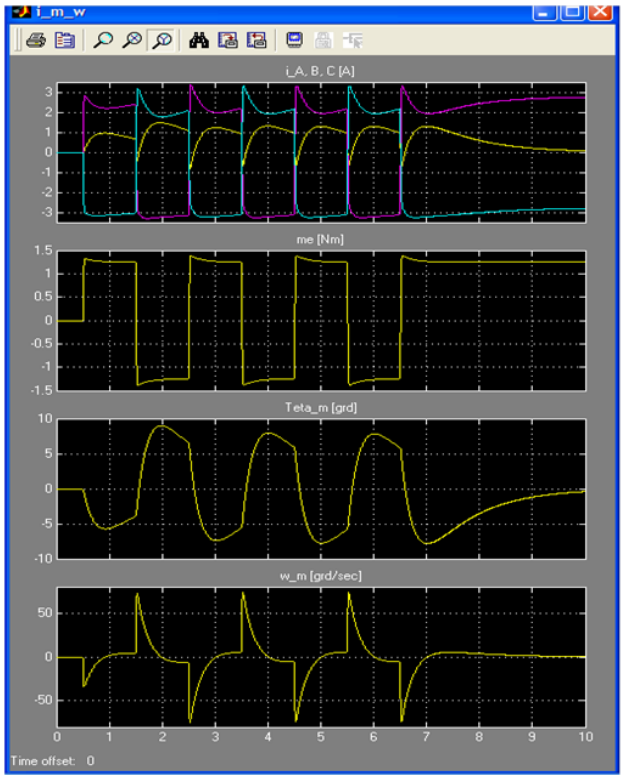

c)

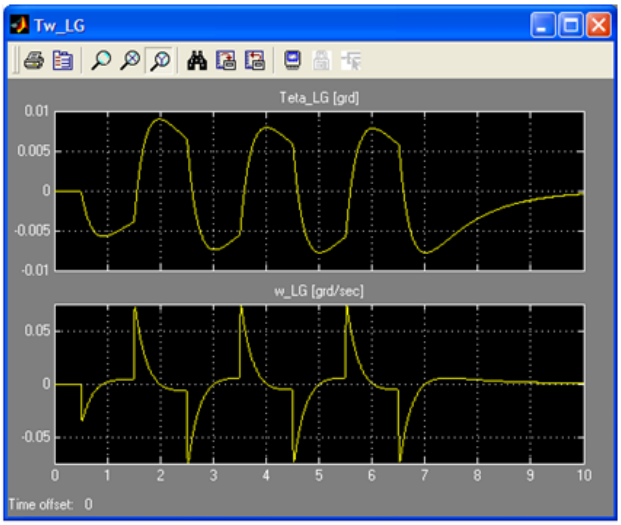

d)

Fig. 6. MSMP supplied by a voltage inverter, transmission ratio 1000, inertia10000 Nm^2.

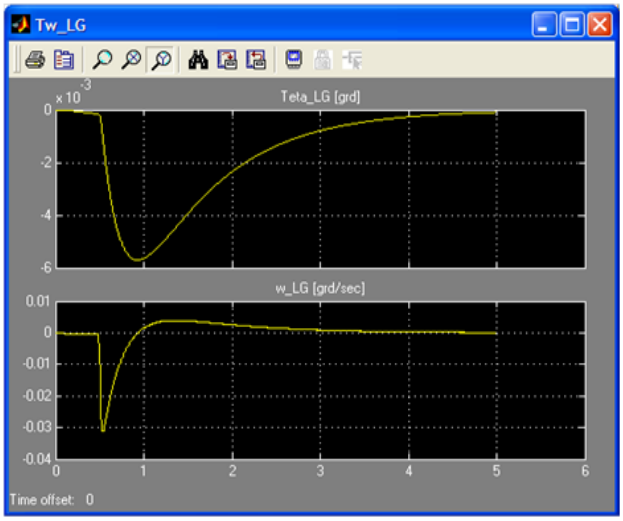

b)

Fig. 7. MSMP supplied by an inverter with prescribed currents, transmission ratio 1000, inertia 10000 Nm^2.

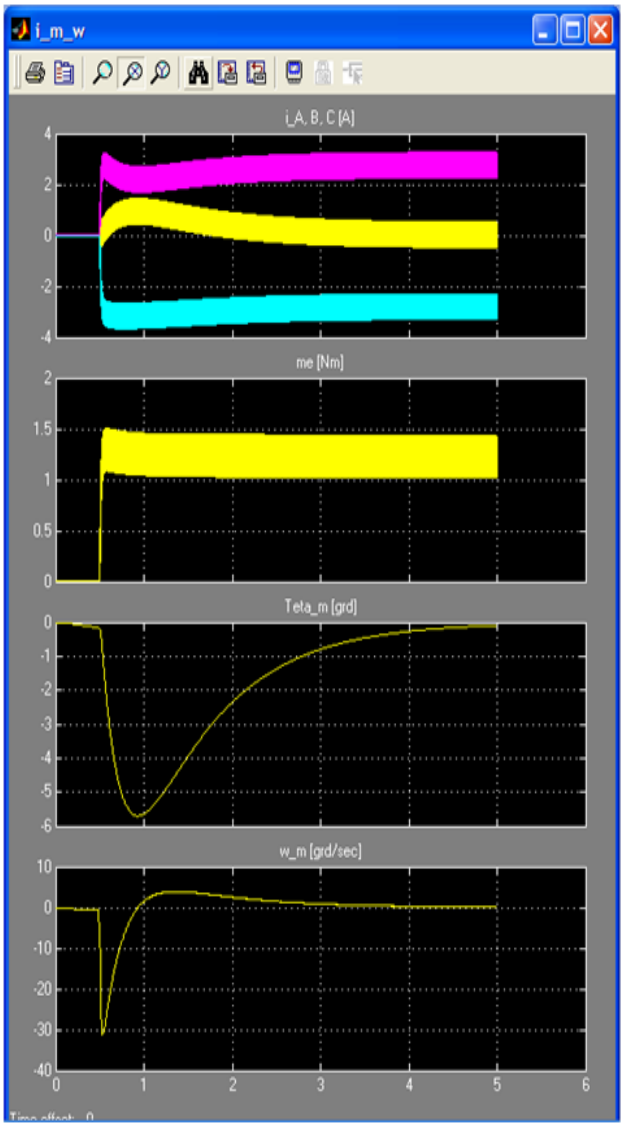

a)

These simulations were very useful finishing off the final variant, being obtained comparative results for a large variety of dimensions of motor, the optimum variant being chosen among them.

The project finality was a protype which was tested on the test stands of the project coordinator Messier-Bugatti [9].

VI. Conclusions

This paper presents some results obtained within a European project in which a team from the University of Craiova also took part.

Among the achievements of this program can be listed:

- decrease with 30% of the production and maintenance costs;

- decrease with 10% of the airship weight;

- carrying out a drive with a probability to lose the functionality.

Acknowledgment

Source of research funding in this article: Research program of the Faculty of Electrical Engineering financed by the PC6, STREP (Specific Target REsearch Project) DRESS - Distributed and Redundant Electro-mechanical nose wheel Steering System, no. 030841.

This paper was written as a tribute to Prof. eng. PhD Sergiu Ivanov.

Contribution of authors:
First author – 60%
First coauthor – 20%
Second coauthor – 20%.

Received on July 17, 2022
Editorial Approval on November 15, 2022

REFERENCES

[1] J. Benzaquen, J. He, B. Mirafzal, "Toward more electric powertrains in aircraft: Technical challenges and advancements", *CES Transactions on Electrical Machines and Systems*, Volume: 5, Issue: 3, Sept. 2021.

[2] H. Saini, N. Sandeep, A. Jakhar, A. K. Verma, "Design and Implementation of Five Level Inverter Topology for More Electric Aircraft Application", *2022 IEEE International Conference on Power Electronics*, Smart Grid, and Renewable Energy (PESGRE), Trivandrum, India, 2-5 Jan. 2022.g

[3] Z. Jiao, Z. Li, Y. Shang, S. Wu, Z. Song, Q. Pan, "Active Load Sensitive Electro-Hydrostatic Actuator on More Electric Aircraft: Concept, Design, and Control", *IEEE Transactions on Industrial Electronics*, Volume: 69, Issue: 5, 2022.

[4] J. Bird, "A Review of Electric Aircraft Drivetrain Motor Technology", *IEEE Transactions on Magnetics*, Volume: 58, Issue: 2, 2022.

[5] Q. Zhang, H. Zhang, "Research on control of electric propulsion permanent magnet synchronous motor of electric aircraft based on genetic algorithm", *2021 China Automation Congress (CAC)*, 22-24 Oct. 2021, Beijing, China, 2021.

[6] S. Ivanov, S. Enache s.a., "Project DRESS - Distributed and Redundant Electromechanical nose gear Steering System", PC6 STREP AST5-CT2006-030841, 2005-2008.

[7] S. Ivanov, S. Enache, "Distributed and redundant electro-mechanical nose wheel steering system", Project stage presentation, Paris-Velizy, France, 2006.

[8] S. Enache, "Researches and contributions regarding improvement of dynamic performances of electrical machines of special uses", Habilitation thesis, Craiova, 2016.

[9] S. Ivanov, "Research from simulation and e-learning to industrial applications", Habilitation thesis, University of Craiova, 2014.

[10] A. K. Tyagi, "Matlab and Simulink", Oxford University Press 2012.

DOI: 10.52846/AUCEE.2022.02

Harmonic Analysis of Electromagnetic Torque in Brushless Direct Current Motors

Monica Adela Enache, Ion Vlad and Sorin Enache
Faculty of Electrical Engineering, Univesity of Craiova, Romania
senache@em.ucv.ro, menache@em.ucv.ro

***Abstract* – This study has aimed at establishing and analyzing the causes that produce oscillations of electromagnetic torque developed by brushless direct current motor. The study opportunity is given by the progresses obtained in command and power electronics, which made this motor performant from technical and economic viewpoint. The specialty literature reveals that important torque oscillations occur in this motor in a complete rotation. That is why, this study and the simulations presented here emphasize that there are five classes of slots relatively to the torque magnitude developed and the fact that all the slots are active, that meaning that the average torque developed occurs in the rotation direction. The harmonic analysis reveals that the torque distortion, within the five classes of slots, is variable between 51.03% and 97.63%. The torques computed for the slots classes are between the minimum limit of 0.029 Nm and the maximum one of 0.077 Nm. The low speed torque oscillations can be reduced with a high inertia moment, a speed reaction loop and a performant control system. The importance of the research theme is justified by what we have presented before and is a subject of major interest for engineering.**

Cuvinte cheie: *motor de curent continuu fara perii, design, cuplu electromagnetic, oscilatii de cuplu.*

Keywords: *brushless direct current motor, design, electromagnetic torque, torque oscillations.*

I. Importance of Driving Light Vehicles with Brushless Direct Current Motors

Electrical devices and installation supplied by local energy sources use permanent-magnet direct current motors, generally brushless motors. Such motors are also experienced in high-power drives: rolling mills, electrical cars and trucks [1-4].

These motors performances have increased by research, which has found new electro-technical materials and by developing the command and power electronics, which increased the conversion of the battery energy.

Brushless direct current motors are generally used for driving light vehicles: electrical bicycle, Fig. 1.a, [5], electrical motor scooter, Fig. 1.b, [6], electrical tricycle, Fig. 1.c, [7], trolleys for disabled, Fig. 1.d, [8].

In case of these vehicles (bicycle/motor scooter/tricycle/electrical trolley), the constructive solution adopted is closed, IP 44, and the motor is placed even in the wheel hub.

The constructive solution is with inner stator, made of steel sheets, with slots, where the winding is placed. The rotor is an outer one, made of steel, shaped as a cylinder, and there are inner permanent magnets, stuck, shaped as a parallelepiped.

a) b) c) d)

Fig. 1. Electrically driven light vehicles for people transport: a) bicycle; b) motor scooter c) tricycle d) trolley for disabled people.

In order to have high operation performances, rare-earth based permanent magnets are used, [9-13]. Load operation means motor heating, because of the losses occurring inside the machine.

High currents and temperatures contribute to demagnetization. That is why, the drives that use brushless direct current motors and must be correctly designed.

The problem of the demagnetization caused by the load current is not considered because the current is permanently controlled and it is limited by the controller and the heating is verified by measuring the temperature.

This paper aims at identifying the causes which produce electromagnetic torque oscillations and at limiting these oscillations [14-18].

II. Modelling Air-gap Magnetic Fields

The study is made with a brushless direct current motor having 2p=30 –number of poles, N_{cr}=27 –number of slots, Fig.2. The notations are as follows: β - command angle of the current in the phase *a*, α - geometrical angle of rotor displacement, γ -delay angle for the control of the current

I_a. Case α =0, when the axis of the slot "1" passes through O. Thus, the following relations results:

$$\beta = p \cdot \alpha + \gamma \quad (1)$$

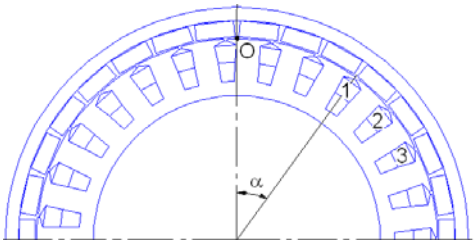

Fig.2. Cross section through the motor.

If the slot opening is neglected, the armature can be considered as being smooth and, in these circumstances, the inductor magnetic field is modelled as a curvilinear trapeze on the entire magnet width. The field is zero on the distance between two successive magnets.

Based on these considerations, the air-gap magnitude has been modelled, Fig. 3, relatively to x [mm] coordinate or to α [°]. Thus, the air-gap magnetic induction curve has resulted relatively to the rotor position, Fig. 4:

$$B = f(\alpha) \quad (2)$$

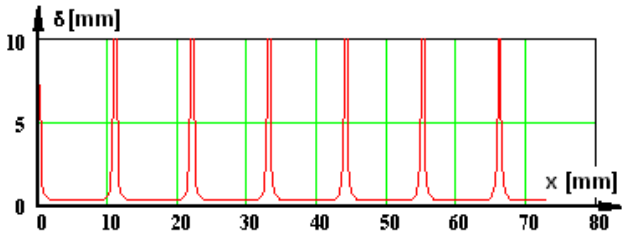

Fig.3. Curve modelling the air-gap magnitude.

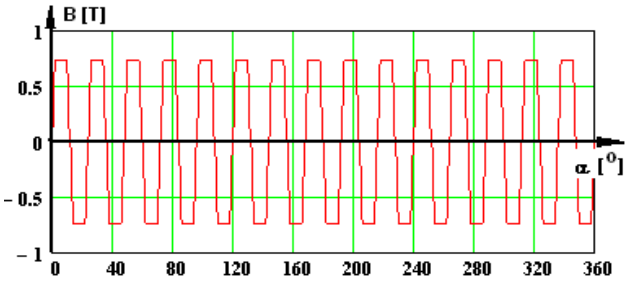

Fig.4. Distribution curve of the air-gap magnetic induction on the entire machine.

On the stator there is a star-connection three-phase winding, no null wire and two series connected phases during the operation. The winding is made in double layer, with coils concentrated on teeth, being a basic constructive component, which condition machine energetic parameters and cost.

The alternating stator currents are trapezoidal shaped, the duration of one pulse being of 120 electrical degrees. For α= 0 the armature ampere-turn curve has been computed and plotted, Fig. 5.a, considering the ampere-turn concentrated in the slot axis.

Because it is a much distorted quantity, the harmonic analysis of the curve has been made, Fig. 5.b, the distortion factor has been computed, k_{dis}=98.6%, and a big number of important harmonics has been emphasized.

It is noticed that the 15-th order harmonic (which is not the most important one in terms of magnitude, Fig.5.a), accomplishes the condition of equality of the poles number on the two armatures (2p=30).

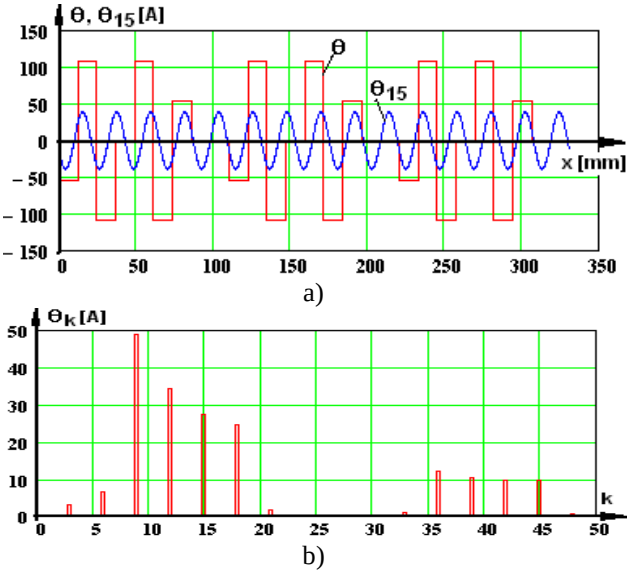

Fig.5. Armature reaction ampere-turn: a) curve and the 15-th order harmonic b) harmonic spectrum.

The air-gap dimension was numerically modelled at establishing the inductor magnetic field, so the curve of the reaction filed and the curve of the resultant field can be plotted, Fig.6.

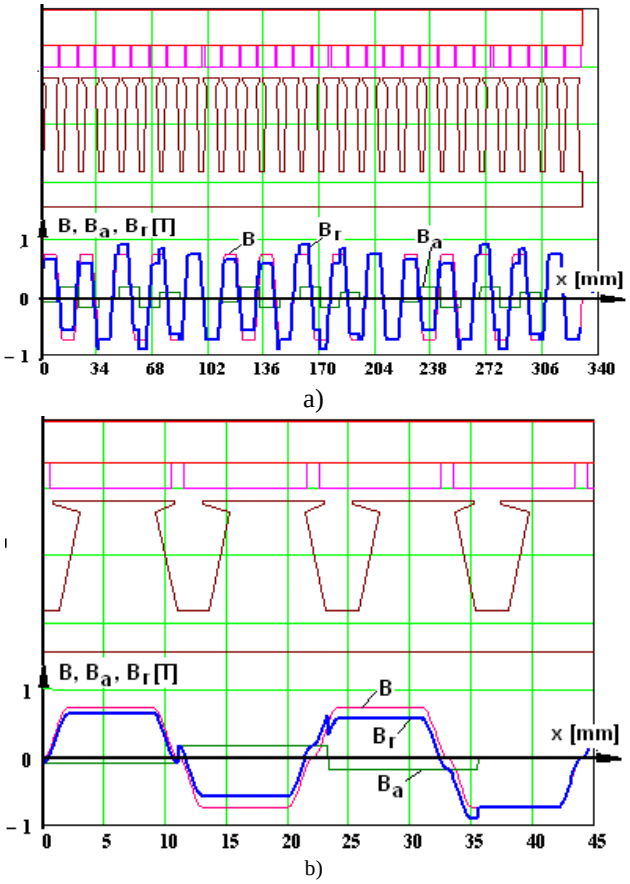

Fig.6. Plan section through the analyzed motor and the curves of the magnetic fields, B –inductor , B_a –reaction, B_r –resultant for: a) entire machine; b) on two pole pairs.

If the time origin t=0 is considered when α= 0, the numerical modelling of currents results relatively to the rotor position and the currents control:

$$I_a, I_b, I_c = f(\alpha, \gamma) \tag{3}$$

The control device models, on a pole pair, the currents of the three phases of the winding relatively to β - electrical angle, dependent on the rotor position. For the slot N_{cx}, the geometrical angle is:

$$\zeta_{Ncx} = \alpha + \frac{360}{N_c} N_{cx} \tag{4}$$

The ampere-turn provided by a slot is:

$$\theta_{Ncx} = 0.5 \cdot n_c (I_x + I_y) \tag{5}$$

where, n_c –number of conductors/slot, I_x, I_y are the currents I_a, I_b or I_c, relatively to the slot distribution on zones and phases, made according to literature.

In most cases, it is considered that the ampere-turn of a slot is concentrated in its axis and at the air-gap level.

This way, a numerical modelling of the slots electromagnetic torques has been established, as follows:

$$M_{Ncx} = B(\alpha) \cdot \theta_{Ncx}(\alpha, \gamma, N_{cx}) \cdot l_{Fe} \tag{6}$$

The instantaneous value of the electromagnetic torque results by summing the elementary torques of the slots.

The research can be carried on by using a program which is based on the presented mathematical model. There will be noted $N_{p\alpha}$ –number of points for a complete rotation and $N_{p\gamma}$ –number of points in which the control is delayed, for a pole pair. Thus, the following angles result:

$$\alpha_e = k_{p\alpha} \frac{360}{N_{p\alpha}} \qquad k_{p\alpha} = 1,2,3...,N_{p\alpha} \tag{7}$$

$$\gamma_e = k_{p\gamma} \frac{360}{N_{p\gamma}} \qquad k_{p\gamma} = 1,2,3...,N_{p\gamma} \tag{8}$$

For all combinations of values α_e, γ_e which result, there are computed and memorized the instantaneous values and the average value of the torque provided by a slot, respectively the total average torque, for a complete rotation.

III. Simulations and Results Obtained

The mathematical model presented was the basis of a numerical computation program and the simulations carried out and their results obtained enable identifying the causes and establishing important conclusions regarding the electromagnetic torque pulsations in brushless direct current motor.

From economic and technical considerations, there have been identified the following four possibilities for the motor supply:

Six-pulse supply for a pole pair

- -normal sequence of phases
- -inverse sequence of phases

Three-pulse supply for a pole pair

- - normal sequence of phases
- - inverse sequence of phases

In case of six-pulse supply and normal sequence of phases, the electromagnetic torque average value, for a complete rotation and different control angles, is presented in Fig. 7.

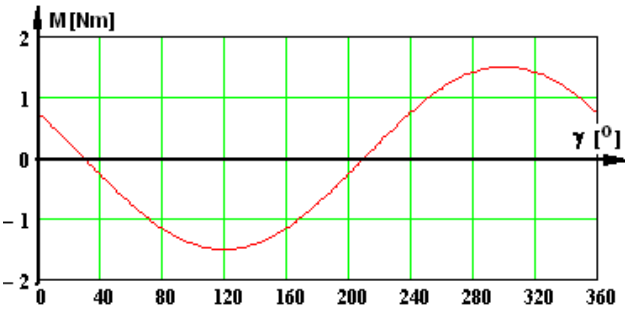

Fig.7. Electromagnetic torque average value in a complete rotation for different control angles of currents.

A. Control for the maximum total torque

From the analysis of this figure, it is noticeable that for γ=294° electrical angle, we have a positive maximum torque (for rotation sense to right) and for γ=114° electrical angle, we have negative maximum value (for rotation sense to left).

The maximum torques have equal absolute values, M_{max}=1.52 Nm. For the electrical angle γ=294°, the geometrical angle results ξ=294/15=19.6°, which shows where the first position transducer must be placed, relatively to the origin – point O, on the stationary armature. The other two position transducers are placed at each 120° electrical angle, in the rotation direction.

The average values, for a complete rotation, of the torques provided by each slot, are presented in Fig. 8 and Fig. 9.a shows the total torque curve, for a complete rotation of the motor. This curve is analyzed from harmonic viewpoint and a harmonic spectrum results in Fig. 9.c, where the important harmonics can be identified, which affect the torque curve, Fig. 9.b.

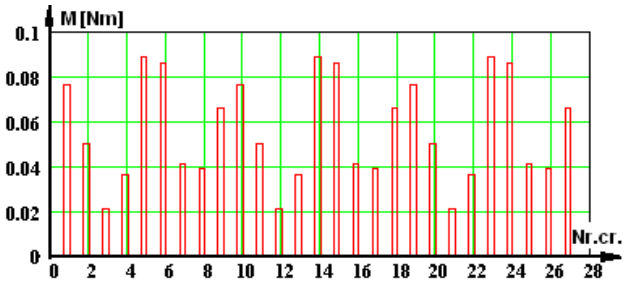

Fig.8. Average values of torques provided by the machine slots for control angle γ=294° M_{Nmed}=1.52 Nm.

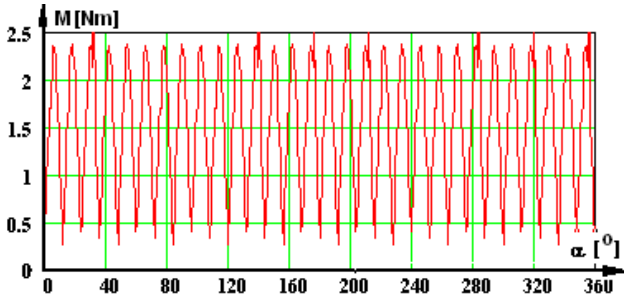

a)

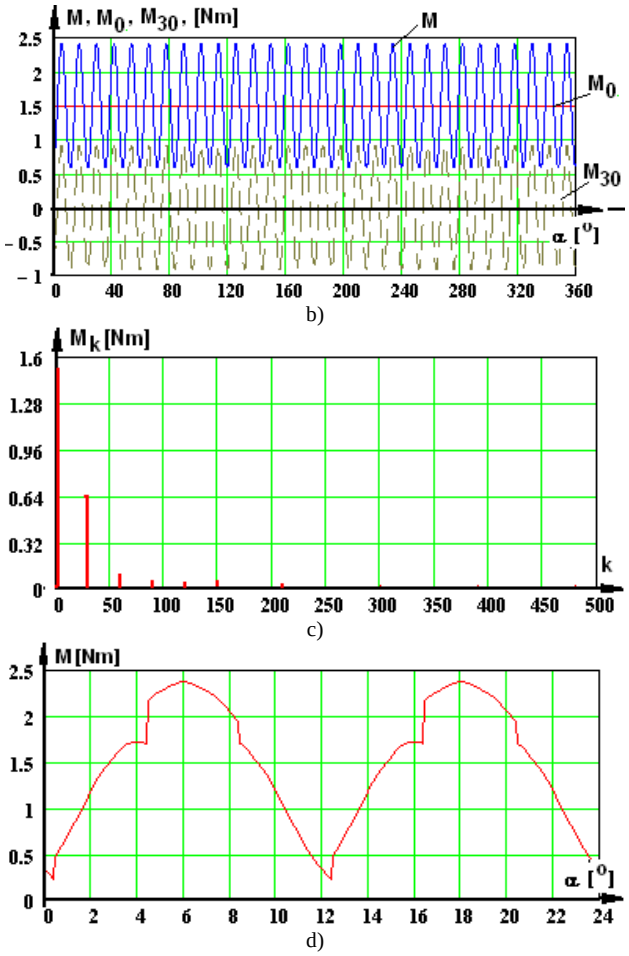

Fig.9. Variation curve of the motor torque: a) for a complete rotation; b) the continuous component and the main harmonic; c) harmonic spectrum; d) torque curve for a pole pair.

The total torque curve for a pole pair is depicted in Fig. 9.d and the harmonic analysis results are filled in the Table I, where there is comparison with the previous results.

B. Analysis of electromagnetic field in each slot

Further on in this paper, a detailed analysis of Fig. 8 is made, in order to divide up in classes the 27 slots of the motor, relatively to the produced average torque. The results of this classification are filled in the Table II.

TABLE I. Analysis of the total torque

	Total torque			Distortion factor
	Average value M_{med} [Nm]	Important harmonics M_k [Nm]		K_{dis} [%]
Analysis for a complete rotation	1.497	M_{30}=0.646	M_{60}=0.069	40.21
Analysis for a pole pair	1.487	M_2=0.655	M_4=0.081	41.06

TABLE II. Slots divided up into classes

Class	Afferent slots	Torque average value
I	5, 6, 14, 15, 23, 24	M_{cr}=0.084 Nm
II	1, 10, 14	M_{cr}=0.077 Nm
III	2, 11, 19	M_{cr}=0.051 Nm
IV	4, 8, 13, 22	M_{cr}=0.038 Nm
V	3, 12, 21	M_{cr}=0.021 Nm

A slot is chosen for each class, the torque curves for a pole pair are presented, Fig. 10, and an analysis is made, from harmonic point of view, Fig. 11.

Any problems occur in the slots 3, 12, 21, where we see large positive and negative torque oscillations (Fig.10.c); in the slots 2, 11, 19 the oscillations are lower (Fig.10.b).

These oscillations cause superior torque harmonics which may exceed even the continuous component, Fig. 11.b and Fig. 11.c, an undesirable effect.

For the analyzed slots, in Fig. 12 there are depicted torque curves, where we have the continuous component, the important harmonic and the resultant torque. The final results of this analysis are detailed in table no. 3, where the distortion factor is also presented.

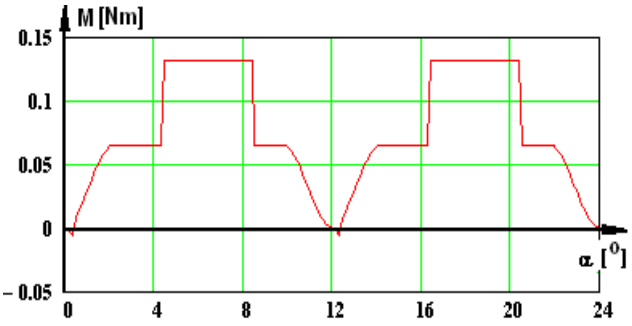

a) torque provided by the slot no.1

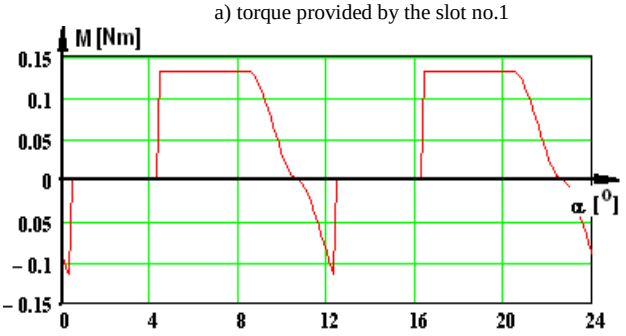

b) torque for the slot no. 2

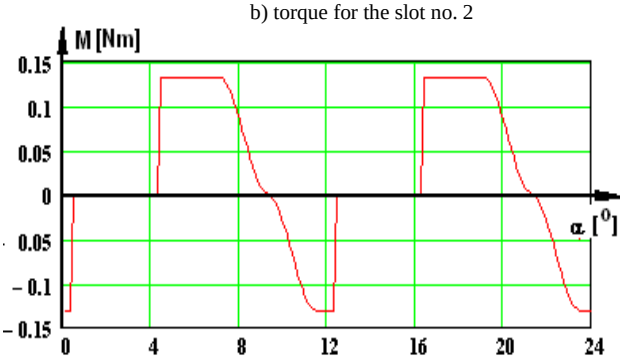

c) torque for the slot no. 3

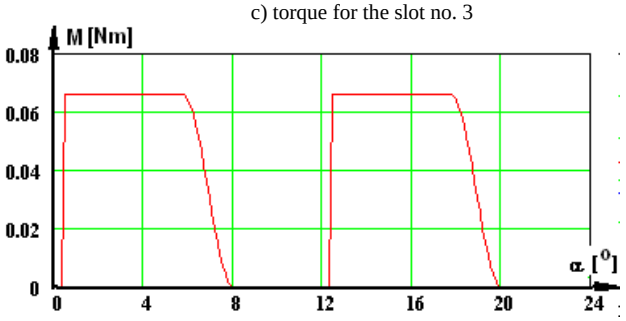

d) torque for the slot no. 4

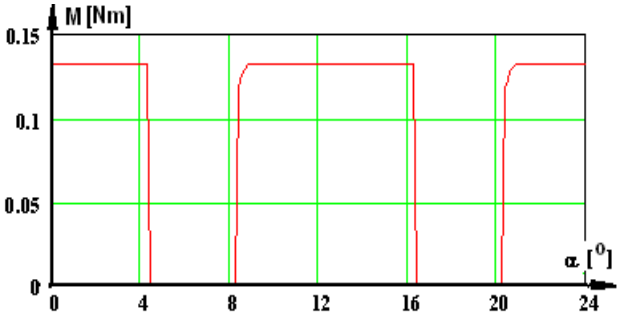

e) torque provided by thr slot no.5

Fig.10. Variation curves for a pole pair for the torque provided by the currents passing the conductors of a slot.

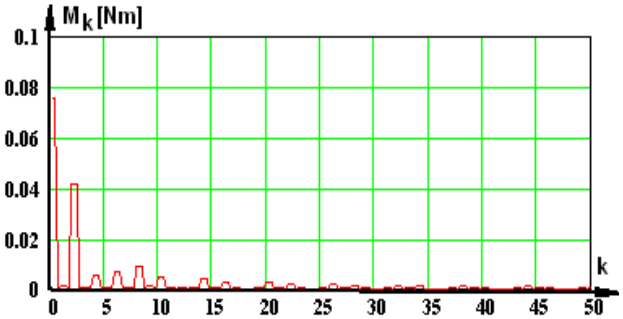

a) torque harmonics in the slot no. 1

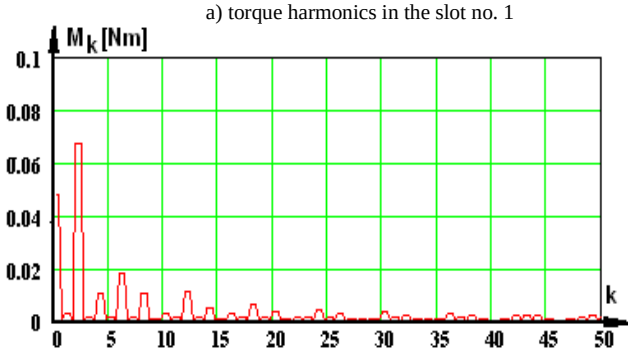

b) torque harmonics for the slot no. 2

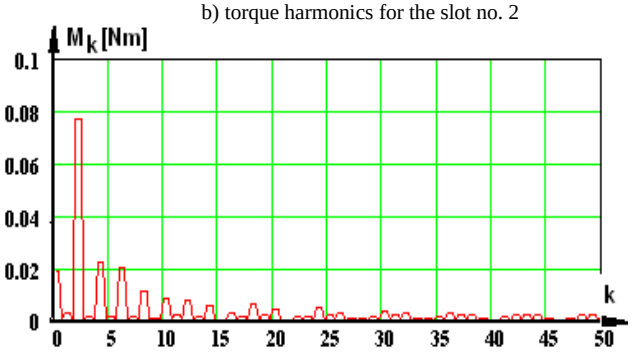

c) torque harmonic in the slot no.3

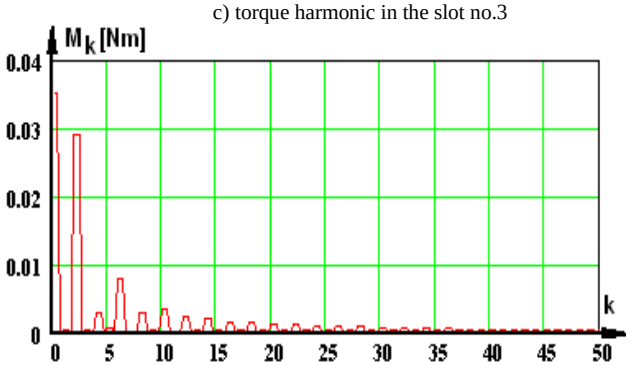

d) torque harmonics for the slot no. 4

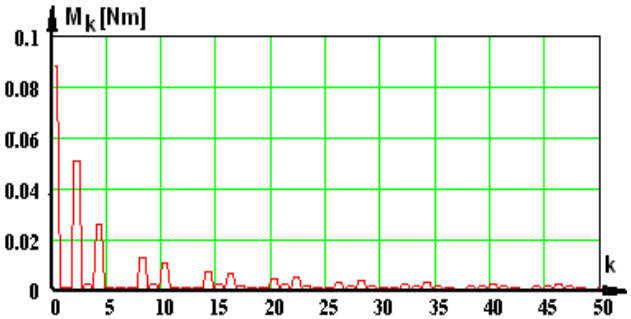

e) torque harmonics for the slot no.5

Fig.11. Harmonic spectrum for the torque curves presented in fig.5.

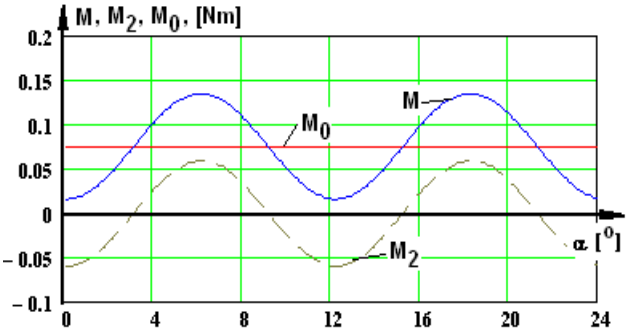

a) slot no. 1

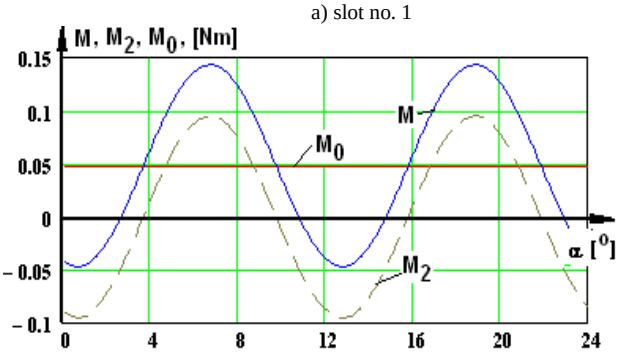

b) slot no. 2

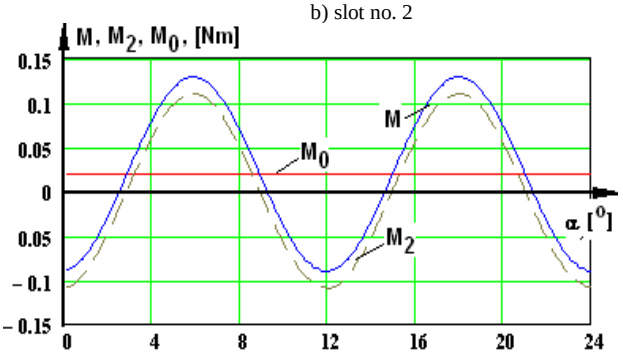

c) slot no. 3

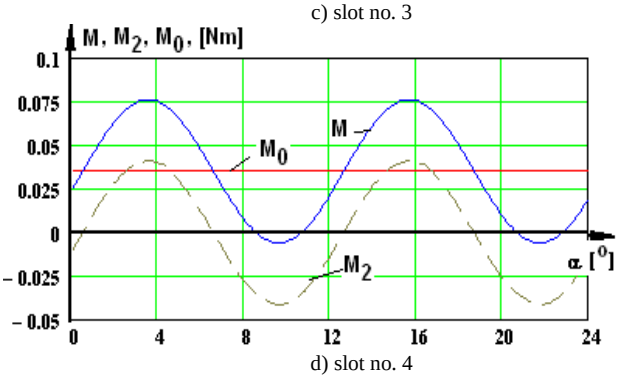

d) slot no. 4

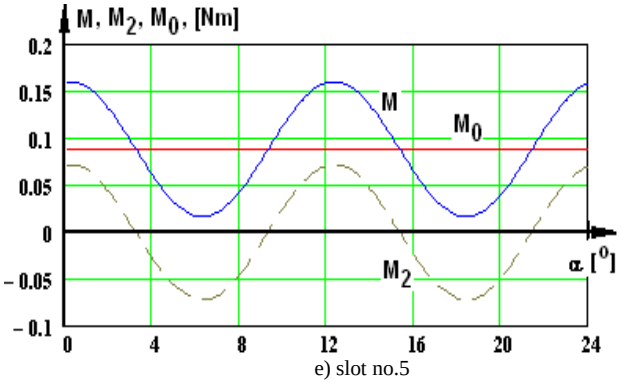

e) slot no.5

Fig.12. Variation curves for a pole pair, for the continuous component, the second order harmonic and their sum.

TABLE III. Analysis of slot torque for a period

	Torques			Distortion factor
Slot no.	Average value M_{med} [Nm]	Important harmonics M_k [Nm]		K_{dis} [%]
1	0.075	M_2=0.042	M_8=0.009	51.03
2	0.048	M_2=0.067	M_6=0.018	83.59
3	0.019	M_2=0.077	M_4=0.022	97.63
4	0.035	M_2=0.029	M_6=0.008	66.32
5	0.088	M_2=0.051	M_4=0.026	56.92

CONCLUSIONS

The research carried out has aimed at analyzing the causes which produce total torque oscillations, in the most favourable case, meaning six-pulse supply, direct sequence of phases and $\gamma = 294^o$ – control angle of the *a* - phase current.

The simulations presented before and the results filled in the Table III show that we have five classes of slots relatively to the magnitude of the torque provided and the fact that all slots are active, meaning the average torque developed is in the rotation sense. The torques computed for slots classes are within the minimum limit, M_{min}= 0.029 Nm, and the maximum one, M_{max}= 0.077 Nm.

The slots belonging to the classes I (six) and V (three) have an accepted value of the average torque and a small distortion factor, $k_{disMcr.I}$ =51.03% and $k_{disMcr.V}$=56,92%.

The slots belonging to the classes II (three) and III (three) have high average torques, but they also have a high distortion factor, $k_{disMcr.II}$ =83.59% and $k_{disMcr.V}$=97.63%.

The slots belonging to the class IV (four) produce the smallest torque, with a distortion factor $k_{disMcr.IV}$=66.32%.

This is the explanation for high torque oscillations which occur in brushless direct current motors. An almost constant torque cannot be obtained with this motor, but it is possible to be close to fulfilling this requirement.

The torque variation for a pole pair is a major drawback and it is explained by an imperfect commutation of the phase currents and by the position occupied by slots in the inductor magnetic field.

The high inertia moment of the rotor and the high speed decrease the speed oscillations caused by the torque variations. A speed reaction loop and a performant control system can reduce substantially the torque oscillations at low speed.

ACKNOWLEDGMENT

Source of research funding in this article: Research program of the Electrical Engineering Department financed by the University of Craiova.

Contribution of authors:
First author – 40%
First co-author – 30%
Second co-author – 30%

Received on July 17, 2022
Editorial Approval on November 15, 2022

REFERENCES

[1] C. Bianchini, F. Immovilli, E. Lorenzani, A. Bellini, M. Davoli, "Review of Design Solutions for Internal Permanent Magnet Machines Cogging Torque Reduction", *IEEE Transactions on Magnetics*, Vol. 48, No.10, 2012, pp 2685-2693.

[2] J. Cros, P. Viarouge, R. Carlson, L.V. Dokonal, "Comparison of brushless DC motors with concentrated windings and segmented stator", *ICEM 2004*, Krakow, Poland, 2004

[3] L. Dosiek, P. Pillay, "Cogging Torque Reduction in Permanent Magnet Machines", *IEEE Trans. On Industry Applications*, Vol. 43, No. 6, 2007, pp 1565-1571.

[4] W. Fei, P.C.K. Luk, "A New Technique of cogging Torque Suppression in Direct-Drive Permanent-Magnet Brushless Machines", *IEEE Trans. on Industry Applications*, Vol 46, No. 4, 2010, pp. 1332-1340.

[5] http://www.bicicleteelectrice.com/2015/06/bicicleta-electrica-zt-08.html

[6] [3] http://www.keewayromania.ro/ro/

[7] [4] http://www.bizoo.ro/firma/nogal/vanzare/6890815/tricicleta-adulti-electrica-zt02

[8] https://sistemeortopedice.ro/scuter-electric/136-scuter-electric-vantage-x.html

[9] M.S. Islam, S. Mir, T. Sebastian, "Issues in reducing the cogging torque of mass-produced permanent magnet brushless DC motor", *IEEE Trans. on Industry Applications*, Vol. 40, No. 3, 2004, pp.813 – 820.

[10] J. Kaňuch, Z. Ferková, "Design and simulation of disk stepper motor with permanent magnets", *Archives of Electrical Engineering*, Vol. 62, No. 2, 2013, pp. 281-288.

[11] T. Koch, A. Binder, "Permanent magnet machines with fractional slot winding for electric traction", ICEM 2002, Brugge, 2002.

[12] *** Catalog ICPE Bucharest, Al-Ni-Co and Nd-Fe-B sintherised magnets–magnetic features.

[13] http://www.magneticsmagazine.com/main/ channels/ magnetic assemblies/ passive-magnetic-bearing-prototype-testing-results/.

[14] W.C. Chi, M.Y. Cheng, C.H. Chen, "Position-sensorless method for electric braking commutation of brushless DC machines", *IET Electric Power Applications*, Vol.7, Issue 9, 2013, pp.701-713.

[15] M. Miyamasu, K. Akatsu, "Efficiency Comparison between Brushless DC Motor and Brushless AC Motor Considering Driving Method and Machine Design", *37th Annual Conference of the IEEE Industrial-Electronics-Society IECON 2011*, pp.1830-1835.

[16] M. Ancău, L. Nistor, "Optimization Numerical Techniques in Computer-aided Design", *Bucharest, Technical Publishing House*, 1996.

[17] T. Tudorache, L. Melcescu, M. Popescu, "Methods for Cogging Torque Reduction of Directly Driven PM Wind Generators", *12th International Conference on Optimization of Electrical and Electronic Equipment*, OPTIM, 2010.

Y.L. Zhang, W. Hua, M. Cheng, G. Zhang, X.F. Fu, "Static Characteristic of a Novel Stator Surface-Mounted Permanent Magnet Machine for Brushless DC Drives", *38th Annual Conference on IEEE-Industrial-Electronics-Society (IECON 2012)*, 2012, pp.4139-4144.

DOI: 10.52846/AUCEE.2022.03

Fuzzy Model for Estimating the Power Consumed in a Transformer Station

Cristian Bratu*, Daniela Popescu* and Cătalin-Constantin Luţu†

* University of Craiova/IEEA, Craiova, Romania, cbratu@elth.ucv.ro

* University of Craiova/IEEA, Craiova, Romania, dpopescu@elth.ucv.ro

† Oltenia Energy Distribution, Craiova, Romania, catalin.lutu@gmail.com

***Abstract* – The paper studies the implementation of a new transformer station in a network designed to take over some of the existing consumers, to provide the necessary energy for a number of new consumers and a reserve for future new connections to the electricity grid. By creating a fuzzy model, a number of rules have been created to highlight the power consumtion regimes, manifested at the level of the transformer station. Also, the possibility of optimizing and taking over from existing clients was created so that a balance and an optimization can be created regarding the disposition of the consumers on each station.**

Cuvinte cheie: *bare încapsulate, curenţi mari, model magnetic, model termic în regim staţionar,probleme cuplate.*

Keywords: *encapsulated busbars, high currents, AC magnetics model, steady-state heat transfer model, coupled problems.*

I. INTRODUCTION

The major changes in the structure of electricity networks illustrate the decentralization of these systems and generate a huge amount of data, which must be processed efficiently. The management of these networks begins by processing-more and more in real time the information provided from the field. [2].

The use of artificial intelligence in the energy field can be found in studies on the integration of production from renewable sources, forecasting of electricity conversion and their price, power quality control, improving the stability of electricity systems.

The paper is intended to be a way to present the advantages of using computer algorithms or even artificial intelligence in the process of managing electrical networks.

The analysis in this paper is based on a hypothetical study, for an electrical network that supplies both household and non household consumers, single-phase and three-phase, as well as prosumers with photovoltaic panels, which will generate only during the day and for which the weather conditions were neglected. Thus, a generalized, optimal regime was analyzed, which theoretically applies in ideal conditions manifested daily.

The main objectives pursued were:

- defining the area of interest;

- creation of rules for highlighting the power consumption regimes manifested at the level of the transformer stations;

- establishing the time intervals in which the analysis was carried out;

- graphic highlighting by variation of the input data, of the different operating regimes for the electrical network.

II. TRANSFORMER STATION

Among critical electrical assets, the power transformer is probably the most representative [2]

A substation is a downstream transformer substation with a power of up to 2500 kVA, designed to supply low voltage (up to and including 1 kV) to consumers.

A substation consists of MV connection equipment (20 or 6 kV), one or more MV/LV transformers and LV switchboards, [7].

In relation to the grounding, the transformation stations can be divided into three categories, namely:

a. Overhead substations mounted on concrete (rarely wooden) poles, with relatively low power transformers, usually between 20 and 250 kVA and usually intended to supply low voltage consumers in rural areas.

b. Above ground transformation stations; this positions are performed in the following variants:

b.1. substations in metal cabins, prefabricated, usually used for temporary supply, site (rarely for normal urban supply), with powers between 100 and 1000 kVA;

b.2. transformation stations in above ground rooms, realised in specially built wall cabins or on the ground floor of apartment blocks in some rooms specially reserved and arranged for the transformation station or in specially reserved rooms in the technological premises of industrial enterprises.

c. Underground transformation stations, built in an underground construction, in places where for various reasons (such as urban systematization), it is not allowed to build an underground construction.

III. FUZZY LOGIC

Fuzzy logic is a fascinating field of research because it makes a very good connection between meaning and accuracy.

The advantages of using fuzzy logic over other methods are:

a. is easy to understand, because it uses simple mathematical concepts;

b. it is flexible because it starts from information with a greater or lesser degree of inaccuracy;

c. can model nonlinear functions with arbitrary complexity; a fuzzy system can be created, starting from any set of input-output data;

d. is based on natural language, ie the language of human communication;

e. can be combined with conventional control techniques.

Fuzzy sets start from the fundamental idea that if X is the "total" set, any subset A, in the classical sense, of X, can be identified with its characteristic function [4]:

$$f_A: X \rightarrow \{0,1\} \quad (1)$$

where $\begin{cases} f_A(x) = 0, \ x \neq A \\ f_A(x) = 1, \ x = A \end{cases}$

The fuzzy subset A of X is defined by a membership function:

$$f_A: X \rightarrow [0,1] \quad (2)$$

A membership function is a curve that defines how each point in the definition domain is assigned a membership value (degree) between 0 and 1.

The usual operations of classical set theory (reunion, intersection, complement, etc.) can be repeated in the case of fuzzy sets, in terms of the function of membership.

IV. PROPOSED MODEL

The analyzed MV/LV substation feeds both single-phase and three-phase household and non-household consumers.

Prosumers are also connected to the transformer station, ie consumers who can store and sell electricity produced from renewable sources [3, 5].

To determine the power consumed in a transformer station, we will use the graphical user interface (GUI) in the Fuzzy Logic Toolbox module of the Matlab application.

In the Fuzzy Logic Toolbox module there are 5 graphical interfaces to use for building, editing and observing a problem: Fuzzy Interface System, Fuzzy Editor (FIS Editor), Membership Function Editor, Rule Editor and Rule Viewer.

The proposed fuzzy system has four inputs (period, type of source, consumer category and installed power) and one output (power consumed).

In the first stage, the functions of the membership are established for the inputs and outputs of the fuzzy system.

The membership functions will be trapezoidal functions, with 4 value ranges each, covering the entire range of installed power values.

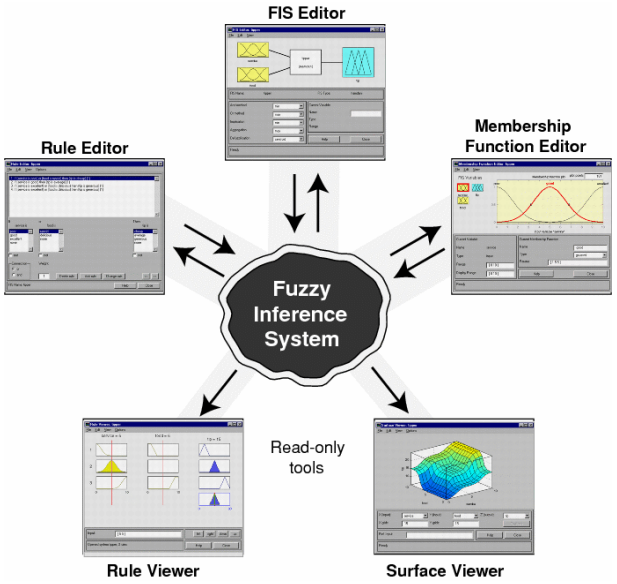

Fig. 1. Fuzzy simulator interfaces.

The membership functions for the system inputs and outputs are shown in Figures 2÷6.

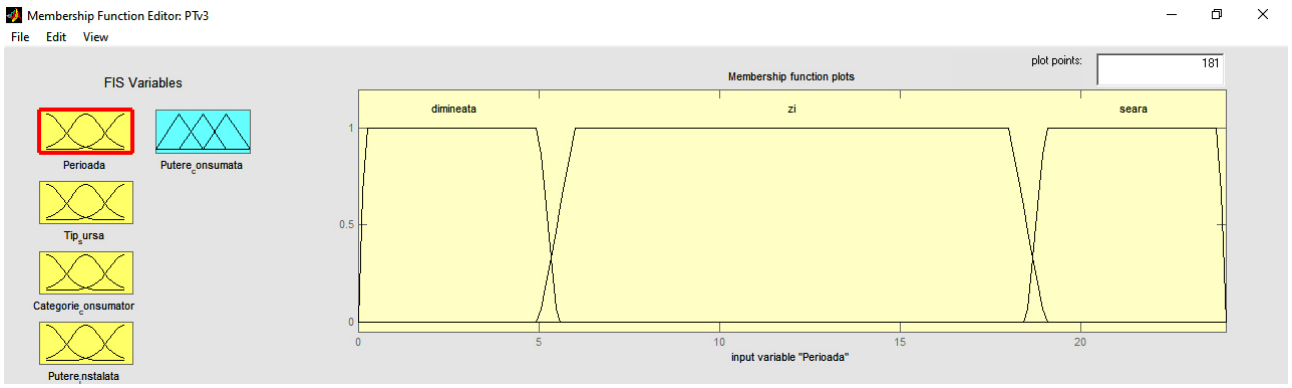

Fig. 2. Membership functions for the the time period: morning (0 0,2 5 5,5), day (5 6 18 19), evening (18.5 19 23.8 24).

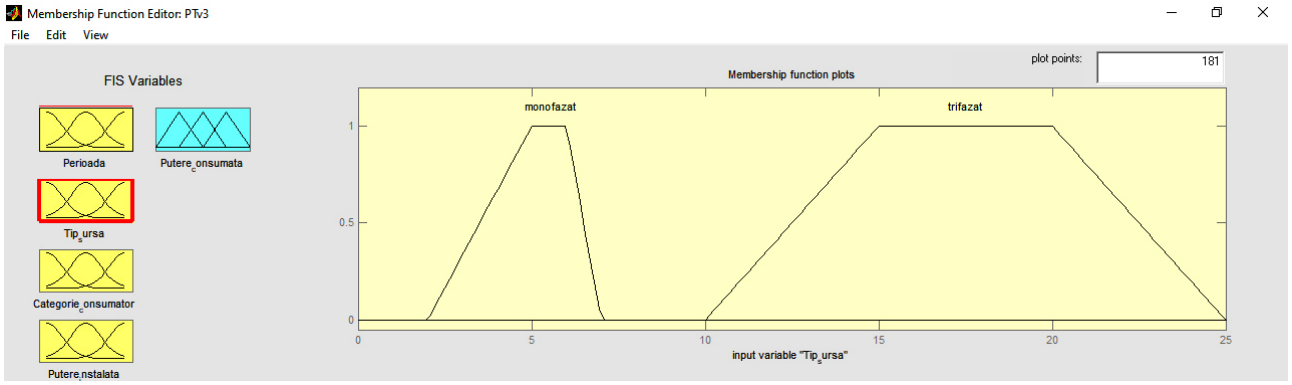

Fig. 3. Source type membership functions: single phase (2 5 6 7) and three-phase (10 15 20 25).

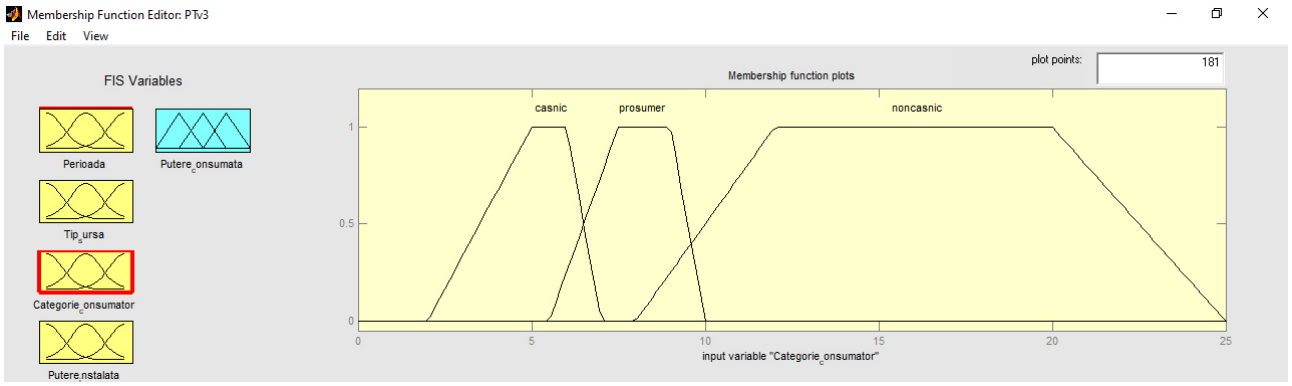

Fig. 4. Consumer functions: household (2 5 6 7), prosumer (5.5 7.5 9 10) – only applicable for day time and non-household (8 12 20 25).

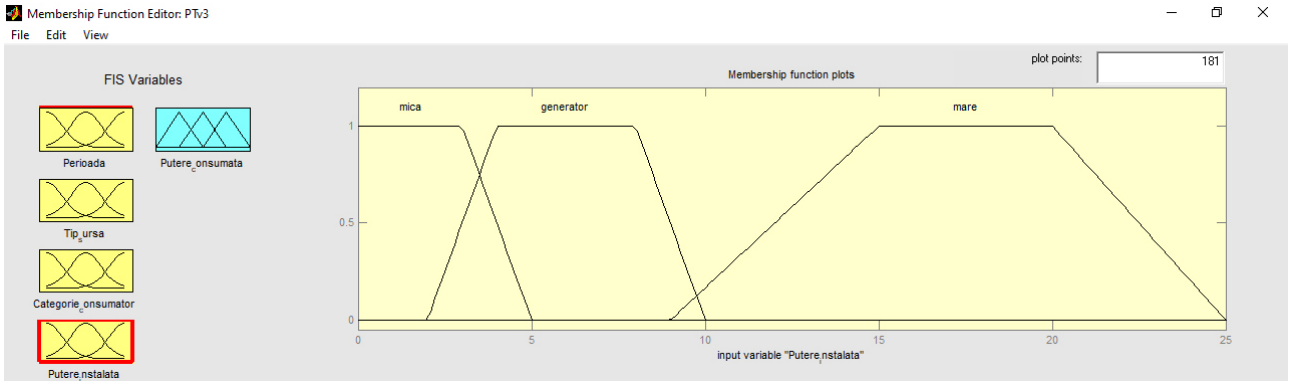

Fig. 5. Belonging functions for installed power: small (0 0 3 5), large (9 15 20 25), generator (2 4 8 10) – was considered for consumers who only generate in the network, without having individual consumption.

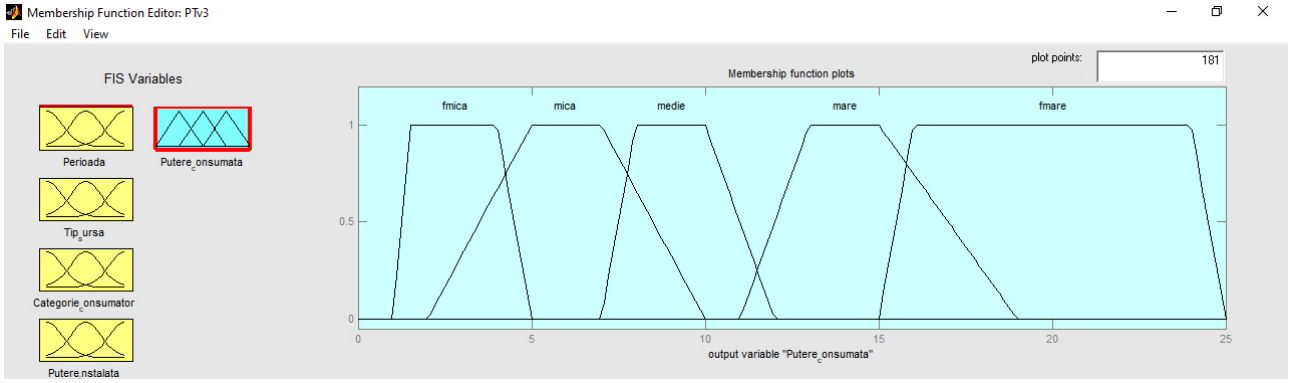

Fig. 6. Membership functions for power consumption: very low (1 1.5 4 5), low (2 5 7 10), medium (7 8 10 12), high (11 13 15 19) very high (15 16 24 25).

In the second stage, the rules used to create the fuzzy diagram will be established and implemented, depending on the time period:

a. night:

* three-phase consumer – household – low installed power =>low consumption

* three-phase consumer – household – high installed power =>medium consumption

*single phase consumer – household – low installed power => very low consumption

* single phase consumer – household – high installed power => low consumption

* three-phase consumer – non-household – low installed power => medium consumption

* three-phase consumer – non-household – high installed power =>very high consumption

* single phase consumer – non-household – low installed power => low consumption

* single phase consumer – non-household – high installed power =>high consumption

b. day:

* three-phase consumer – household – low installed power => low consumption

* three-phase consumer – household – high installed power => medium consumption

* single phase consumer – household – low installed power => very low consumption

* single phase consumer – household – high installed power => low consumption

* three-phase consumer – non-household – low installed power => medium consumption

* three-phase consumer – non-household – high installed power =>very high consumption

* single phase consumer – non-household – low installed power => low consumption

* single phase consumer – non-household – high installed power =>high consumption

*prosumers – three-phase – low installed power => low consumption

* prosumers – three-phase – high installed power =>medium consumption

* prosumers – single phase – low installed power => very low consumption

* prosumers –single phase – high installed power => low consumption

* prosumers – three-phase – generator => low consumption

* prosumers – single phase – generator => very low consumption

c. evening:

* three-phase consumer – household – low installed power => low consumption

* three-phase consumer – household – high installed power => medium consumption

* single phase consumer – household – low installed power => low consumption

* single phase consumer – household – high installed power => medium consumption

* three-phase consumer – non-household – low installed power => medium consumption

* three-phase consumer – non-household – high installed power => very high consumption

* single phase consumer – non-household – low installed power => low consumption

* single phase consumer – non-household – high installed power => high consumption

In the third stage, the output values are obtained, the inputs in the fuzzy system and the activated rules are shown in Figure 7 and 8. Depending on the values set for the 4 inputs, an answer will be established which represents the power consumed.

The fuzzy simulator from the Matlab application also allows the generation of results in the form of three-dimensional surfaces (Figures 9÷11).

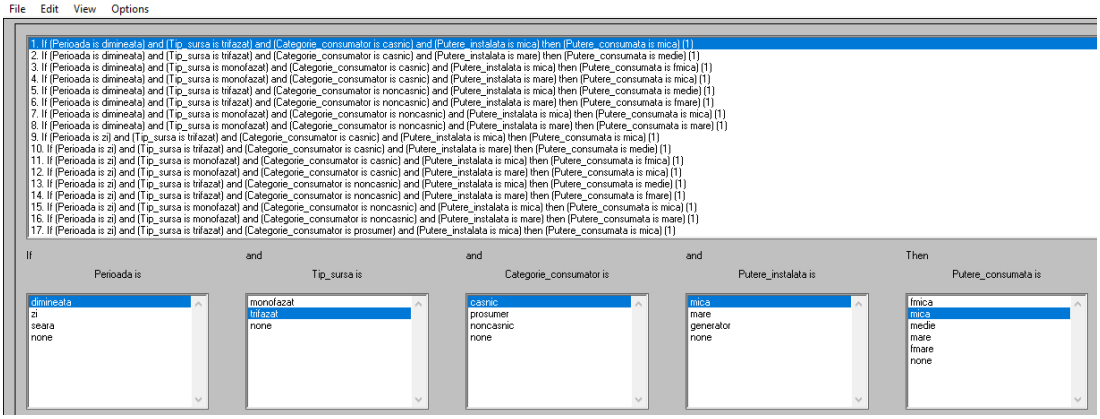

Fig. 7. The rules used to create the fuzzy diagram

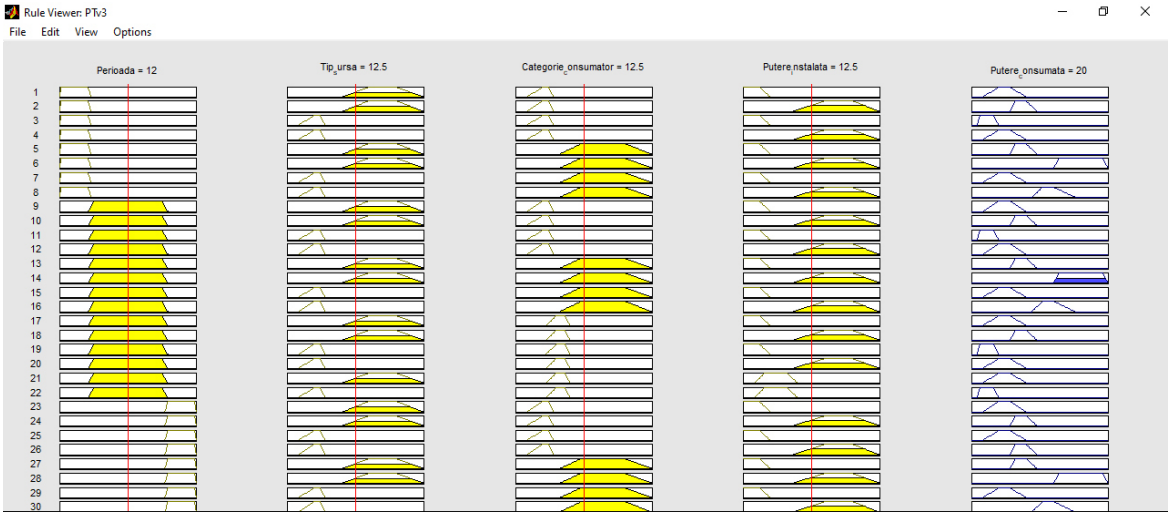

Fig. 8. For non-household, three-phase consumers who have a high installed power, variations are observed for three periods of time (morning, day, night) of the energy consumed due to the compensation of the prosumers during the day.

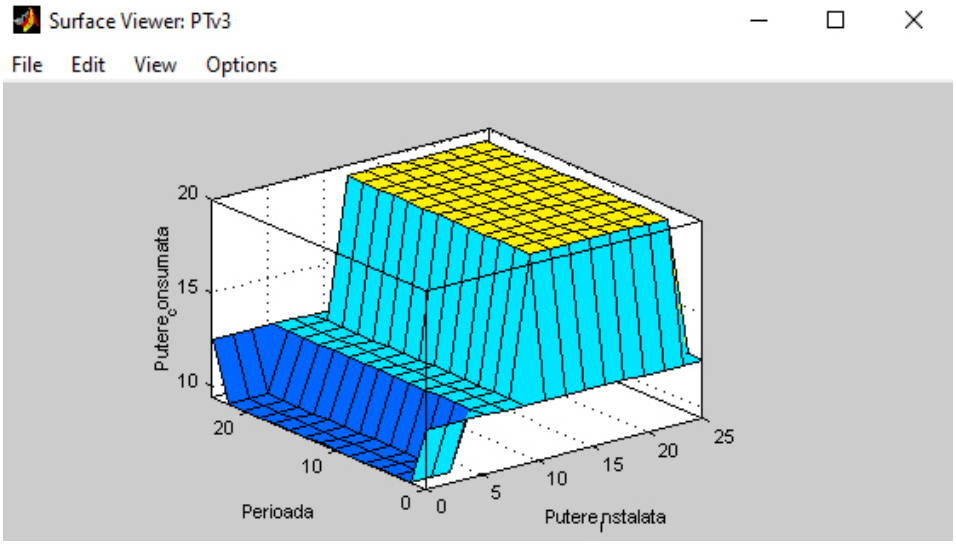

Fig. 9. View as “surface” for consumed power taking into account the time period and installed power.

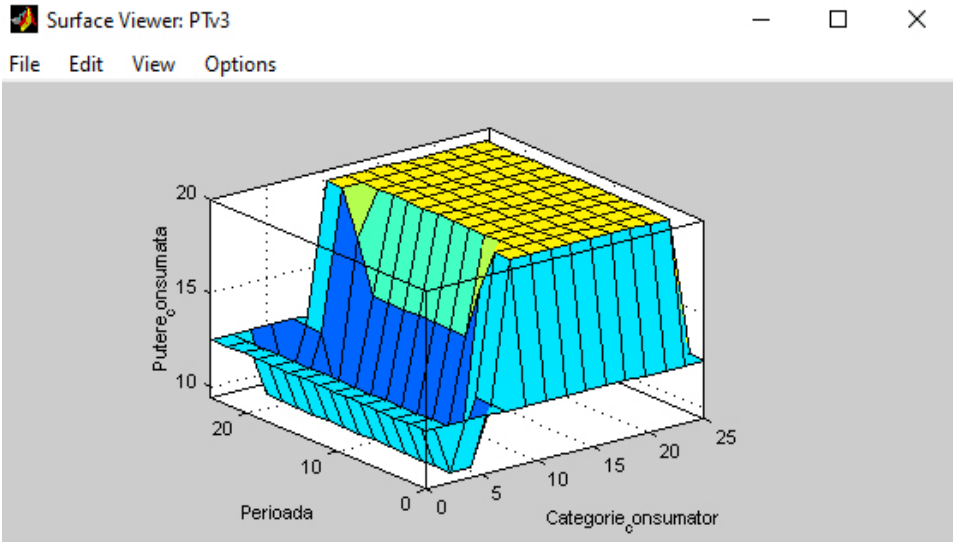

Fig. 10. View as “surface” for consumed power taking into account the time period and the category of consumers.

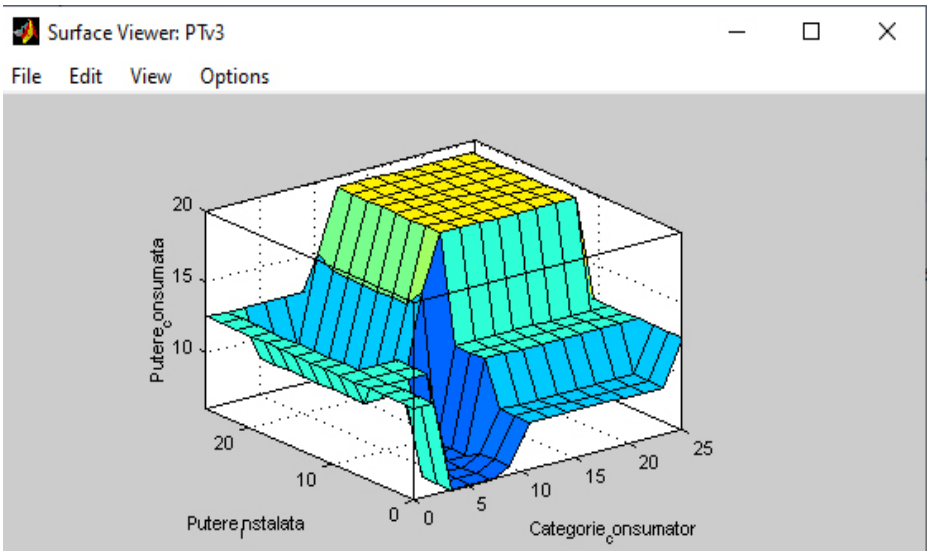

Fig. 11. View as "surface" for consumed power taking into account the installed power and the category of consumers.

Of course, variations in these indices can be greatly customized and the level of accuracy can increase with a more accurate approach to input data, Also, with the optimization for the area of interest of the operation regime of the prosumers, more realistic data can be obtained in accordance with the topographic, meteorological, atmospheric data etc.

V. Conclusions

Although it seems a difficult and complicated process to create correct diagrams, it must be borne in mind that the network administrator interacts only with the graphical interface, which is much easier to use and interpret.

The advantage of using artificial intelligence in electrical networks through the use of a graphical interface, has a clear advantage due to easy use but also the possibilities of network efficiency thus reducing losses and at the same time ensuring continuity in power supply to consumers.

As perspectives of the applications of computational intelligence in energy, a bridge is currently being created between the pool of producers and that of electricity consumers beyond the electricity transmission and distribution network: the electricity storage facilities.

Acknowledgment

Source of research funding in this article: Research program of the Electrical Engineering Faculty, financed by the University of Craiova.

Contribution of authors:

First author – 50%

First coauthor – 30%

Second coauthor – 20%.

Received on July 10, 2022

Editorial Approval on November 20, 2022

References

[1] A.P., Rahman, G., Harry, Suwarno, N.u, Maulidevi,A.S., Bambang, *A fuzzy model for power transformer faults' severity determination based on gas level, gas rate and dissolved gas analysis interpretation*, Enaegies 2020, 13(4) https://www.mdpi.com/1996-1073/13/4/1009/htm

[2] D.M., Ricardo, D.A., Zaldivar, A.R, Andres, Z., JAefferson, E.E., Monbello, *A fuzzy inference- based approach for estimating Power transformers risk index*, Electric Power Systems Research, vol 209, 2022 https://www.sciencedirect.com/science/article/abs/pii/S0378779622002309#!

[3] H.C., Yeong, C.C., Yi, L.L., Sau, .L., Chen, *Smart three-phase power transformer utilizing fuzzy logic approach*, Proceeding of 10th WSEAS International Conference on Electronics, https://www.researchgate.net/publication/262357630_Smart_three-phase_power_transformer_utilizing_fuzzy_logic_approach

[4] L.A., Zadeh, *Fuzzy sets; Information and Control*, Vol. 8, No. 3, 1965, pp.338-353.

[5] M., Gavrilaș M., O., Ivanov, G., Gavrilaș, *REI Equivalent Design for Electrical Power Systems with Genetic Algorithms*, WSEAS Transactions on Circuits and System,Vol. 7, nr. 10, pp. 911-921.

[6] S.M., Islam,. T., Wu, G., Ledwich, *A novel fuzzy logic approach to transformer fault diagnosis*. IEEE Trans. Dielectr. Electr. Insul. 2000, 7, 177–186.

[7] https://www.cez.ro/ckfinder/userfiles/files/cez/despre-noi/cezd/politici-tehnice/pt-pa-pc.pdf

DOI: 10.52846/AUCEE.2022.04

Current Issues Regarding the Analysis of the Physico-Chemical and Electrical Properties of Transformer Oil

Mircea Emilian Ardeleanu*, Aurelia Scornea†, Dan Gabriel Stănescu*,
Ionuţ Marius Burciu* and Ioana Gabriela Sîrbu*

* University of Craiova/Department of Electrical, Power and Aerospace Engineering, Craiova, Romania,
mardeleanu@elth.ucv.ro, dstanescu@elth.ucv.ro, burciuionut95@yahoo.com, osirbu@elth.ucv.ro

† National Institute for Research, Development and Testing in Electrical Engineering/ High Voltage Division,
Craiova, Romania, scornea@icmet.ro

Abstract – **Researchers and practitioners interested in the operation, monitoring and diagnosis of electrical equipment (such as: transformers, motors and generators, circuit breakers, etc.) know that in order to ensure a safe operation of such equipment it is necessary to know, among other things, the condition of the insulation system. This is one of the essential information to know because about 40% of failures which occur in the operation of the electrical equipment are due to insulation breakdown; in some cases they can reach even close to 100%. In this context this paper proposes the presentation of several modern methods and equipment for the study and analysis of physical and chemical properties (namely: analysis of water content, density and interfacial tension, dissolved gas analysis and furan components determination) and electrical parameters (namely: determination of loss factor and relative permittivity) of transformer oil. Samples of transformer oil type MOL TO 30.01 (uninhibited electrical insulator, non-additive), new StaSo Transformer Oil I (high quality inhibited insulating oil) and TR 30 oil were studied. Two samples were collected directly from the original barrel, two samples were collected from the transformer tank after dielectric tests at the transformer's manufacturer and also two samples of used TR 30 oil were collected from two transformers. The tests were carried out in an accredited laboratory with calibrated equipment. The results highlighted the properties of each analyzed sampled. The interpretation of the results emphasized the qualities and defects of each analyzed oil sample and whether or not they fit the standards in the field.**

Cuvinte cheie: *ulei de transformator, factor de pierdere, permitivitate relativă, tensiune interfacială, analiza gazelor dizolvate.*

Keywords: *transformer oil, loss factor, relative permittivity, interfacial tension, dissolved gas analysis.*

I. Introduction

From the practice of operation and maintenance of electrical equipment (transformers, motors and generators, etc.) it is known that, in order to ensure a safe operation and functionality, it is necessary to know, among other things, the condition of the insulation system, because about 40% of malfunctions which occur in operation are due to damaged insulation. In some cases, this percentage can even reach close to 100% [1-3].

Therefore, ensuring a safe and long-lasting operation of electric power transformers, an important and essential element in the electricity transmission and distribution system, is a permanent concern and a main objective for both manufacturing companies and users [3].

The insulation system of electrical equipment, in general, is subjected, during the entire operation, to a complex of stresses: electrical, mechanical, thermal etc. Thus, in the case of an electrical transformer, its insulation system must withstand and transmit at the same time to the coolant (transformer oil) the heat developed in the various construction elements (windings, magnetic circuit) [1, 4, 5]. Electrical insulation systems do not withstand the suddenly degradation process, but under the action of various stresses the insulation gradually undergoes irreversible structural transformations, which causes their electrical characteristics to worsen.

The ageing degree is determined by the variation of the values of the dielectric material parameters at a given time, compared to the initial values of these parameters. The ageing rate is different if all the electrical, thermal, and mechanical stressors act simultaneously, separately or in a certain sequence [4, 6].

Transformer faults generally result from the long term degradation of oil and paper due to the combination of heat (pyrolysis), moisture (hydrolysis) and air (oxidation). Due to electrical and thermal stresses that in-service power transformer experiences, oil and paper decomposition occurs, resulting in a number of gases related to the cause and effect of various faults. Gases produced due to oil decompositions are hydrogen (H_2), methane (CH_4), acetylene (C_2H_2), ethylene (C_2H_4) and ethane (C_2H_6), while carbon monoxide (CO) and carbon dioxide (CO_2) are mainly produced by paper decompositions and can be used as a trigger source for paper monitoring [7].

In the ageing process transformer oil undergoes structural changes due to the decomposition of constituent aliphatic, naphthenic and aromatic hydrocarbons [5].

Therefore, in the maintenance activity of the electrical transformers it is necessary to carry out a permanent monitoring of the electrical, physical and chemical parameters of the transformer oil.

Insulation degradation is a major concern for these aged transformers. Insulation materials in transformers degrade at higher operating temperatures in the presence of oxygen and moisture. Practicing engineers currently use a number

of modern diagnostic techniques to assess the insulation condition of aged transformers [8].

Thus, in this paper we propose to present offline methods and modern equipment used for the study and analysis of physical and chemical properties (analysis of water content, density and interfacial tension, dissolved gas analysis, and determination of furan components) and electrical properties (determination of loss factor tanδ and relative permittivity ε_r) of the transformer oil.

Samples of transformer oil type MOL TO 30.01 (uninhibited electrical insulator, non-additive) and new StaSo Transformer Oil I (high quality inhibited insulating oil) were studied: two samples collected directly from the original barrel, two samples collected from the transformer tank, after dielectric tests at the transformer's manufacturer; there were also studied two samples of used TR 30 oil, collected from two transformers.

The experimental determinations were carried out in the specialized laboratory, within The National Research, Development and Testing Institute for Electrical Engineering - ICMET Craiova .

II. Some Aspects Regarding the Liquid Electrical Insulating Materials

The liquid electrical insulating materials are those that are in a liquid state during the entire period of use and operation [1]. This category of electrical materials includes both natural and synthetic electrical insulating oils.

The chemical structure of oil is very complex, oil being made up of a large number of hydrocarbon and non-hydrocarbon molecules. The hydrocarbons consist of paraffins, naphthenes and aromatics. The non-hydrocarbons consist of acids, esters, alcohols, ketones, iron and copper. The chemical composition of the oil can have significant effects on the properties it exhibits such as oxidation behavior and dielectric strength [9].

Most liquid electrical insulating materials are flammable, which requires a lot of attention and caution in operation. Likewise, these materials are oxidizable, from this chemical process resulting gases, water, acids etc. which are factors that lead to changes in their dielectric properties [10].

Mineral oils are achieved by the frequent distillation of crude oil. Therefore, from a chemical point of view, mineral oils constitute a mixture of naphthenic, aromatic and paraffinic hydrocarbons [10, 11].

For the cleaning of unstable chemical impurities, the oils are subjected to the refining process. The refining process consists, in essence, in the treatment with sulphuric acid, neutralization with alkaline solution, washing with water, drying and settling. Another efficient method of refining is that of the Romanian engineer Lazăr Edeleanu, known in the literature as the "Edeleanu process", which is based on the specific solubility of some classes of hydrocarbons in liquid sulphur dioxide [1,10].

Transformer oil, being a non-polar material, has a low value of relative permittivity (ε_r = 2.2 .... 2.4) and the loss factor tanδ is dependent on the temperature, increasing with temperature due to the increase of electrical conductivity. The increase in temperature also influences the value of the dielectric strength due to the increase in the oxidation rate, the solubility rate and the water emulsification.

Ageing, wear and therefore degradation of the dielectric properties of transformer oils are favored by factors such as the presence of oxygen, high temperature, electric field, electric arc, light and some metals [11].

III. Experimental Results and Analysis of Some Transformer Oils

A. Test Samples

For the study of some physical, chemical and electrical properties of the transformer oil, samples of transformer oil type MOL TO 30.01 (uninhibited electrical insulator, non additive) and new StaSo Transformer Oil I (high quality inhibited insulating oil) were used in this paper: two samples collected directly from the original barrel, two samples collected from the transformer tank after dielectric tests at the transformer's manufacturer; there were also studied two samples of used TR 30 oil, collected from two transformers.

The experimental determinations were carried out in the specialized laboratory, within The National Research, Development and Testing Institute for Electrical Engineering - ICMET Craiova.

Before starting the test, in order to facilitate the recognition of each type of analyzed oil during the tests, a coding of them was carried out to ensure their identification [1]. In table I this coding is presented.

B. The Experimental Determinations

1) Visual Analysis

The visual examination is applicable to electrical insulating liquids that have been used in transformers, oil circuit breakers or other electrical apparatus as insulating or cooling media, or both. Poor transparency, cloudiness or the observation of particles indicates contamination such as moisture, sludge or other foreign matter [1,12].

A first analysis of the oils is the visual analysis which aims to establish the degree of clarity, transparency, appearance of the oil. Colour is often used as a qualitative method.

The colour of the oils, depending on the condition of the insulation system, is in the range from yellow-colourless to brown and intensifies by use when the oils become opaque by wear during the operation of power transformers [5]. In Fig. 1[1] the studied samples are depicted.

TABLE I.

Identification Codes of Tested Oils

No.	Identification codes of tested oils	
	Oil type	***Code assigned for experiment***
1	StaSo Oil, new, inhibited insulating oil	S100
2	StaSo Oil collected from the transformer tank after stand tests	S102
3	MOL TO 30.01RO oil, new, uninhibited	M200
4	MOL TO 30.01RO oil collected from the transformer tank after stand tests	M202
5	TR 30 oil, used, reddish color	300
6	TR 30 oil,used, brown	400

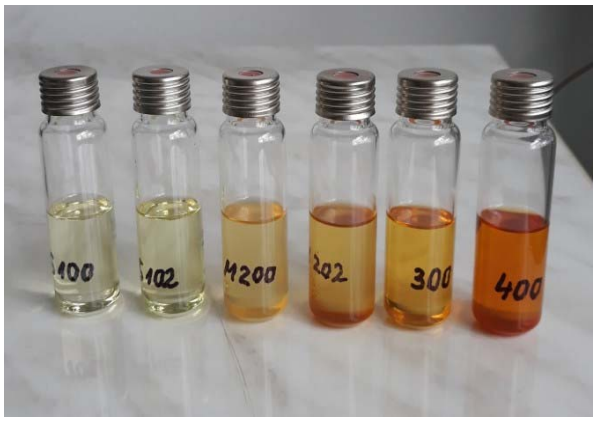

Fig. 1. The studied oil samples.

It is observed that S100 oil sample is clear, while a slight coloration appears at the S102 sample (oil after tests in the stand) and it is no longer so clear. The same observation is made for M200 and M202 oil. In the case of used oils codes 300 and 400, their reddish-brown colour is observed, which attests the state of advanced wear.

2) The Analysis of Water Content From The Oil

Water content in insulation materials increases its electric conductivity and dissipation factor and reduces dielectric strength [14].

The moisture in transformer is generated from several sources: remaining moisture in insulation during manufacturing, humid air from outside during transportation and/or assembling in substation, humid air from outside through the breather (non-sealed), moisture ingress through gaskets, chemical decomposition of cellulose, moisture absorption from outside during some maintenance operations such as on site control of active part or bushing replacement, topping-up of oil level made with humid oil (non-dried) [12].

Water is, therefore, one of the most important factors, which affects the life of the electrical insulation system of the power transformer. Water can exist in the transformer in several forms [1,5]:

- ✓ free water at the bottom of the tank;
- ✓ ice at the bottom of the transformer tank;
- ✓ water in the form of emulsion, highlighted by determining tan δ;
- ✓ dissolved water, which is determined by the Karl Fischer method;
- ✓ free water, in the situation when the oil saturation is exceeded and the formation of small drops of water begins.

The water solubility in transformer oil increases with temperature and oil neutralization index. The water absorption capacity of the electrical insulating mineral oil increases rapidly with increasing temperature (about 4-5 times higher at a temperature of 80°C than at a temperature of 20°C) [5]. This analysis, on the water content, is carried out in the laboratory using a device called coulometric titrator, which uses the Karl Fisher analysis method, the result being reported as the concentration of water in ppm (parts per million).

Fig. 2. The image of the Karl-Fisher coulometric titrator model CA-21 used in the experimental results.

TABLE II.

THE EXPERIMENTAL RESULTS

No.	The experimental results achieved regarding the amount of water contained in the oil		
	Code assigned for experiment	*Water content in ppm*	**Maximum allowed value according to the regulation** PE 129-99
1	S100	21.16	30 ppm
2	S102	24.72	
3	M200	26.54	
4	M202	11.17	
5	300	29.87	
6	400	38.21	

Fig. 2 shows the coulometric titrator type Karl-Fisher model CA-21, manufactured by Mitsubishi Japan used in the experimental results. In table II [1] the obtained experimental results are presented.

3) Determination of Electrical Insulating Oil Density and Interfacial Tension

Some theoretical aspects regarding the interfacial tension are worth specifying. It is known from chemistry and specialized literature that at the fluid interface, the Van der Waals type forces are no longer compensated but have an inward-oriented resultant. Thus, the potential energy of the molecules inside the fluid is lower than at the surface and consequently additional energy is distributed on the free surface. To create 1 cm^2 of free surface it is necessary to consume energy equal to the interfacial voltage. The interfacial tension at the surface of a fluid is determined by evaluating the force perpendicular to any segment placed on the surface of the fluid and relative to its length. The interfacial tension is quantified as a force per unit length, equivalent to the energy per unit area of the fluid. It is expressed in [N/m] in the international system or [dyne/cm] [1,6, 13]. The analysis for determining the density and the interfacial force is carried out according to the STAS 9654-74 standard.

Fig. 3. The image of the tensiometer type KSV Sigma 702ET used in experiments.

TABLE III.

THE EXPERIMENTAL RESULTS

NR.	The experimental results on the determination of density and interfacial force		
	Code assigned for experiment	***Density (g/cm^3)***	***Interfacial tension (dyne/cm)***
1	S100	0.867	40.27
2	S102	0.870	39.99
3	M200	0.849	37.01
4	M202	0.854	29.27
5	300	0.871	24.86
6	400	0.873	16.57

The equipment used for the practical determination of oil density and interfacial tension is the tensiometer type Sigma 702ET, produced by KSV Instruments Finland and equipped with thermostatic bath LAUDA RA 104, shown in Fig. 3. The tensiometer is provided with an arm in which it is hanged either a glass ball (to determine the oil density) or a Du Noüy ring (to determine the interfacial tension). The Du Noüy ring is a thin platinum wire ring with a circumference of 9.545 mm, from which a hook is welded, also made of platinum wire.The experimental results are depicted in table III [1].

4) Dissolved Gas Analysis (DGA)

Dissolved gas analysis (DGA) is one of the most widely used diagnostic tools for detecting and evaluating faults in electrical equipment filled with insulating liquid. However, interpretation of DGA results is often complex and should always be done with care, involving experienced insulation maintenance personnel [14].

The equipment with which this analysis is performed is the gas chromatograph type CLARUS 600, model 4087, produced by PerkinElmer USA. Chromatographic separation is based on the differentiated interaction of the components of a test against two phases, called: stationary phase and mobile phase (moving in relation to stationary phase).

The process takes place in a chromatographic column, or on the surface plan of a plate on which the stationary phase is deposited.

Fig. 4. The image of the chromatograph type CLARUS 600 that was used in tests

Chromatographic analysis is a coupled process between chromatographic separation and determination (detection) of separate compounds (process that is based on measuring a physical property).

The chromatogram represents the time dependence of the property measured by the chromatographic system detector. In a chromatogram we find chromatographic peaks and a baseline (constant or variable). Chromatographic separation of a mixture of *n* components should result in a chromatogram with *n* chromatographic peaks.

The chromatographic signal is called the chromatographic peak, the shape of which actually represents an image of the distribution equilibrium of the analyzed molecules between the mobile phase and the stationary phase, which occur in the chromatographic column [7].

Dissolved gas analysis was made for all the oil samples presented above. Below, the chromatogram for one of the cases is presented (oil-code 202). From the analysis of the chromatogram in Fig. 5, it is observed that the analyzed oil shows small peaks for the following gases: O_2, N_2, CH_4, C_2H_6, C_2H_4, C_2H_2, CO, CO_2, aspect that denotes their presence in the composition of the analyzed oil.

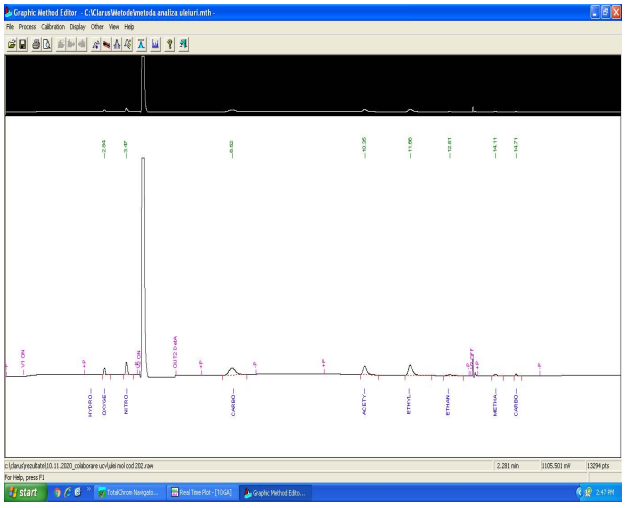

Fig. 5. The chromatogram obtained for the analysis of oil code 202.

From the analysis of the other studied oils, their chromatograms did not detect the presence of dissolved gases.

5) The Furans Determination

The furanic compounds that are mainly produced due to paper oxidation and hydrolysis processes could be directly extracted from the oil to characterize the thermal decomposition of insulation paper. The furan concentration in transformer oil depends on the mass ratio between oil and cellulose [15].

Furans are major degradation products of cellulose insulation paper and are found in the insulation oils of operational transformers [8].

The analysis was performed according to the standard SR EN 61198: 2004 [16].

This analysis was performed using HPLC 1100 High Performance Liquid Chromatograph, manufactured by SHIMADZU CORPORATION KYOTO Japan (Fig. 6).

Fig. 6. The image of the High Performance Liquid Chromatograph (HPLC 1100).

In principle, this analysis consists in determining the 2-furfural and its derivative compounds from the electrical insulating oil by the method of separating the elements into columns, characterized by different specific wavelengths and transferring them to a detector with a different degree of light absorption. It determines a distinct chromaticity for each detected furan component; it is called high performance liquid chromatography (HPLC).

Five furan derivatives are related with cellulosic insulation degradation in transformer oil; 2-Fulfural (2FAL), 2-Fulfurol (2FOL), 5- Hydroxy methyl-2-furfural (5HMF), 5-Methyl-2-furfural (5MEF) and 2-Acetyl furan (2ACF) [15].

Quantitative Results

PDA

ID#	Ret. Time	Area	Area %	Conc. ppm (mg/kg)	Name
1	2.244	1194	0.046	0.006	5-hidroximetil 2-furfural (5-HMF)
2	0.000	0	0.000	0.000	alcool 2-furfurilic (2-FOL)
3	3.560	1880	0.066	0.008	2-furfural (2-FAL)
4	0.000	0	0.000	0.000	2-aceil furan (2-ACF)
5	0.000	0	0.000	0.000	5-metil 2-furfural (5-MEF)

Grouping Results

PDA

Group#	Group Name	Conc. ppm (mg/kg)	Area
1	FURANI	0.014	3074
Total		0.014	3074

Fig.7. The content of furanic components in used oil code 400.

The analysis of the obtained results showed only in the case of the test of the oil code 400 (TR 30 oil, used, brown) the presence of the components 5-HMF (5-Hydroxy methyl-2-furfural) and 2-FAL (2-Fulfural).

6) Determination of the Dielectric Loss tanδ and The Relative Dielectric Permittivity ε_r at 90°C

These determinations are carried out simultaneously using a tester manufactured by BAUR Austria, shown in Fig. 8. The tests were carried out according to IEC 60247: 2004 [17]. The experimental results are presented in Table IV [1].

Fig.8. The image of the BAUR DTLC tester.

TABLE IV.

THE EXPERIMENTAL RESULTS

No.	The experimental results for tanδ and ε_r		
	Code assigned for experiment	*tan δ*	ε_r
1	S100	0.0030	2.12
2	S102	0.0117	2.13
3	M200	0.0041	2.09
4	M202	0.0244	2.10
5	300	0.0103	2.14
6	400	0.0888	2.17

C. *Analysis of Experimental Data*

From the analysis of the results presented in Table II, it is observed that the oil code 400 (used oil) exceeds the value of 30 ppm and the oil code 300 (also a used oil) has the amount of water very close to the limit value (29.87 ppm compared to 30 ppm). The other oil samples comply with the regulations.

In terms of density, according to [18], all analysed samples correspond to a density of less than 0.895 g/cm^3.

The interfacial tension is considered appropriate according to PE 129-99, if it has a value higher than 20 dyne/cm. From the data presented in Table III, it can be seen that only oil code 400 (used TR-30 oil) does not correspond.

According to [17], the dielectric loss factor tanδ must be a maximum of 0.004. It can be seen from the data recorded in Table IV that only the oil sample code 400 (used TR 30 oil) exceeds this value.

The value of the relative permittivity ε_r determined experimentally and recorded in Table IV falls within the known limits of the literature [10, 11].

IV. Conclusions

As it is known, both from practice and from the specialized literature, the deterioration of the insulation system is the major cause of transformer problems and failure. Thus, a first stage in establishing a proper electrical insulation is carried out in the design and testing phase of the equipment for choosing the best electrical insulation materials, with high performance.

In the operation phase of electrical equipment (electric motors and generators, electrical transformers, circuit breakers etc.), the maintenance activity aims to monitor the proper functioning of the electrical equipment.

In the case of electrical transformers, indispensable elements in electricity transmission and distribution networks, online and offline monitoring of the state of electrical insulation (solid and liquid) ensures their proper functioning by preventing the occurrence of fails that could occur and can disturb various economic processes.

It is known from the literature and practice that transformer oil plays a key role in the proper operation of transformers. The analysis of transformer oil can reveal several types of anomalies (electrical, thermal defects, premature ageing, loss of insulation capacity etc.).

This paper proposed and presented some of the modern methods of offline analysis of physical, chemical and electrical properties of transformer oil (determination of water content, density, interfacial tension, dissolved gas analysis, determination of furan components, relative permittivity and loss factor). Samples of transformer oil type MOL TO 30.01 (uninhibited electrical insulator, non-additive) and new StaSo Transformer Oil I (high quality inhibited insulating oil) were studied: two samples collected directly from the original barrel, two samples collected from the transformer tank, after dielectric tests at the transformer's manufacturer; there were also studied two samples of used TR 30 oil, collected from two transformers.

The achieved results showed that the oil samples type MOL TO 30.01 and StaSo Transformer Oil I, taken from the original barrel and from the transformer tank after specific stand tests of the electrical transformer correspond to the norms in force, while the oil samples type TR 30 taken from transformers with many hours of operation show signs of ageing [1].

Future studies will focus on the comparative analysis of other physical, chemical and electrical properties that feature the state of wear of transformer oil as well as the analysis of the solid-liquid insulation system (cellulose type insulation impregnated with transformer oil).

Acknowledgment

Source of research funding in this article: Research program of the Electrical Engineering Faculty, financed by the University of Craiova.

Contribution of authors:
First author – 25%
First coauthor –35%
Second coauthor – 16%
Third coauthor- 8%
Fourth coauthor- 16%

Received on August 27,2022
Editorial Approval on November 23, 2022

References

[1] M.E. Ardeleanu, I.G. Sîrbu, D. G. Stănescu, I.M. Burciu, and A. Scornea, "Modern methods of analysing the transformer oil," *Proc. of the 2021 Int. Conf. on Electromechanical and Energy Systems* (SIELMEN), Oct. 6-8, 2021, Iaşi, Romania, pp. 288-292.

[2] M. Ghiorghiu, C. Ghiorghiu, and D. Zlatanovici, *Checking The Insulation of Electrical Equipment* (in Romanian: *Verificarea izolației echipamentelor electrice*), Bucharest: Tehnică, 1984.

[3] G. Tănăsescu, P. Noținger, and others, "Online monitoring and diagnostic system (SMD) for AT 3200 MVA 220/110 kV from Turnu-Măgurele substation" (in Romanian: "Sistem de monitorizare și diagnosticare (SMD) on-line pentru AT 3200 MVA 220/110 kV din stația Turnu-Măgurele"), *Proc. of the 5th National Symposium - Optimization of energy services*, Buzău, Romania, 2008.

[4] M. Șerban, "The extension of the activities of producing high voltage transformer oils in specific industrial in Romanian enterprise," *Proc. of the 31-th Annual Congress of the American Romanian Academy of Arts and Sciences* (ARA), July,2007, Brasov, Romania, pp.214-218.

[5] M. Fătu, "*Studies on improving the quality of transformer oils*" Ph.D.Thesis, Transilvania University of Brasov, 2015, Brasov, Romania.

[6] M. Şerban, E. Helerea. and A. Munteanu, "Ecological vegetal oils and their competition with mineral electroinsulating oils," *Proc. of the BRAMAT Int. Conf*., Feb., 2009, Braşov, pp.6- 21.

[7] D.K Mahanta and S. Laskar, "Electrical insulating liquid: A review," in *Journal of Advanced Dielectrics*, Vol.7, No.4, 2017, pp. 1730001-1-1730001-9.

[8] T.K. Saha, "Review of modern diagnostic techniques for assessing insulation condition in aged transformers," *in IEEE Trans. on Dielectrics and Electrical Insulation*, vol.10, no.5, Oct. 2003, pp.903-917.

[9] A.C. Power, "Development in the Interpretation of Power transformer Dissolved Gas Analysis Results," Master of engineering science degree, University of New South Wales, 1992.

[10] Ch. Popescu, A. Ifrim, and others, *Electrotechnical Materials. Properties and Uses* (in Romanian: *Materiale electrotehnice. Proprietăți si utilizări*), Bucharest: Tehnică, Romania, 1976.

[11] A. Ifrim and P. Notingher, *Electrotechnical Materials* (in Romanian *Materiale electrotehnice*), Bucharest: Didactică si Pedagogică, Romania, 1979.

[12] J.S. N`cho, I. Fofana, Y. Hadjadj, and A. Beroual, "Review of physicochemical-based diagnostic techniques for assessing insulation in aged transformers", in *Power Transformer Diagnostics, Monitoring and Design Features*, Edited by Issouf Fofana, 2018, https://www.mdpi.com/journal/energies/specialissues/power-transformer.

[13] S.S. Gabrian, C. Gabrian, A. Roșca, and D. Roșca, "Interpretation of interfacial tension on mineral oils used as carriers of electrical current of high voltage," *Proc of the XVth Int. Multidisciplinary*

Conference Professor Dorin Pavel-founder of Romanian hydropower, Sebeş, Romania, 2015, pp.289-296.

[14] SR EN 60599/2016, "Electrical equipment in service filled with mineral oil. Guide for the interpretation of dissolved gas and free gas analysis" (in Romanian: "Echipamente electrice în serviciu umplute cu ulei mineral. Ghid pentru interpretarea analizei gazelor dizolvate şi a gazelor libere").

[15] A.N. Bakar, A. Abdu-Siada, and S.Islam, "A review on chemical diagnosis techniques for transformer paper insulating degradation," *Proc. of the 2013 Australasian Universities Power Engineering Conference* (AUPEC), Sept.29-Oct.03, 2012, Hobart, TAS, Australia, pp.1-6.

[16] SR EN 61198/ 2004, "Electroinsulating mineral oils. Methods for determining 2-furfural and its derivatives" (in Romanian: "Uleiuri minerale electroizolante. Metode de determinare a 2-furfural şi derivaţii săi").

[17] IEC 60247-2004- "Insulating liquids. Measurement of relative permittivity, dielectric dissipation factor (tanδ) and d.c resistivity."

[18] SREN 60296-2012- Fluids for electrical applications. New mineral oils for transformers and switchgear.

DOI: 10.52846/AUCEE.2022.05

Modeling of Thermal Transfer Parameters by Transparent Construction Elements

Felicia Elena Stan Ivan, Radu Cristian Dinu and Adelaida Mihaela Duinea
Faculty of Electrical Engineering/ Department of Electrical, Energy and Aerospace Engineering, Craiova, Romania,
fivan@elth.ucv.ro, rcdinu@elth.ucv.ro, aduinea@elth.ucv.ro

Abstract **− The article presents a case study on the modeling of heat transfer parameters through transparent construction elements. Conducting experimental studies on the scale of an entire building is very complex, on the one hand due to the size and geometric complexity of the studied objectives and, on the other hand, due to numerous random factors (climatic conditions or how the buildings are operated). In order to be able to carry out a study on the real behavior of the buildings, models are made for them, taking into account the real mode of operation of the installations related to these constructions. The present article consists in making a modeling for a simple exterior window, with a single sheet of glass that separates the interior space of an enclosure (rooms) from the exterior environment. The modeling will be performed both for the case of a building located inside a locality and for the case of the location of the building outside the locality.**

Cuvinte cheie: *transfer termic, clădiri, elemente de construcție transparente, modelare, model*

Keywords: *thermal transfer, buildings, transparent construction elements, modeling, model*

I. INTRODUCTION

Energy consumption due to buildings currently represents, in Romania, approximately 30% of the total energy consumed. This share is constantly increasing, mainly due to air conditioning systems, approaching the level registered in the member countries of the European Union, in which residential and tertiary buildings are assigned a share of energy consumption of approx. 40% of total energy consumption.

Achieving a completely global model that represents a construction in its entirety is practically impossible. As a result, each of the models made in the field of thermo technics of constructions and their related installations represents only certain aspects related primarily to the purpose for which they were made.

For example, the behavior of a building under the action of the wind will be represented differently depending on what is pursued by modeling this phenomenon. So, such a model built for the study of mechanical behavior, will represent the walls of the building by the mechanical characteristics of the materials (modulus of elasticity, limit efforts, etc.) and the wind by the force it exerts on the building. On the other hand, if a model is made for the study of the energetic behavior of the building, the thermophysical characteristics of the materials from which its walls are made (thermal conductivity, specific heat, etc.) and their permeability will be taken into account.

Also, the action of the wind will be represented, in this case, by changing the convective heat exchange coefficient achieved on the outer surface of the building envelope and by the dynamic pressure that influences the air infiltration inside the building through its joints and leaks.

In other words, modeling consists in representing an object or phenomenon in different forms starting from its initial reality, generally using simplifying hypotheses.

The modeling process essentially comprises three main stages [12]:

The construction of the physical model. It is the modeling stage that allows, on the one hand, the analysis of the physical phenomena that intervene in the model, and on the other hand, the adoption of appropriate simplifying hypotheses;

Construction of the mathematical model. In this stage, the physical model is represented, in a certain universal language, so that its degree of complexity is expressed. In the case of very simple physical models there are obvious analytical solutions, and in the case of complicated (complex) models it is necessary to resort to numerical solving;

Construction of the numerical model**.** This stage consists in assigning the values for the parameters of the mathematical model in order to obtain the model equations. At the end of this stage, a set of equations or systems of equations is obtained, in which only the variables of the problem are unknown. Depending on the complexity of the mathematical model, special numerical methods (such as the finite difference method) or the model reduction technique can be used to solve the numerical model, i.e. replacing the complex model with a much smaller model and for which solution is, however, a good approximation of the complete model.

The stages of a modeling process applied in the case of the thermal behavior of constructions (building and related installations) are [5], [12]:

Physical representation that aims at clearly defining the boundaries of the analyzed system (room, apartment or building) and its interactions with external factors (climatic parameters, thermal conditions in neighboring rooms, the action of thermal installations, the action of occupants, etc.);

Mathematical representation is the modeling stage in which the equations characteristic of the analyzed phenomena are written (energy conservation equations and heat and mass transfer equations) and the hypotheses are

formulated on the parameters (factors, coefficients, etc.) that intervene. The result of this stage is transcribed in the formulation of the equation or system of equations characteristic of the physical model and also in the clear establishment of the boundary conditions, based on the definition of the boundaries of the model from the previous stage;

Numerical representation is the stage in which the equations or system of equations established in the previous stage is transposed in numerical form, simplified according to the information on parameters and boundary conditions, numerical solving methods and available simulations, etc.

II. HEAT TRANSFER AT GLAZED SURFACES. CONVECTION HEAT TRANSFER MODELLING

The unit surface heat flux q_s is expressed by Newton's cooling law in the form of the product between a property of the system α and the force that generates the process:

$$q_s = \alpha \cdot (t_s - t_f) \tag{1}$$

Defining in this simplistic way an essentially complicated transfer mechanism gives the convection heat transfer coefficient,α, the property to encompass all the factors that determine the process. Convection heat transfer is influenced by thermodynamic and fluid dynamics factors, because at the interference between fluid and wall the heat exchange is done through the boundary layer. The hydrodynamic factors are:

a) cause of the movement: - the free movement is caused by gravitational forces determined by the temperature gradient, and the forced movement by a potential difference (pressure) created by a pump, fan or blower.

b) Hydrodynamic flow regime: laminar flow regime, Re<2,320; transient flow regime 2.320<Re<10.000; turbulent flow regime, Re>10.000.

The Reynolds criterion is determined by the relation:

$$\mathrm{Re} = \frac{w \cdot d}{\upsilon} \tag{2}$$

where: w - is the velocity of the fluid, [m/s];d - equivalent hydraulic diameter, [m];υ - kinematic viscosity, [m^2 /s].

c) The character of the flow: - subsonic, sonic, supersonic, taking into account the problems specific to each type.

Thermophysical factors:

a) The temperature difference between the wall and the fluid: - for temperature differences Δt>500°C the radiant effect is also taken into account in the calculations.

b) Flow behaviour: Newtonian fluids or non-Newtonian fluids.

c) The thermophysical parameters of the fluid: - the density, ρ, the specific heat at constant pressure, c_p, the kinematic viscosity, υ and the coefficient of thermal conductivity, λ, have a great influence on the thermal convection. The average value of the convection coefficient α between a fluid and a wall is obtained from the relation:

$$\alpha = \frac{q}{t_p - t_f} \ [\mathrm{W/m^2 \cdot K}] \tag{3}$$

For different hydrodynamic regimes and geometric conditions, the values of the convection coefficientα, are obtained from criterion equations of form: For different hydrodynamic regimes and geometric conditions, the values of the convection coefficientα, are obtained from form criterion equations:

$$Nu = f(\mathrm{Re}, Gr, \mathrm{Pr}, ...) \tag{4}$$

Determining the values of the similarity criteria for that case, we obtain the numerical value of the Nusselt criterion according to which the average value of the convection coefficient is obtained:

$$\alpha = Nu \cdot \frac{\lambda_f}{l} \tag{5}$$

where: λ_f - thermal conductivity of the fluid, [W / m·K]; l - the characteristic length of the solid wall, [m]. The average value of α along an area S is obtained by the relation:

$$\alpha = \frac{1}{S}\int_S \alpha_x \cdot dS = C \cdot x^{-n} \ [\mathrm{W/m^2 \cdot K}] \tag{6}$$

Convection heat transfer and the intervention of this mode of heat exchange in the entire heat exchange from indoor to outdoor air, is based on free convection, being studied from this point of view.

Free convection occurs due to the relatively low level of air speed and is manifested by the flow of hot or cold air along the construction elements. In the case of high air velocities, thermal convection can be studied from the point of view of mixed or even forced convection, but the effects of this modeling would be to obtain high values of heat transferred between the two areas (indoor / outdoor).

As previously stated, the fundamental law of convective heat transfer is known as Newton's Law and allows the calculation of heat flux Q, proportional to the heat exchange surface, S, and the temperature difference between wall temperature and fluid:

$$Q = S \cdot h \cdot (T_s - T_f) \quad [\mathrm{W}] \tag{7}$$

with:α- thermal convection coefficient, [W / (m^2·K)], which depends on several variables (temperature, velocity, thermal conductivity, viscosity, specific heat, density, etc.) and is calculated for turbulent motion, and laminar with the help of criterion relations.

In order to establish the criteria for calculating the thermal convection coefficient, it is necessary to know the convection type. So:

-for natural convection, the characteristic parameter is the Grashof number, in which case, the modeling of the thermal convection coefficient is done based on the relation:

$$h = C \cdot (Gr \cdot \mathrm{Pr})^n \cdot \frac{\lambda_f}{l} \ [\mathrm{W/m^2 \cdot K}] \tag{8}$$

for forced convection, the characteristic parameter is the Reynolds number, in which case, the modeling of the thermal convection coefficient is done based on the relation:

$$h = C \cdot \mathrm{Re}^{0,8} \cdot \mathrm{Pr}^{n} \cdot \frac{\lambda_f}{l} \ [\mathrm{W/m^2 \cdot K}] \quad (9)$$

were: $Gr = \frac{g \cdot l^3 \cdot \beta \cdot \Delta T}{\upsilon^2}$ - Grashof criterion; $\mathrm{Pr} = \frac{\upsilon}{a}$ - Prandtl criterion; $\mathrm{Re} = \frac{v \cdot l}{\upsilon}$ - Reynolds criterion; λ_f - thermal conductivity of fluids (in our case air), established from the literature as a function of temperature, [W/(m^2·K)]; l - the characteristic length of the solid element (construction element), [m]; g=9,81 m/s^2 – gravitational acceleration; $\beta = \frac{1}{T_m}$ - isobar coefficient of volume variation, for gases considered ideal, [K^{-1}]; ΔT – solid-fluid temperature difference, [K]; $\upsilon = \frac{\eta}{\rho}$ - the kinematic viscosity of the fluid (in our case, the air), determined as a function of temperature as the ratio between the dynamic viscosity of the fluid, η, and the density of the fluid, ρ; $a = \frac{\lambda}{\rho \cdot c}$ - thermal difussion coefficient, [m^2/s] determined according to the energetic characteristics of the construction element (thermal conductivity of construction material, λ, density of construction material, ρ, specific heat of the material, c);

C, m, n – experimental constants characteristic of each type of movement.

III. CASE STUDY FOR MODELLING THERMAL TRANSFER PARAMETERS BY TRANSPARENT CONSTRUCTION ELEMENTS

Based on the theoretical aspects regarding the modeling of heat transfer at the level of the envelope elements of a building, the following will establish the parameters that characterize the heat transfer processes at the level of the glazed elements of the tire (windows): the internal coefficient of thermal convection, α_i,[W/(m^2·K)]; the external thermal convection coefficient, α_e,[W/(m^2·K)]; global heat transfer coefficients, k_{FE}, [W/(m^2·K)]; thermal resistance of the glass, R_{FE}, [(m^2·K)/W]; heat flux density at the inner face, q_i, respectively outer face, q_e, of the glass, [W/m^2]; total heat flow transmitted through the window, Q_{FE}, [W];

For this purpose, it is considered a simple exterior window, with a single sheet of glass that separates the interior space of an enclosure (room) from the external environment, having the dimensions represented in figure 1.

From the analysis of the part of the studied room, it is observed that the dimensions of the studied window are: width l_{fer} = 220 cm, height h_{fer} = 300 cm.

In order to evaluate the parameters that characterize the thermal transfer processes at the window level, the following hypotheses are made:

- the outdoor temperature, θ_e, taken into account is represented by the average annual temperature of the cold period, corresponding to climate zone II [2];

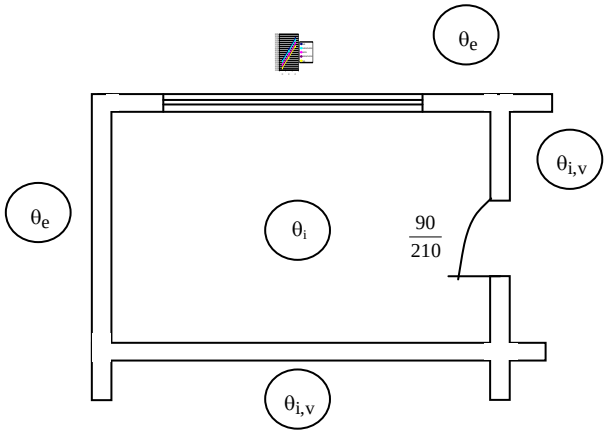

Fig.1. Location of the window in the structure of the building envelope: θe - outside air temperature, [°C]; θ_i - the temperature of the air inside the enclosure considered, [°C], $\theta_{i,v}$ - the air temperature inside the spaces adjacent to the enclosure considered, [°C]

- the air temperature inside the studied room, θ_i, is considered to be the one specific to the thermal comfort established by the norms in force, depending on the destination of the room [7]: $\theta_i = +18^{\circ}C$; $\theta_i = +20^{\circ}C$; $\theta_i = +22^{\circ}C$;

- the intensity of the solar radiation, I_{Tj}, is established for each case, depending on the cardinal orientation "j", of the window and of the locality in which the building is located [2];

- the window is made with ordinary glass, having the absorption coefficient, α_a = 0.10;

- calculation wind speed, established depending on the wind distribution of the localities and the location of the building (inside or outside the locality;

- the air speed inside the room is considered v_i = (0.10 ... 0.15) m/s, considered as a value allowed for comfort conditions in terms of indoor air speed (free convection);

- the window is considered to be: with ordinary glass on the woodwork and wooden frames, in which case the thermal resistance of the window is considered in a first approximation R_0 = 0.19 (m^2·K)/W - FEI [7]; with ordinary glass on the chopping board and metal frames, in which case the thermal resistance of the window is considered in a first approximation R_0 = 0.17 (m^2·K)/W - FEII [7]; with thermal insulation glass on woodwork and wooden frames, in which case the thermal resistance of the window is considered in a first approximation R_0 = 0.33 (m^2·K)/W - FEIII [7]; with thermal insulation glass on the woodwork and metal frames, in which case the thermal resistance of the window is considered in a first approximation R_0 = 0.28 (m^2·K)/W - FEIV [7].

To exemplify the calculation algorithm, the situation was chosen in which the window with the dimensions in figure 1, is with ordinary glass on the woodwork and wooden frames and separates two air zones with temperature inside θ_i = + 20°C, and outside θ_e = + 7.5°C, (v = 4.5 m/s) with S direction orientation and an indoor air speed of 0.1 m/s. The calculation algorithm involves the following steps [6]:

1. Determine the convection coefficient on the inside of the window with the expression:

$$\alpha_i = C \cdot (Gr \cdot \Pr)^n \cdot \frac{\lambda_f}{l} \text{ [W/m}^2\text{·K]} \quad (10)$$

$$Gr = \frac{g \cdot l^3 \cdot \beta \cdot \Delta T}{\upsilon^2} \quad (11)$$

$$l = 2 \cdot l_{fer} + 2 \cdot h_{fer} \text{ [m]} \quad (12)$$

The average thermodynamic temperature is determined as the arithmetic mean between the temperature of the air inside the considered room, and the temperature on the inside of the window, $\theta_{fer,\,i}$.

The temperature on the inside of the window is determined by considering the thermal resistance at the surface of the construction elements (window) as $R_{i,fer}$ = 0.125 m^{2}K/W [7]:

$$\theta_{fer,i} = \theta_i - R_{i,\,fer} \cdot \frac{\theta_i - \theta_e}{R_0} \text{ [°C]} \quad (13)$$

The thermal conductivity of air, λ_f, is determined by its (air) temperature

As a result, the convection coefficient on the inner face of the glass will be, for a first approximation (figure 1).

2. Determine the convection coefficient on the outer face of the glass with the calculation expression for smooth surfaces:

$$\alpha_e = a + b \cdot v^n \text{ [W/m}^2\text{·K]} \quad (14)$$

3. Calculate the actual temperature recorded on the inner surface of the glass and, if the value obtained is cu1% different from the value obtained by the initial approximation, validate the value of the internal convection coefficient, and determine the other parameters with this value.

$$\theta_{fi} = \theta^* + \frac{\alpha_a \cdot I}{\alpha_i + \alpha_e} [^\circ C] \quad (15)$$

$$\theta^* = \frac{\alpha_i \cdot \theta_i + \alpha_e \cdot \theta_e}{\alpha_i + \alpha_e} \text{ [°C]} \quad (16)$$

The calculation error compared to the initial approximation is:

$\varepsilon_{\theta,\,fi} = \dfrac{\theta_{fi}^{(1)} - \theta_{fi}^{(2)}}{\theta_{fi}} < \pm 1\% \Rightarrow$ the internal convection coefficient is $\alpha_i = \alpha_i^{(2)} = 3{,}583\ W/(m^2 \cdot K)$.

4. Determine the overall heat transfer coefficient of the glass:

$$k_{FE} = \frac{1}{R_{FE}} = \frac{\alpha_i \cdot \alpha_e}{\alpha_i + \alpha_e} \text{ [W/m}^2\text{K]} \quad (17)$$

5. The total thermal resistance of the window is determined:

$$R_{FE} = \frac{1}{k_{FE}} \text{ [m}^2\text{K/W]} \quad (18)$$

6. Determine the heat flux density on the inside of the window:

$$q_i = k_{FE} \cdot (\theta_i - \theta_e) - \frac{k_{FE} \cdot \alpha_a \cdot I}{\alpha_e} \text{ [W/m}^2\text{]} \quad (19)$$

7. Determine the heat flux density at the outer face of the window:

$$q_e = k_{FE} \cdot (\theta_i - \theta_e) + \frac{k_{FE} \cdot \alpha_a \cdot I}{\alpha_i} \text{ [W/m}^2\text{]} \quad (20)$$

8. The total heat flow transmitted through the window is:

$$Q_{FE} = k_{FE} \cdot S_{FE} \cdot (\theta_i - \theta_e) \text{[W]} \quad (21)$$

For all the situations taken into account in the calculation assumptions mentioned above, the values obtained by modeling the heat transfer at the level of the single window, with a single sheet of glass, variations in the density of heat fluxes on the inside, qi, respectively outside, q_e, glass and total heat flux transmitted through the window, Q_{FE}, depending on the type of window and their geographical orientation being presented, in case the indoor temperature is 18°C, in the diagrams in figures 2 ... 4.

Table 1 shows a centralized calculation example following the modeling of heat transfer at the level of the single window, with a single sheet of glass, for southern orientation, corresponding to climate zone II (θe = + 7.5°C) and air temperature interior θi = 18°C. The variations of the density of the thermal fluxes at the inner face, qi, respectively the outer face, q_e, of the glass and of the total heat flux transmitted through the window, QFE, are determined.

Also, in order to highlight the variations of the parameters that define the heat transfer through the glass envelope elements of a building depending on the variations of the internal air temperature, in the diagrams from figures 5 ... 7, the variations of these parameters are presented, for the case of the window type 1 (it is the most common type of simple window found in constructions in Romania).

TABLE I.
PARAMETERS OF HEAT TRANSFER SIMPLE OUTER WINDOW WITH A SHEET OF GLASS, ORIENTED IN THE CARDINAL DIRECTION SOUTH, CORRESPONDING TO THE CLIMATIC ZONE ($\theta_E = +7.5°C$) AND THE TEMPERATURE OF THE INDOOR AIR $\theta_I = 18°C$

Crt. no.	Parameter	Location/window type							
		Inside town				Outside town			
		FEI	FEII	FEIII	FEIV	FEI	FEII	FEIII	FEIV
1.	Characteristic window lenght, l, [m]	10,40				10,40			
2.	Temperature on the inner surface of the window for the first approximation, $\theta_{fer}^{(0)}$,[°C]	11,092	10,279	14,023	13,313	11,092	10,279	14,023	13,313
3.	Isobaric coefficient of volume variation, $\beta \cdot 10^{-3}$, [K^{-1}]	3,49	3,49	3,49	3,49	3,49	3,49	3,49	3,49
4.	The room interrior temperture difference, ΔT, [K]	8,802	8,856	8,795	8,797	9,097	9,153	9,092	9,093
5.	the kinematic viscosity of the fluid (in our case, the air), inside the, $\upsilon \cdot 10^{-6}$, [m^2/s]	14,880	14,880	14,880	14,880	14,880	14,880	14,880	14,880
6.	Grashof criterium, $Gr \cdot 10^{12}$	1,530	1,539	1,529	1,529	1,582	1,592	1,581	1,581
7.	Prandtl citerium for the interior air inside the room, Pr	0,7034	0,7034	0,7034	0,7034	0,7034	0,7034	0,7034	0,7034
8.	Productl $(Gr \cdot Pr) \cdot 10^{12}$	1,076	1,083	1,075	1,075	1,113	1,120	1,112	1,112
9.	Coefificient C	0,135	0,135	0,135	0,135	0,135	0,135	0,135	0,135
10.	Exponent n	0,333	0,333	0,333	0,333	0,333	0,333	0,333	0,333
11.	Thermal conductivity for the air inside the room, λ_f, [W/m·K]	0,02574	0,02574	0,02574	0,02574	0,02574	0,02574	0,02574	0,02574
12.	Convection coefficient on the inside side of the window, α_i, [$W/m^2 \cdot K$]	3,4208	3,4278	3,4198	3,4201	3,4592	3,4663	3,4585	3,4587
13.	Temperature on the inner surface of the window, θ_{fer}, [°C]	9,1936	9,1959	9,1932	9,1933	8,8996	8,9016	8,8994	8,8995
14.	Convection coefficient on the out side of the window,, α_e, [$W/m^2 \cdot K$]	23,25	23,25	23,25	23,25	29,10	29,10	29,10	29,10
15.	The overall heat transfer coefficient of the glass, k_{FE}, [$W/m^2 \cdot K$]	2,9821	2,9874	2,9813	2,9815	3,0917	3,0974	3,0911	3,0912
16.	Total thermal resistance of the window, R_{FE}, [$m^2 \cdot K/W$]	0,3353	0,3347	0,3354	0,3354	0,3235	0,3229	0,3235	0,3235
17.	Heat flux density on the inside of the window, q_i, [W/m^2]	30,1252	30,1789	30,1173	30,1195	31,4796	31,5378	31,4739	31,4755
18.	Heat flux density on the outside of the window, q_e, [W/m^2]	39,3752	39,4289	39,3673	39,3695	40,7296	40,7878	40,7239	40,7255
19.	The total heat flow transmitted throw the window, Q_{FE}, [W]	206,66	207,03	206,60	206,62	214,25	214,65	214,21	214,22

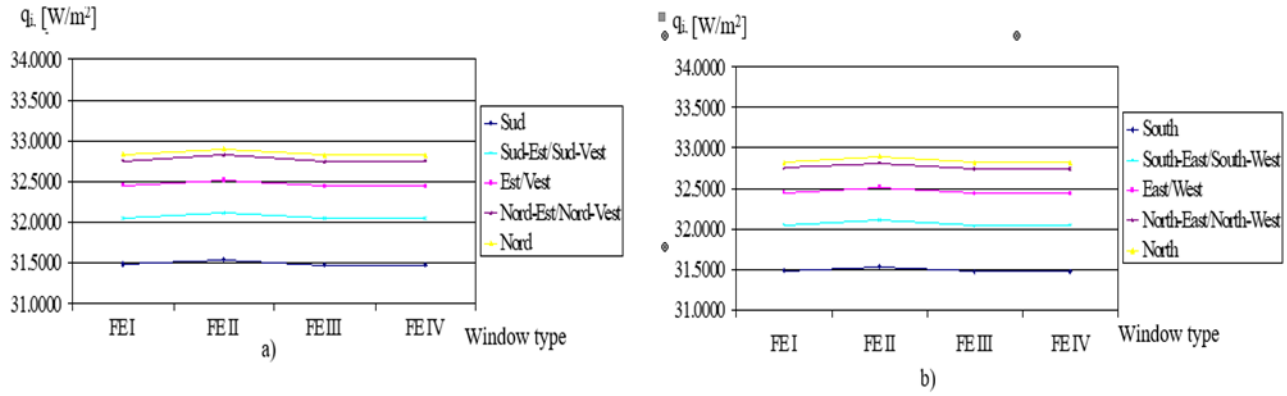

Fig.2.Variations in heat flux density on the inside of the window, depending on its type:
a) location inside the locality; b) location outside the locality.

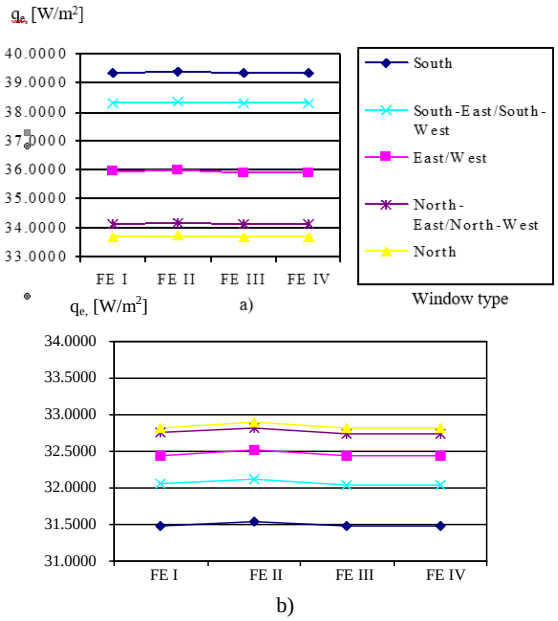

Fig. 3. Variations in heat flux density on the outside of the window, depending on its type: a) location inside the locality; b) location outside the locality.

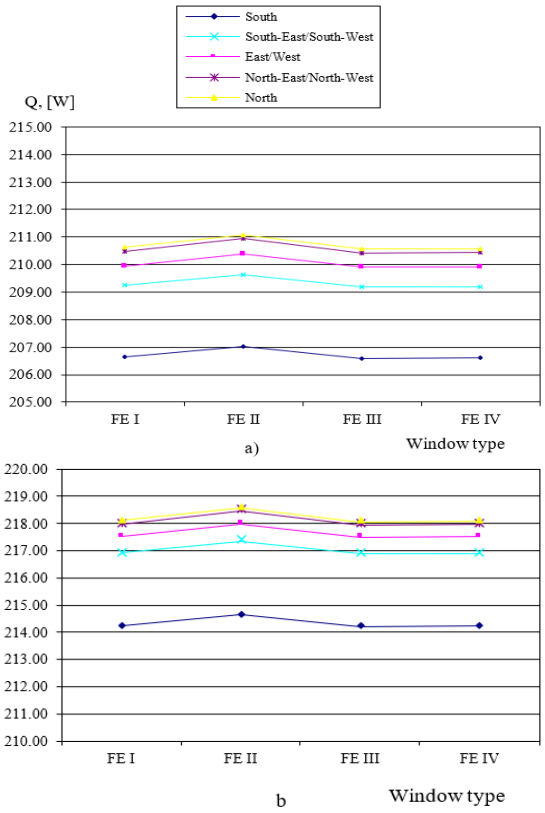

Fig.4.Variations in the total heat flux transmitted through the window, depending on its type: a) location inside the locality; b) location outside the locality.

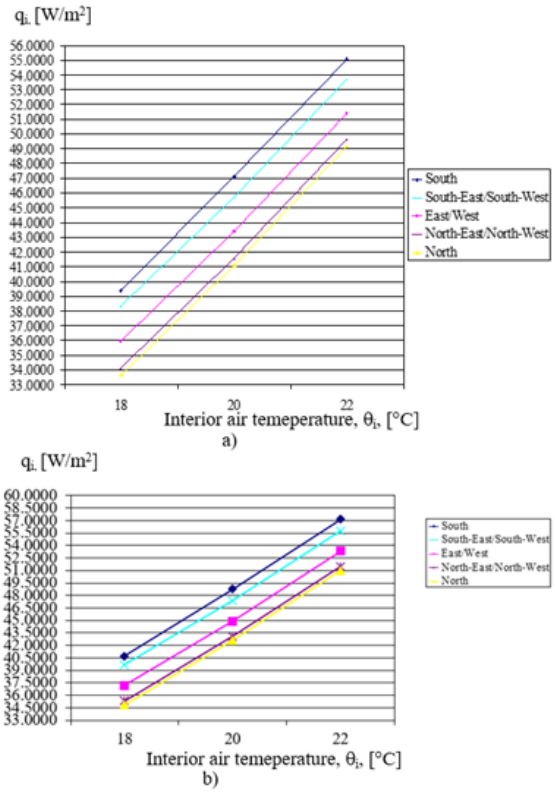

Fig 5.Variations in the heat flux density on the inside of the simple type I window, depending on the indoor air temperature and the location of the building: a) location inside the locality; b) location outside the locality.

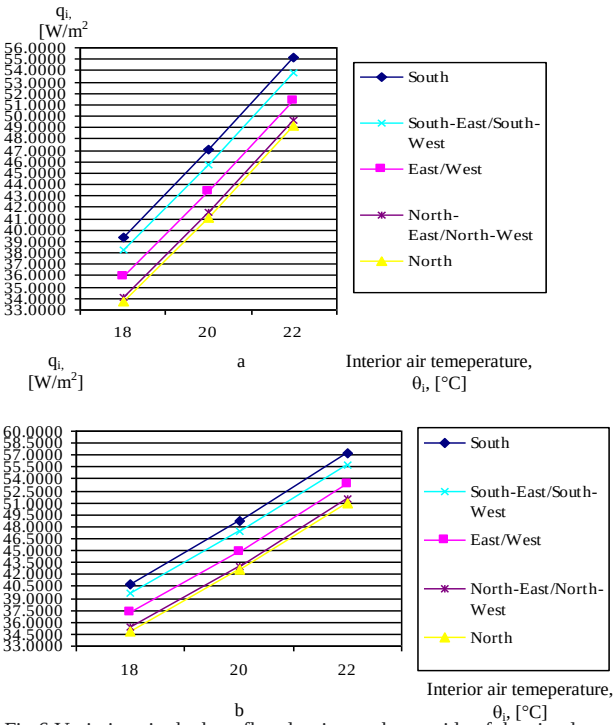

Fig.6.Variations in the heat flux density on the outside of the simple type I window, depending on the indoor air temperature and the location of the building: a) location inside the locality; b) location outside the locality.

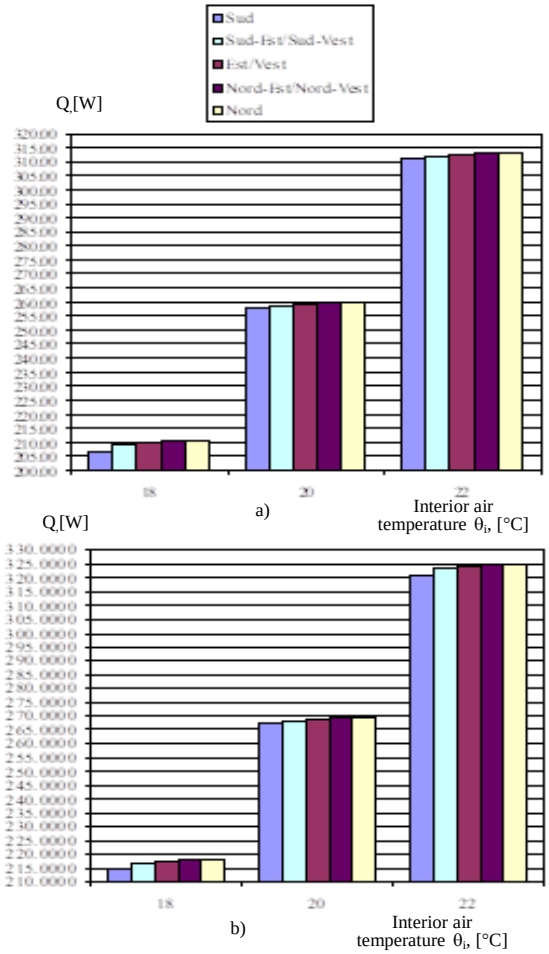

Fig.7.Variations of the total heat flux transmitted through the simple type I window, depending on the indoor air temperature and the location of the building: a) location inside the locality; b) location outside the locality.

IV. CONCLUSIONS

When modeling the radiant heat transfer, using the fictitious room calculation method, an explicit writing of the radiated heat fluxes between the considered surface and the fictitious room is obtained, which has the effect of eliminating the laborious solution of the linear system of radio modeling equations. Also, the application of this method of modeling radiant heat transfer introduces errors that can characterize a radiant balance other than zero, because the modeling does not take into account the actual exchange of heat by radiation between different surfaces of the room.

Elimination of this drawback is possible by calculating a real radiant balance and allocating the non-closing error by weighted measurement in relation to the surfaces. By doing this, the net flow values for each of the room surfaces are corrected by successive iterations.

By comparing the three families of models presented in the paper (approximation of form factors, fictitious room and radiant thermal resistances) that allow the calculation of the heat flux transmitted by radiation in mono zoned and multi zone models with the radiosity method, leads to minor differences (<10%) in the case of form factors close to 1, provided that the radiant heat transfer balance is prepared as accurately as possible.

The use of the three methods for estimating the radiant heat exchange in a room (approximation of form factors, fictitious room and radiant thermal resistance) leads to relevant results if no conditions other than those currently accepted in behavioral analyzes are required. thermal properties of buildings and their installations (gray and diffuse surfaces for the two spectral domains - large and short wavelength, isothermal surfaces and air considered a transparent medium for thermal radiation). From the analysis of the results obtained after simulating the heat transfer through a simple window, the following conclusions can be drawn:

The convergence of the real value of the temperature on the inner face of the simple windows presupposes in most cases the performance of 3 iterations;

The temperature on the inside of the window varies from 8.6976°C in the case of single type III window, to the location outside the locality and indoor air temperature of + 18°C, to a maximum of 9.8735°C in the case of single type II window , at the location inside the locality and a temperature of + 22°C;

The thermal convection coefficients on the inside of the window show quite small fluctuations depending on the indoor air temperature and the absorption of solar radiation (between 3.4918 W / (m^2·K) and 3.8440 W / (m^2·K)), being as value <4 W / (m^2·K);

The geographical orientation of the window, through the absorption index of solar radiation, influences the value of heat loss, regardless of the type of window, noting that the decrease of this parameter results in an increase in heat loss through the window;

In relation to the geographical orientation, so to the coefficient of absorption of solar radiation, it is observed that the unit heat flux to the inner face of the window increases with the reduction of solar radiation intensity, having values close to the values of unit heat flux to the outer face of the window. At high intensities of solar radiation q_i = (30.1252…31.4475) W/m^2, respectively q_e = (39.3752…40.7255) W/m^2, i.e. a difference of approximately (9.25 ...9,79) W/m^2, unlike if the intensity of the solar radiation is lower, in which case, q_i = (31,6467… 32,8823) W/m^2, respectively q_e = (33,6767…34,8523) W/m^2, i.e. a difference of approximately (2.03...1.97) W/m^2;

The value of the convection coefficient on the outer face of the single window, with a window, regardless of its type, varies depending on the calculation wind speed, increasing almost 1.25 times for an increase in wind speed by 1.5 m/s, of at 23.25 W/(m^2·K) in case of location of the building inside the locality at 29.10 W/(m^2·K) in case of location of the building outside the locality;

The heat flow transmitted from the inside of the room to the outside environment depends on both the overall heat transfer coefficient and the temperature difference between the two environments separated by the window.

Thus, the global heat transfer coefficient has the lowest value in the case of the simple type III window, at the location in the locality of the building to which the respective window belongs and at an indoor air temperature of + 18°C (2.9813 W/(m^2·K)), which leads to a heat loss of 206.60 W, and the highest value is recorded in the case of a simple type IV window, outside the location of the building and at an indoor air temperature of + 22°C

(3.3948 W/(m^2·K)), which leads to a heat loss of 324.88 W. It is observed that at an increase of 13.87% of the global heat transfer coefficient, results in an increase in heat loss by more than 50%;

Heat losses through single windows reach the highest values in the case of simple type IV windows, in the case of buildings located outside the localities, regardless of the orientation and temperature of the air inside the room.

ACKNOWLEDGMENT

Source of research funding in this article: Research program of the Electrical Engineering Department financed by the University of Craiova.

Contribution of authors:
First author – 50%
First coauthor – 25%
Second coauthor – 25%

Received on July 50, 2022
Editorial Approval on November 18, 2022

REFERENCES

[1] Bică, M., Călbureanu, M., ș.a., *Transfer de căldură şi masă*, Editura ICMET, Craiova, 2003.

[2] Cocora, O., *Auditul şi expertiza termică a clădirilor şi instalaţiilor aferente*, Editura MatrixRom, Bucureşti, 2004.

[3] Duinea, A.,M., Mircea, I., *Procese de transfer de căldură şi masă în instalaţii termoenergetice*, Editura Universitaria Craiova, 2006.

[4] Ilina, M., Lungu, C., *100 de probleme practice de instalaţii de încălzire,* Editura MatrixRom, Bucureşti, 2005.

[5] Iordache, F., Băltăreţu, F., *Modelarea şi simularea proceselor dinamice de transfer termic*, Editura MatrixRom, Bucureşti, 2002.

[6] Iordache, Fl., Caracaleanu, B., Iordache, V., *Termotehnica construcţiilor. Culegere de probleme rezolvate,* Editura MatrixRom, Bucureşti, 2007..

[7] Mircea I., Dinu R.C., *Producerea energiei electrice şi termice, partea a-II-a*, Editura Universitaria, 2006.

[8] Mircea, I., ș.a., Conversia energiei şi energetică generală. Tabele, formule termotehnice şi aplicaţii pentru uzul studenţilor, Reprografia Universităţii din Craiova, 1999.

[9] Naghi, M., Bică, M., *Transfer de căldură în regim nestaţionar,* Editura Universitaria, Craiova, 2000.

[10] Stan - Ivan, F.,E., *Transfer de căldură şi masă,* Referat Teză de Doctorat, Craiova, 2006**.**

[11] Stan - Ivan, F.,E., Mircea, I., *Eficienţa energetică şi economică a clădirilor*, Editura SITECH, Craiova, 2014.

[12] Teodosiu, C., *Modelarea şi simularea sistemelor în domeniul instalaţiilor pentru construcţii,* Editura MatrixRom, Bucureşti, 2007.

DOI: 10.52846/AUCEE.2022.06

Exhaustive Optimization Method Applied on Electromagnetic Device

Alin-Iulian Dolan

University of Craiova, Faculty of Electrical Engineering, Craiova, Romania, adolan@elth.ucv.ro

***Abstract* –This paper presents the application of an exhaustive optimization method based on the design of experiments (DOE) and the finite element method (FEM), with the aim of improving the actuation force developed by a DC electromagnet. The optimization of this device has been the subject of several previous works, allowing comparisons between the optimization methods applied in terms of the obtained precision and the workload. According to previous studies, two geometric parameters (the angle ratio of the support tip and the coil shape ratio) are very influential on the force developed at the maximum air gap. Thus, the exhaustive optimization method took into account these two parameters for its maximization, having as constraints the maintenance of the global dimensions of the device (external radius, the height of carcass, height of the plunger with support) and of the cross-section of the winding. The optimization algorithm used the results of 2-D FEM numerical experiments carried out with the FEMM program in combination with the LUA language and is based on the response surface methodology (RSM) and analysis of variance (ANOVA). Second-order polynomial models of the objective function were calculated using full factorial designs with three levels per factor. After three iterations, a very good result was obtained, comparable to those obtained by other methods, but with a significant cost in terms of workload, the optimum obtained being a global one.**

Cuvinte cheie: *optimizare, proiectarea experimentelor, metodologia suprafeţelor de răspuns, analiză dispersională, metoda elementelor finite 2-D.*

Keywords: *optimization, DOE, RSM, ANOVA, 2-D FEM.*

I. INTRODUCTION

Finite element modeling (FEM) techniques successfully replace real experiments, making significant contributions to solving problems in electromagnetism, especially when combined with the design of experiments (DOE) technique [1], [2].

The electromagnet is an electrical equipment designed to transform electrical energy into mechanical energy, developing a force that acts on a moving armature. It is often found in switches, relays and valves due to its simplicity of construction, reliability and low cost. Many scientific works have presented studies on improving the performance in terms of the force developed, based on the analysis of the magnetic field through FEM and different optimization techniques, aiming at reducing the reluctance of the magnetic circuit and increasing the magnetic flux density in the air-gap [3] – [27].

In [3] was presenteda 3-D axial-symmetric finite element method analysis combined with the quadratic sequential programming (SQP) to optimize of the geometric shape of the plunger of a DC actuator for increasing the static thrust characteristic. In [4] was created a 3-D shape optimization algorithm combining the geometric parameterization of the design surface with B-spline technique and design sensitivity analysis to optimize the pole face of an electromagnet, obtaining a uniform distribution of magnetic field on the target region from the air gap. In [5] was used the level set based topology optimization to maximize the actuating force, subject to limited usage of ferromagnetic material.

The work [6] presented structural topology optimization of an electro/permanent magnet linear actuator. The used tools are Maxwell Stress Tensor (MST) approach coupled with FEM for magnetic force computation, the adjoint method for the optimization sensitivity analysis and the sequential linear programming (SLP) for solving the optimization problem.

The response surface technology (RSM), DOE, FEM and SLP were combined in [7] to optimize a linear actuator with permanent magnet for driving a needle in a knitting machine.

In [8] was proposed an optimized topology of a solenoid with unified coil that operates valves in aircraft engine under harsh environmental conditions and high endurance requirements. The solution aims at developing higher force for the constrained size or the same force for less size and weight of the solenoid. In [9] was presented an optimization technique for average electromagnetic force of an actuator.

In [10] was performed a shape optimization of the plunger of an electromagnetic actuator in order to obtain linear static characteristic. Using suitable genetic algorithms, it is proven that the properly shaped plunger can strongly influence its static characteristic. In [11] was discussed a technique of optimal design for actuators with permanent magnet for the class of medium voltage of vacuum circuit breakers. Using the RSM technique combined with FEM are obtained improvement of dynamic characteristics and minimization of permanent magnet weight.

The influence of the plunger shape on the developed force of a DC electromagnetic actuator and on its time response were presented in [12]. The optimization of the plunger shape was made using a 2-D axial-symmetric model by genetic algorithm and the analysis of magnetic subsystem of actuator was performed by FEM implemented with ANSYS Electronics software.

The paper [13] presented the maximization of the magnetic force of an actuator which tends to be highly dependent on the geometry around air gap. Using the approach of MST through the isogeometric analysis for

force computation, the optimization problem is solved using a gradient-based algorithm of modified method of feasible directions. The research in [14] brought a new level-set-based topology optimization method for magnetic actuator design using two remeshing techniques: the modified adaptive mesh method and the extended finite-element method (XFEM). The tools were used to maximize the magnetic force under the constraint of the ferromagnetic material volume.

In [15] was presented an optimization technique based on a parametric and topology optimization method for determination of the optimized configuration of a permanent magnet actuator (PMA), maximizing the magnetic force subject to an unchangeable volume fraction constraint for each material.

As one of the branches of DOE, the RSM was used in combination with FEM in [16] to make a screening of significant parameters of an electrical motor in order to optimize its performances. The same techniques were applied in [17] to improve an electromagnet in magnetic levitation system based on many design variables.

The maximization of the force developed by an electromagnetic actuator was often an appropriate case study to prove and validate different optimization techniques. The SQP method was applied in [18] to a linear actuator after validation of a shape sensitivity analysis of magnetic forces by the MST approach and FEM. Improvement of static characteristic of an electromagnet was made in [19] by the same tool.

In [20] was successfully performed the maximization of the clamping force of an electromagnetic linear actuator with divided coil excitation by using RSM.

Coupling the RSM with 2-D FEM was applied in [21] to develop mathematical relationships between input design parameters and output performance parameters of a tubular permanent magnet brushless linear motor with Halbach magnet array, in order to optimize its efficiency, specific power and cost.

In recent papers [22], [23] were presented optimal solutions of a DC electromagnet (Fig. 1) providing a maximi-zed static force characteristic [22], respectively, a maximum electromagnetic force related to the largest air-gap (actuating force) [23], preserving the global dimensions of the device and the cross-section of the winding. The used tools were DOE and 2-D FEM.

Two parameters were taken into account to maximize the static characteristic in [22] and three parameters were used to maximize the acting force in [23].

The work [25] carried out previous analyses proposing an optimal shape of the same DC device, subject to the same constraints, expanding research on a fourth geometrical parameter. To justify the use of these four parameters in the optimization process, was performed a screening of DC electromagnet that has proved that all the four parameter have best influence on the static force characteristic, with 99% confidence.

These are the angle ratio support tip k_β, the coil shape ratio k_b, the support thickness ratio k_{a1}, and the support height ratio k_v:

$$k_\beta = \frac{\beta}{\beta_1} \in [0.67 \div 1.33] \quad (1)$$

$$k_b = \frac{h_b}{g_b} \in [6 \div 8] \quad (2)$$

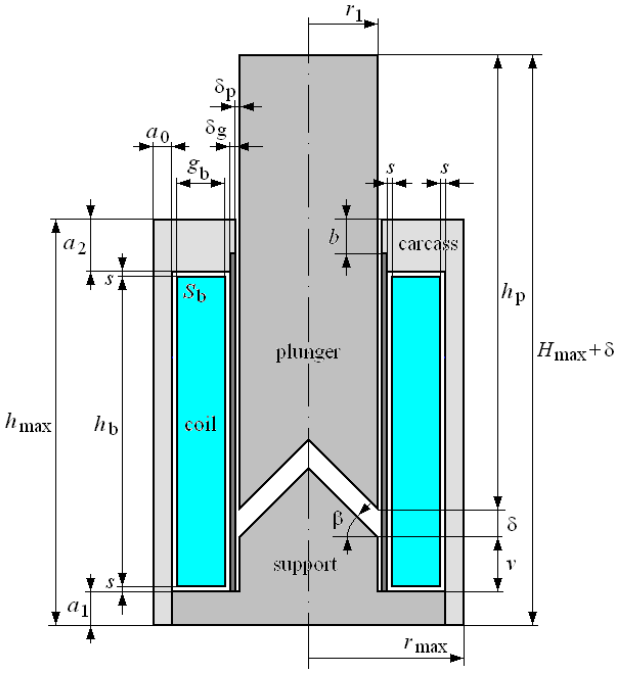

Fig. 1. Geometry of DC electromagnet [22].

$$k_{a1} = \frac{a_1}{a} \in [0.9 \div 1.1] \quad (3)$$

$$k_v = \frac{v}{h_b} \in [0.15 \div 0.20] \quad (4)$$

where $\beta_1 = 45°$ is initial value of the angle β and $a = 14.90$ mm is the initial value of support thickness.

The studies continued in the work [26] with the extension to six of the number of parameters taken into account to the maximization of the actuating force, using the optimization method based on zooms in experimental domain.

The design methodology [24] indicates the initial values of geometrical parameters with their ranges and Table I summarizes them [22]. The air-gap varies in range $\delta = [1 \div 41]$ mm, the winding has $N = 1269$ turns of standard diameter $d = 0.8$ mm and the rated voltage is $U_r = 110$ V DC. For $\delta = [10 \div 41]$ mm and $\delta = [1 \div 10]$ mm the currents are $I_1 = 12.92$ A, respectively, $I_2 = 6.90$ A, depending on absence or presence of an economy resistor.

In Fig. 2 are done the magnetization curves of the core of steel (plunger with support) and of the carcass of cast iron [22].

All the optimization methods used in works [22], [23], [23], [26] are methods that allow the determination of an local extremum, which can be the global one if the initial point with which the algorithm starts is placed in its vicinity.

The present paper aims to verify whether in the optimization problem having the actuation force as objective function, there are also local maximums. In other words, the aim is to verify the unimodality of the objective function.

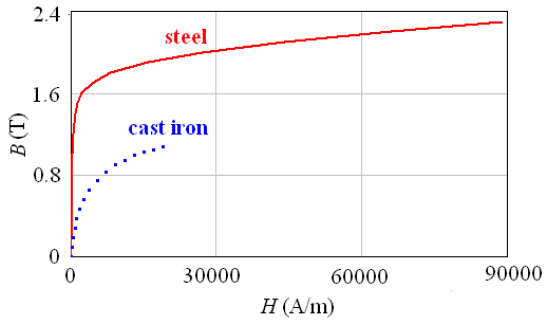

Fig. 2. Magnetization curves for core (plunger with support) (steel) and for carcass (cast iron) [22].

TABLE I.
GEOMETRICAL PARAMETERS OF DC ELECTROMAGNET [22]

r_1 (mm)	29.80	g_b (mm)	19.83	b=0.671a_2 (mm)	10.00
β_1 (°)	45.00	h_b (mm)	138.90	δ_p (mm)	1.00
a_1 (mm)	14.90	s (mm)	2.00	δ_g (mm)	2.00
a_2 (mm)	14.90	v (mm)	24.29	S_b=$g_b h_b$ (mm^2)	2752.27
a_0 (mm)	9.07	h_p (mm)	192.00		

For this was applied an exhaustive optimization method [2] based on the same numerical instruments, taking into account the first two geometric parameters, proven very influential [25], slightly expanding the variation range of the first:

$$k_\beta = \frac{\beta}{\beta_1} \in [0.467 \div 1.533] \quad (5)$$

$$k_b = \frac{h_b}{g_b} \in [6 \div 8] \quad (6)$$

This method has been used successfully to optimize a Superconducting Magnetic Energy Storage (SMES) device [27].

II. EXHAUSTIVE OPTIMISATION METHODS BASED ON RESPONSE SURFACE METHODOLOGY

The exhaustive optimization methods proceed to a complete and systematic analysis of the feasible domain by realization of designs of experiments put side by side or stacked [2]. The applied algorithm uses the RSM and zoom operations.

The response surface methodology (RSM) is a useful technique for modeling and analysis of the response of a system influenced by a set of independent factors. The DOE is essentially based on the creation and exploitation of the models of the response consisting of analytical relationship describing the variations of the response versus to the variation of the factors [1]. Usually, the RSM pro-blems use polynomial models of first- or second-order derived as results of a series of experiments with different values for the factors.

For a set of k factors, the model function (regression) Y_{mod} approximates the value of response Y for any combination of the factors. The second-order models use qua-dratic terms and $p = 6$ coefficients

$$Y_{\text{mod}}(\boldsymbol{x}) = f(\boldsymbol{x}) \cdot \boldsymbol{\beta} \qquad \boldsymbol{x} = (x_1 \ldots x_k)^{\text{T}} \quad (7)$$

$$f(\boldsymbol{x}) = (1\ x\ y\ xy\ x^2\ y^2),\ \boldsymbol{\beta} = (b_0\ b_1\ b_2\ b_{12}\ b_{11}\ b_{22})^{\text{T}} \quad (8)$$

A. Estimation of Coefficients of Polynomial Models

For N experiments and 2 factors, the value of the model function in any experience point $\text{P}_i\ (\boldsymbol{x}_i) = \text{P}_i\ (x_i, y_i)$ is

$$Y_{\text{mod}}(\boldsymbol{x}_i) = f(\boldsymbol{x}_i) \cdot \boldsymbol{\beta}, \quad 1 \le i \le N \quad (9)$$

In most common situations $N > p$ and there is enough information in the experimental data to estimate a unique value for $\boldsymbol{\beta}$ such that the model best fits the response. It commits an adjustment error in each of these points. So there is an error vector $\boldsymbol{\varepsilon}$ (residue) nonzero. The coefficients can be estimated by minimization of the vector $\boldsymbol{\varepsilon}$ by the least squares criterion. The matrix-form relationship linking the response and the model function based on the estimation vector $\hat{\boldsymbol{\beta}}$ is

$$\boldsymbol{Y} = \left(Y(\boldsymbol{x}_1) \ldots Y(\boldsymbol{x}_N)\right)^{\text{T}} = \left(f(\boldsymbol{x}_1) \ldots f(\boldsymbol{x}_N)\right)^{\text{T}} \cdot \hat{\boldsymbol{\beta}} + \boldsymbol{\varepsilon} \quad (10)$$

$$\sum_{i=1}^{N} \varepsilon_i^{\,2} = \sum_{i=1}^{N} \left(Y(\boldsymbol{x}_i) - Y_{\text{mod}}(\boldsymbol{x}_i)\right)^2 \to \min \quad (11)$$

B. Analysis of Variance (ANOVA) of the Model and Adjusting Coefficients

The ANOVA can be used to test the validity of the model function based on the relationship [2]

$$\boldsymbol{Y}^{\text{T}} \cdot \boldsymbol{Y} = \boldsymbol{Y}_{mod}^{\ \text{T}} \cdot \boldsymbol{Y}_{mod} + \boldsymbol{\varepsilon}^{\text{T}} \cdot \boldsymbol{\varepsilon} \quad \Leftrightarrow \quad SST = SSR + SSE \quad (12)$$

The left terms, called the total sum of the squares (SST) is composed of the sum of squares due to regression (SSR) and of the sum of errors squares (SSE). The variances (the mean squares) of the responses, regression and residues are deducted dividing the sums of squares by the corresponding degrees of freedom (DOF). Suppressing the constant terms corresponding to coefficient b_0, the DOFs decrease by 1. Thus

$$MST_{-0} = \frac{SST}{N-1} \quad MSR_{-0} = \frac{SSR}{p-1} \quad MSE = \frac{SSE}{N-p} \quad (13)$$

The Fisher-Snedecor test is performed calculating ratio

$$F_{\text{obs}} = \frac{MSR_{-0}}{MSE} \quad (14)$$

The MSR_{-0} can be considered of the same order as MSE if the ratio F_{obs} is less than a statistical threshold. The null hypothesis H_0 means that $\boldsymbol{\beta} = \boldsymbol{0}$. Under this assumption, F_{obs} is an observed value of a variable F of Fisher-Snedecor type, with p (or $p-1$) and $(N-p)$ DOFs.

The hypothesis H_0 must be rejected at level λ when the probability $P(F \ge F_{\text{obs}}) \le \lambda$.

The quality of a model can be evaluated by some adjustments coefficients:

- Coefficient of determination (R^2) is the ratio of the variance explained by the regression by the variance of responses, both corrected by the average value $\overline{Y}$

$$R^2 = \frac{\boldsymbol{Y}_{mod}^{\ \text{T}} \cdot \boldsymbol{Y}_{mod} - \overline{\boldsymbol{Y}}^{\text{T}} \cdot \overline{\boldsymbol{Y}}}{\boldsymbol{Y}^{\text{T}} \cdot \boldsymbol{Y} - \overline{\boldsymbol{Y}}^{\text{T}} \cdot \overline{\boldsymbol{Y}}} = \frac{SSR_{-\text{m}}}{SST_{-\text{m}}} = \frac{SST_{-\text{m}} - SSE_{-\text{m}}}{SST_{-\text{m}}} \quad (15)$$

- Adjusted coefficient of determination (R_{a}^2) is defined in relation to corresponding DOFs

$$R_{\text{a}}^{\,2} = \left(\frac{SST_{-\text{m}}}{N-1} - \frac{SSE_{-\text{m}}}{N-p}\right) \Big/ \left(\frac{SST_{-\text{m}}}{N-1}\right) \quad (16)$$

- Rate of coefficient of variation by difference between the extreme values of the responses on the current subdomain

$$\Delta = \frac{\hat{\sigma}}{\Delta y} = \frac{\sqrt{SSE}}{\Delta y} \tag{17}$$

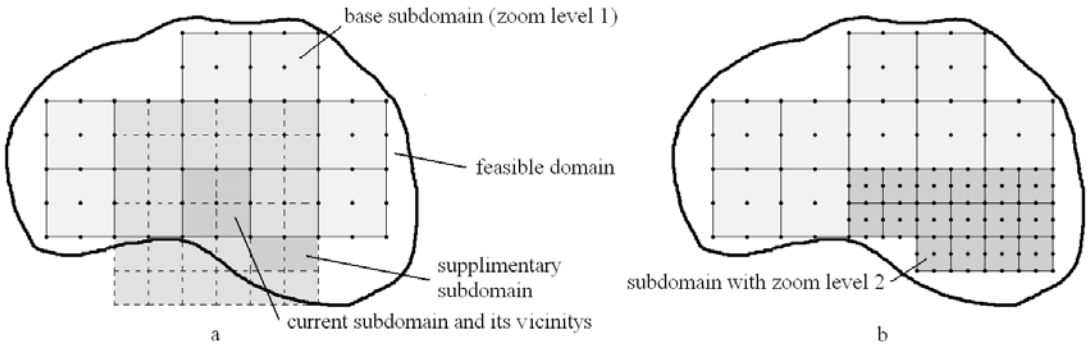

Fig. 3. Description of the exhaustive optimization algorithm [27].

The goal of the exhaustive optimization method is to modeling the objective function by subdomains, performing on each of them a full factorial design with 3 levels per factor, in order to calculate a polynomial model of 2-nd order. If k is the number of factors, result 3^k experiments per subdomain.

The partitioning of study domain is made with an initial hyper-rectangular grid chosen by experimenter, covering the great part of feasible domain, such that exist at least two neighbor subdomains along each of the k dimensions (base subdomains) (Fig. 3a). The candidate points must not be excluded by the constraints on position.

Each analyzed hyper-rectangular subdomain (current subdomain) may be subject to constraints on reached value. Before performing all the 3^k experiments, is made a summary analysis of its 2^k corners: if none of them fulfills the constraints on reached value no longer performs the rest of $3^k - 2^k$ experiments and the next subdomain is analyzed. Otherwise, the rest of experiments are performed.

A calculated model is considered valid if its adjustment coefficients exceed the threshold indicated by experimenter ($R^2 \geq R^2_{\text{lim}}$, $R_a{}^2 \geq R_a{}^2_{\text{lim}}$, $\hat{\sigma}/\Delta y \leq \Delta_{\text{lim}}$, $P \geq P_{\text{lim}}$). Otherwise, the current subdomain must be divided into 2^k subdomains where the same process is repeated.

The algorithm uses a parameter called maximum zoom level that defines the maximum number of scissions of the base subdomain plus 1.

By hypothesis, the base subdomain is realized with a unit level of zoom (Fig. 3a). This parameter allows setting the stop condition of the algorithm. The scission of a base subdomain generates 2^k subdomains with zoom level 2 (Fig. 3b).

The accuracy of the modeling can be set by the parameter called minimum zoom level that defines the minimum number of scissions to apply to the base subdomain.

For the boundary subdomains, a supplementary analysis of theirs vicinities can be useful for better covering of the feasible domain. So, if a boundary subdomain must be divided into 2^k parts, then the analysis is extended to the neighbour subdomains in order to find some parts of them (supplementary subdomains) which can complete the initial grid (Fig. 3a).

The algorithm is recursive. It calls itself either whether the minimum number of zooms is not reached or whether the maximum number of zooms is not reached, or whether none of the criteria of quality is fulfilled.

III. Optimization Problem and Its Solving

The optimization problem is the maximization of the electromagnetic force at δ = 41 mm, calling actuating force (F_a), which is set as objective function. This is a 2-D nonlinear optimization problem subject to four equality constraints consisting in preserving the global dimensions of the device (the external radius $r_{\max}$, the height of carcass $h_{\max}$, the height of plunger with support $H_{\max}$) and the coil cross section ($S_b = g_b \cdot h_b$). The complete form (P) of the optimization problem is

$$\text{P}: \begin{cases} \min F_a(k_\beta, k_b, a_0, a_2, h_p, g_b) \\ k_{\beta\min} \leq k_\beta \leq k_{\beta\max} \\ k_{b\min} \leq k_b \leq k_{b\max} \\ g_r(k_b, k_{a1}, k_v) = 0 \\ g_h(k_b, k_{a1}, k_v) = 0 \\ g_H(k_b, k_{a1}, k_v) = 0 \\ g_{Sb}(k_b, k_{a1}, k_v) = 0 \end{cases} \tag{18}$$

$$g_r(k_b) = r_1 + \delta_p + \delta_g + 2s + g_b(k_b) + a_0(k_b) - r_{\max} \tag{19}$$

$$g_h(k_b, k_{a1}) = k_{a1}a + a_2(k_b, k_{a1}) + 2s + k_b \cdot g_b(k_b) - h_{\max} \tag{20}$$

$$g_H(k_b, k_{a1}, k_v) = h_p(k_b, k_{a1}, k_v) + k_v \cdot k_b \cdot g_b(k_b) + k_{a1} \cdot a - H_{\max} \tag{21}$$

$$g_{Sb}(k_b) = k_b \cdot [g_b(k_b)]^2 - S_b \tag{22}$$

where a = 14.90 mm, $r_{\max}$ = 65.70 mm, $h_{\max}$ = 172.60 mm, $H_{\max}$ = 231.19 mm, S_b = 2752.27 mm^2 are initial values resting constant.

The 2-D feasible domain is represented in Fig. 4, being a rectangular domain, in which there are only positional constraints, related to the parameters' limits.

For the zoom level ζ = 1, the feasible domain was partitioned into a number of 4 × 4 = 16 basic subdomains on which the ANOVA technique was applied, obtaining different response surfaces, whose quality was tested by

calculating the four adjustment coefficients of P, R^2, $R_a{}^2$, Δ.

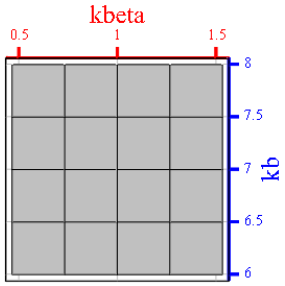

Fig. 4. The 2-D feasible domain and basic subdomains ($\zeta = 1$).

Theirs chosen thresholds are established to be: $P_{lim} = 0.99$, $R^2_{lim} = 0.98$, $R_a{}^2_{lim} = 0.95$, $\Delta_{lim} = 0.08$. The maximum zoom level was chosen to be $\zeta_{lim} = 3$.

The differences between the values of the adjustment coefficients are represented chromatically in Fig 5, noting isolated areas with nuances much different from the majority, indicating the uncertainty subdomains of the local or global maxima. Subdomains of unsatisfactory quality (column no. 4) still require partitioning.

For the zoom level $\zeta = 1$ the optimal value is obtained in the point P_1 having the coordinates $k_\beta = 1.4000$ and $k_b = 6.5000$, with value $F_{a1} = 808.767$ N, meaning a gain of 23.19%, comparatively with initial value $F_a = 656.522$ N. The point P_1 is visible in Fig. 9. In the subdomains in which the quality criteria are fulfilled was not performed the full factorial design and these appear not divided.

In Fig. 6 are represented the results obtained for $\zeta = 2$, with optimal solution in the point $P_2(1.4667, 6.6250)$, $F_{a2} = 811.053$N, gain 23.54% and in Fig. 7, the results for $\zeta = 3$, with optimal solution in $P_3(1.4333, 6.5625)$, $F_{a3} = 813.583$N, gain 23.92%.

These values are comparable with the previous ones.

Fig. 8 collects the results shown in Figs. 5-7, highlighting a single "island" of color much different from the rest, which indicates the presence of a single maximum, which proves the unimodality of the objective function up to this zoom level. The points P_2 and P_3 are visible in Fig. 10 and Fig. 11.

Two stopping criterions limit the number of iterations, when the accuracy is acceptable. Thus, the value computed is compared with initial one:

$$\varepsilon_1\,[\%] = \frac{F_a{}^{(t)} - F_{a\_in}}{F_{a\_in}} \cdot 100 \le \varepsilon_{1max}\,[\%] \qquad (23)$$

or the value computed per iteration (t) is compared with the previous different one (s) ($1 \le s \le t-1$):

$$\varepsilon_2\,[\%] = \frac{F_a{}^{(t)} - F_a{}^{(s)}}{F_a{}^{(s)}} \cdot 100 \le \varepsilon_{2max}\,[\%] \qquad (24)$$

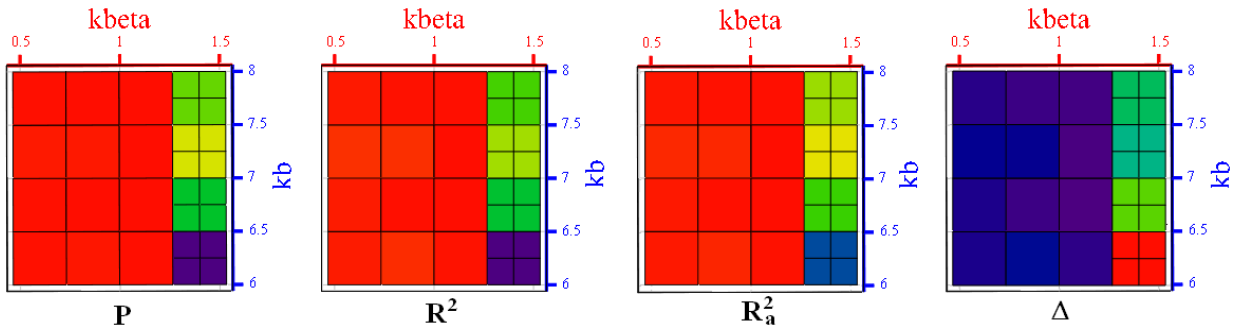

Fig. 5. The chromatic highlighting of the differences between the values of the adjustment coefficients on the basic subdomains ($\zeta = 1$).

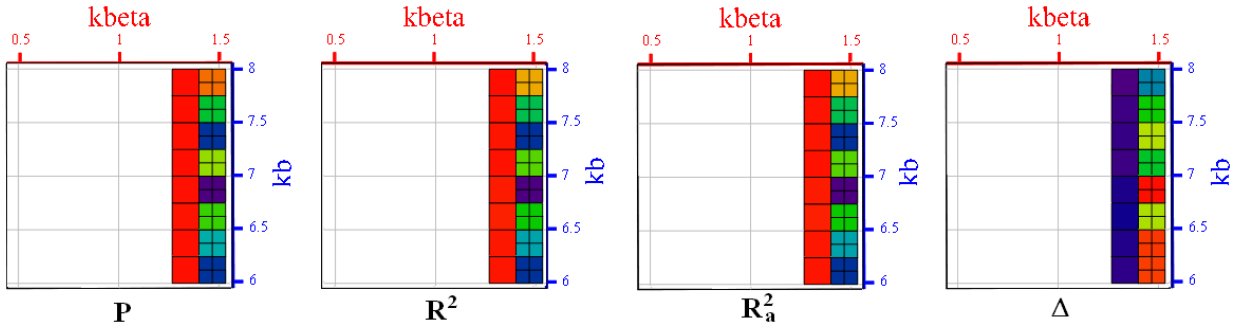

Fig. 6. The chromatic highlighting of the differences between the values of the adjustment coefficients on the subdomains with $\zeta = 2$.

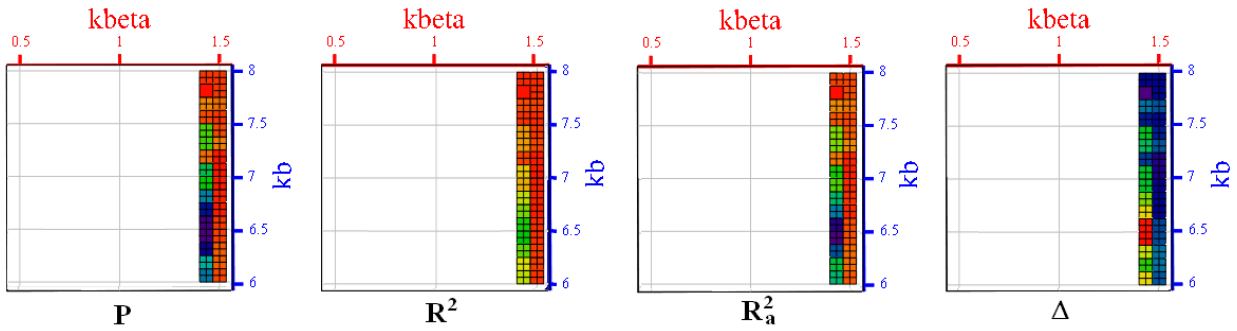

Fig. 7. The chromatic highlighting of the differences between the values of the adjustment coefficients on the subdomains with ζ = 3.

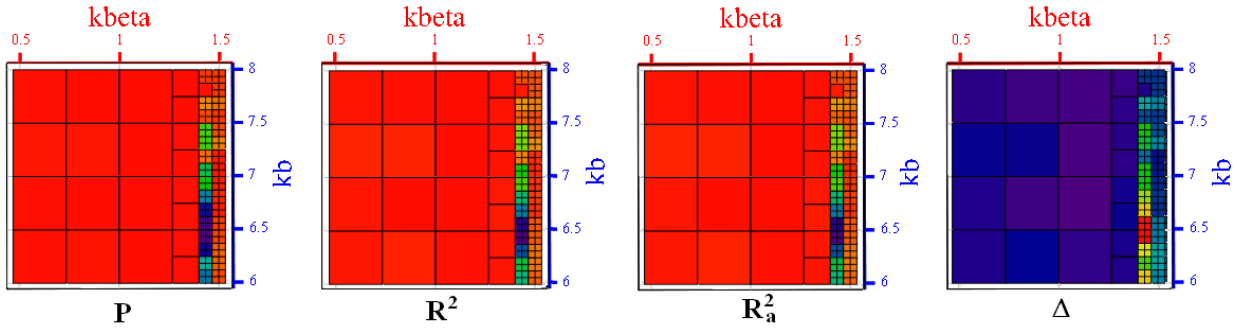

Fig. 8. The chromatic highlighting of the differences between the values of the adjustment coefficients on the analysed subdomains (ζ = 1, 2, 3).

The applied exhaustive optimization method requires a total of N = 577 numerical 2-D FEM experiments. More than half (324 experiments) can be recovered from previous iterations, resulting in a real number of 253 experiments.

In Table II are summarized the results of application of the optimization algorithm to the electromagnetic device along the three iterations, showing the variation of the design parameters, objective function, errors and main geometrical parameters.

Figure 12 presents on left and right sides the initial and the optimal geometrical shapes with the distributions of magnetic flux density obtained in FEMM software as axisymmetric solution.

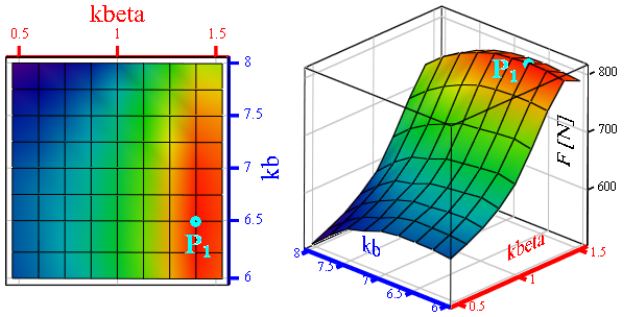

Fig. 9. The values of the objective function in the nodes of the partitioned basic subdomains and the optimal value for ζ = 1 (Point P_1).

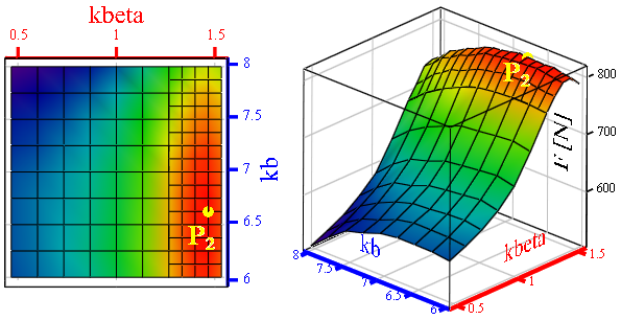

Fig. 10. The values of the objective function in the nodes of the partitioned basic subdomains and the optimal value for ζ = 2 (Point P_2).

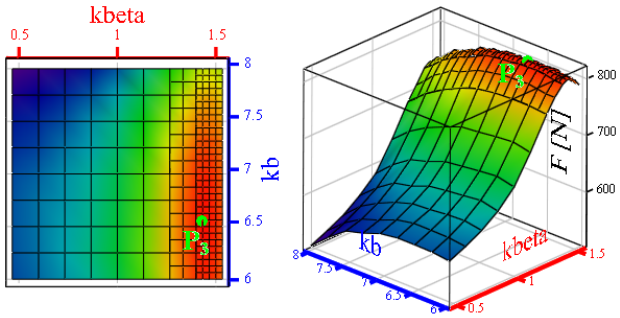

Fig. 11. The values of the objective function in the nodes of the partitioned basic subdomains and the optimal value for ζ = 3 (Point P_3).

TABLE II. QUANTITIES VARIATION DURING THE OPTIMIZATION PROCESS: DESIGN PARAMETERS, OBJECTIVE FUNCTION F_a, ERRORS AND MAIN GEOMETRICAL PARAMETERS

Iterations	N_{tot}	N_{rec}	k_β	k_b	F_a (N)	ε_1 (%)	ε_2 (%)	β (°)	g_b (mm)	h_b (mm)	a_0 (mm)	a_2 (mm)	v (mm)	h_p (mm)
Initial	1	-	1.0000	7.0000	656.522	-	-	45.00	19.83	138.80	9.07	14.90	24.29	192.00
1	144	64	1.4000	6.5000	808.767	23.19	23.19	63.00	20.58	133.75	8.32	19.95	23.41	192.89
2	144	86	1.4667	6.6250	811.053	23.54	0.28	66.00	20.38	135.03	8.52	18.67	23.63	192.66
3	288	174	1.4333	6.5625	813.583	23.92	0.31	64.50	20.48	134.39	8.42	19.31	23.52	192.77
Total	577	324												

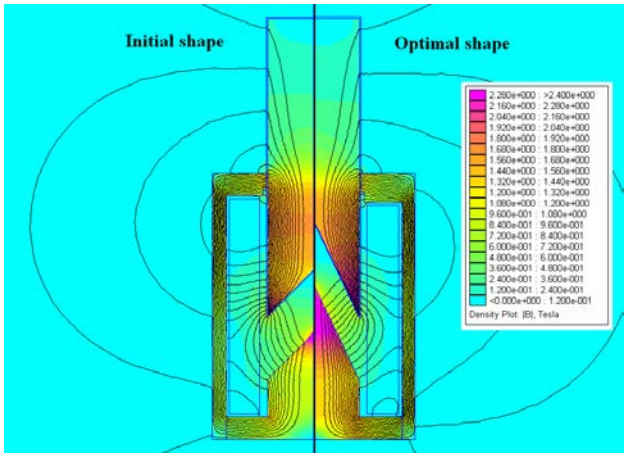

Fig. 12. Distribution of magnetic flux density for initial (left) and optimal (right) shapes (δ = 41 mm, FEMM, axisymmetric solution).

IV CONCLUSIONS

The paper presents the application of an exhaustive optimization method based on DOE and 2-D FEM, on a DC electromagnetic device. This was the subject of several previous works that investigated the improvement of its performances through methods of the same type, but capable of determining only a local optimum.

The optimization problem is nonlinear and it consists in maximization of the actuating force taking into account two geometric parameters (the angle ratio of the support tip and the coil shape ratio) subject to equality constraints which describe the preservation of the global dimensions of the device and of the cross-section of the winding.

The exhaustive optimization algorithm used the values of numerical simulation with FEMM software and it allowed the determination of the global optimum which corresponds to a gain in actuation force of 23.92%, from 656.522 N to 813.583N.

The result obtained in this paper is comparable to the previous ones, validating the old methods with a significant cost in the workload.

ACKNOWLEDGMENT

Source of research funding in this article: Research program of the Electrical Engineering Department financed by the University of Craiova.

Contribution of authors:

First author – 100%

Received on July 17, 2022

Editorial Approval on November 20, 2022

REFERENCES

[1] D. Montgomery, Design and analysis of experiment, 5-th Edition, Arizona State University, 2000.

[2] S. Vivier, "Strategies d'optimisation par la methode des plans d'experiences et applications aux dispositives electrotechniques modelise par elements finis," Ph-D Thesis, Lille, 2002.

[3] S.-B. Yoon, J. Hur, Y.-D. Chun, and D.-S. Hyun, "Shape optimization of solenoid actuator using the finite element method and numerical optimization technique," IEEE Transactions on Magnetics, Vol.33, No. 5, pp. 4140-4142, September, 1997.

[4] J.-S. Ryu, Y. Yao, C.-S. Koh,S. Yun, and D.-S. Kim, "Optimal Shape Design of 3-D Nonlinear Electromagnetic Devices Using Parameterized Design Sensitivity Analysis," IEEE Transactions on Magnetics, Vol. 41, No. 5, pp.1792-1795, May, 2005.

[5] S.-I. Park, and S. Min, "Magnetic Actuator Design for Maximizing Force Using Level Set Based Topology Optimization," IEEE Transactions on Magnetics, Vol. 45, No. 5, pp.2336-2339, May, 2009.

[6] J. Lee, E.-M. Dede, and T. Nomura, "Simultaneous Design Optimization of Permanent Magnet, Coils, and Ferromagnetic Material in Actuators," IEEE Transactions on Magnetics, Vol. 47, No. 12, pp. 4712-4716, May, 2011.

[7] I. Yatchev, M. Rudnicki, K. Hinov, and V. Gueorgiev, "Optimization of a permanent magnet needle actuator," COMPEL, Vol. 31, Issue 3, pp. 1018-1028, 2012.

[8] R. Narayanswamy, D.-P. Mahajan, and S. Bavisetti, "Unified Coil Solenoid Actuator for Aerospace Application," Proceedings of IEEE Electrical Systems for Aircraft, Railway and Ship Propulsion, Bologna, October 16-18, pp. 1-5, 2012.

[9] S. Yong, J. Tong, S. Enze, and Y. Zaiming, "Analysis and optimization of static characteristics in overall operating conditions of electromagnetic actuator," Research Journal of Applied Sciences, Engineering and Technology 7(8), pp. 1561-1567, 2014.

[10] F. Mach, I. Novy, P. Karban, and I. Dolezel, "Shape Optimization of Electromagnetic Actuators," Proceedings of IEEE ELEKTRO, Bologna, May 19-20, pp. 595-598, 2014.

[11] H.-M. Ahn, T.-K. Chung, Y.-H. Oh, K.-D. Song, Y.-I. Kim, H.-R. Kho, M.-S. Choi, and S.-C. Hahn, "Optimal Design of Permanent Magnetic Actuator for Permanent Magnet Reduction and Dynamic Characteristic Improvement using Response Surface Methodology," J. Electr. Eng. Technol.2015, 10(3): pp. 935-943, 2015.

[12] E. Plavec, and M. Vidović, "Genetic Algorithm Based Plunger Shape Optimization of DC Solenoid Electromagnetic Actuator," Proceedings of 24th IEEE Telecommunications Forum (TELFOR), Belgrade, pp. 1-4, 2016.

[13] S.-W. Lee, J. Lee, and S. Cho, "Isogeometric Shape Optimization of Ferromagnetic Materials in Magnetic Actuators," IEEE Transactions on Magnetics, Vol. 52, No. 2, pp. 1-8, February, 2016.

[14] S. Jeong, S. Lim, and S. Min, "Level-Set-Based Topology Optimization Using Remeshing Techniques for Magnetic Actuator Design," IEEE Transactions on Magnetics, Vol. 52, No. 3, pp. 1-4, March, 2016.

[15] S. Lim, S. Jeong, and S. Min, "Multi-Component Layout Optimization Method for the Design of a Permanent Magnet Actuator," IEEE Transactions on Magnetics, Vol. 52, No. 3, pp. 1-4, March, 2016.

[16] F. Gillon, and P. Brochet, "Screening and response surface method applied to the numerical optimization of electromagnetic devices," IEEE Transaction on Magnetics, Vol. 36, No. 4, pp.1163-1166, 2000.

[17] D.-K. Hong, K.-C. Lee, B.-C. Woo, and D.-H. Koo, "Optimum design of electromagnet in magnetic levitation system for contactless delivery application using response surface methodology," Proceedings of the 2008 International Conference on Electrical Machines, pp. 1-6, 2008.

[18] J.-M. Biedinger, and D. Lemoine, "Shape sensitivity analysis of magnetic forces", IEEE Trans.on Magn.,Vol.30, pp. 2309-2516, 1997.

[19] G. Sefkat, "The design optimization of the electromechanical actuator," Structural and Multidisciplinary Optimization, February 2009, Volume 37, Issue 6, pp. 635–644, 2009.

[20] T.-W. Kim, and J.-H. Chang, "Optimal design of electromagnetic actuator with divided coil excitation to increase clamping force," Journal of International Conference on Electrical Machines and Systems, pp. 1461-1464, 2014.

[21] K. Li, X. Zhang, and H. Chen, "Design Optimization of a Tubular Permanent Magnet Machine for Cryocoolers", IEEE Transactions on Magnetics, Vol. 51, pp.1-8, 2015.

[22] A.-I. Dolan, "Optimization of DC electromagnet using design of experiments and FEM," XIII-th IEEE International Conference on Applied and Theoretical Electricity – ICATE 2016, Craiova, Romania, October 06-08, pp. 1-6, 2016.

[23] A.-I. Dolan, "Three parameters optimization of acting force of DC electromagnet," Proceedings of 11-th IEEE International Conference on Electromechanical and Power Systems – SIELMEN 2017, Iasi-Chisinau, October 11-13, pp. 1-4, 2017.

[24] G. Hortopan, Electrical apparatus of low voltage (in Romanian), Tehnica Publishing House, Bucharest, 1969.

[25] A.-I. Dolan, "Optimal Shape of DC Electromagnet," Annals of the University of Craiova, Series: Electrical Engineering, Universitaria Publishing House, No. 41, pp. 9-13, 2017.

[26] A.-I. Dolan, "Improvement of Acting Force of DC Plunger-Type Electromagnet by Six Parameters optimization," Proceedings of the XII-th International Conference on Electromechanical and Power Systems – SIELMEN 2019, October 9-11, pp. 1-5, Iasi-Chisinau, 2019.

[27] A.-I. Dolan, and F. Stefanescu, "Exhaustive optimization method based on DOE and FEM applied on a SMES device," Proceedings of the XIX-th IEEE International Symposium on Electrical Apparatus and Technologies – SIELA 2016, Bourgas, Bulgaria, May 29-June 1, pp. 92-95, 2016.

DOI: 10.52846/AUCEE.2022.07

Automatic Sorting System for Educational Training

Laurentiu Alboteanu, Florin Ravigan
University of Craiova / Department of Electromechanical, Environmental and Applied Informatics,
Craiova, Romania, e-mail: lalboteanu@em.ucv.ro, ravigan.florin@gmail.com

***Abstract* - At the same time as the introduction of automated equipment in industry, production operators and maintenance workers servicing automated stations require professional training courses depending on the category and job. Depending on the particularity of the production process, these training courses can be done internally at the production unit, at external industrial partners or at universities. The paper presents an automatic tire sorting system made on a small scale. The sorting system is composed of an input stock and two output stocks of sorted tires. Tire storage in the two output stocks is done with an electro-pneumatic manipulator robot. The sorting is done according to the tire bead width, for which the system is equipped with the appropriate sensors. The structure is controlled by an Arduino Mega2560 microcontroller development system. The sorting station can also be controlled manually by the operator via a joystick and some buttons. In comparison to other sorting systems, the robot structure is simpler. It performs the transfer of the tires by only two movements, thus reducing the handling time. Also, the automatic sorting system realized corresponds to the requirements imposed on flexible production systems. The automatic system can be used both for training students from technical faculties and industrial operators in the field.**

Cuvinte cheie: *sortare, sistem automat, actionare pneumatică, microcontroler senzori, robot manipulator, pregătire educațională.*

Keywords: *sorting, automatic system, pneumatic drive, microcontroller, sensors, manipulating robot, educational training*

I. INTRODUCTION

Industry in general and in the machine construction, in particular, requires great flexibility of the manufacturing process, flexibility enabling the transition easy from the technical and cheap in terms of equipment and labor to another manufacturing. In this context, it is necessary to design and implement special equipment that will be comprised of flexible automations. An important role in this equipment you have manipulators and robots, which ensure the construction features and functional characteristics and quality indicators for flexible manufacturing [1].

Robots and manipulators are the most complex and flexible machines that have been created and used by man so far that incorporate pneumatic drives. Taking into account these considerations the paper presents an automatic sorting system using a manipulator robot and a pneumatic actuation system. Industry needs knowledgeable, skilled robotics engineers, technicians, and operators. The application enables trainers to successfully integrate robotics into programs and lab facilities [1], [2].

The automatic sorting system presented in the work represents a small scale model of an automatic tire sorting system. It can be used for the educational training of students, but also of staff in the field.

II. DESCRPTION OF SORTING STATION

A. Structure of a sorting station

The various products resulting from the manufacturing process require sorting and palletizing operations. The sorting facility is composed of an electric drive system (SAE) and an electro pneumatic one (SAEP), under the coordination of a control system (CS) which, based on the operating protocol, ensures the control laws (Fig.1) [3], [4]. The control system receives the information from the sensory system (SS) regarding the state of the system and provides the commands to the actuators in the drive structure to realize the functional diagram.

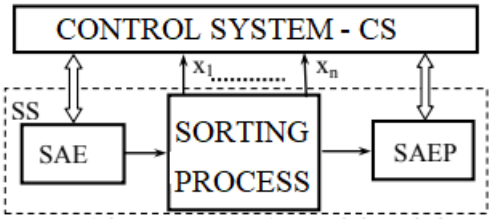

Fig. 1. Structure of sorting station.

The tire sorting station is based on a manipulator robot that sorts tires according to the program selected by the user.

The tires are brought by conveyor belts to the point of collection where they are caught with the help of a gripper, here the selection process also takes place (depending on the bar code placed on each bead, depending on the width of inches) and the tire is placed on another conveyor that transports it to the storage points [5].

Robots used in sorting operations must be equipped with guiding devices with 5-6 degrees of mobility, universal or flexible gripping devices (pincers). Most of the time, such robots are equipped with autonomous travel systems, and sometimes with remote control systems. The drive system of robots of this type can be electric, hydraulic or combined.

The control system must contain surface and/or volume evaluation programs. He must ensure the command of the peripheral devices, process the information collected by the sensors about the nature of the manipulated objects and their arrangement, and modify the behavior of the robot according to this information.

B. *Design of sorting system for educational training*

The educational application refers to a system for handling and sorting pieces according to their width.

Figure 2 shows the layout of the component blocks on the training board.

The manipulator has two axes, the first actuated by an electric motor and the second by a pneumatic cylinder.

The position information is taken from the sensors of each axis.

To carry out the sorting operation, the analysis of two signals generated by a distance sensor located at the end of the gripper will be considered.

At the base of the control process is the command and control unit, which manages the entire process, as well as the man-machine interface [6], [7], [8].

Based on the operating principle of a closed-loop control system, the command and control block takes the information about the positions of the system elements from the position sensors, and the information about the width of the piece gripped in the gripper from the distance sensor.

Following the processing of this information, according to a pre-established program, command signals are generated to the pneumatic actuators [9], [10] (Fig. 2).

Sorting process parameters can be viewed and modified through the user interface.

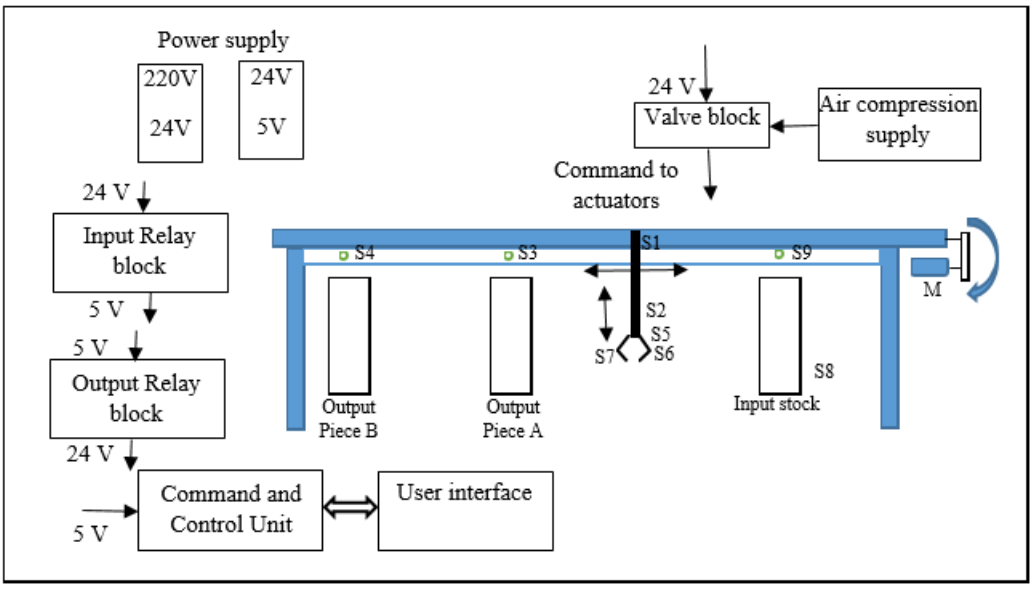

Fig. 2. Training board of sorting system - the layout of the components.

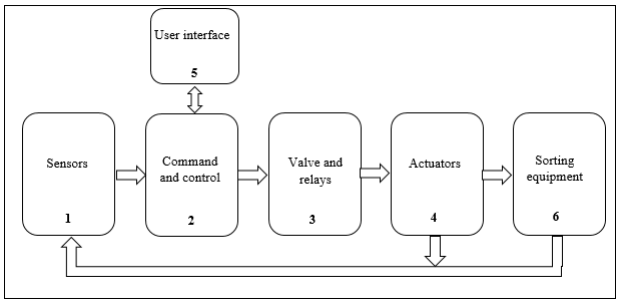

Fig. 3. Block diagram of a sorting system.

The block diagram of the system (Fig. 3) contains 6 blocks:

- Block number 1: it is made up of the 9 sensors of the sorting robot:

Sensor 1 - arm up position;

Sensor 2 - lower arm position;

Sensor 3 - center robot position (piece A);

Sensor 4 - left robot position (piece B);

Sensor 5 – detection of type A piece;

Sensor 6 - detection of type B piece;

Sensor 7 - gripper status;

Sensor 8 - piece presence sensor;

Sensor 9 - right robot position (initial position).

- Block number 2 – the command and control block, is the part of the application that deals with the management of input and output signals and decides the operation of the application after an established automatic cycle or the execution of commands manually. It operates in two modes: in closed-loop (control) and also with a human operator in the loop.
- Block number 3 represents the part of pneumatic solenoid valves [11] and the four motor control relays:

Relays RQ3, RQ4- left motor rotation;

Relays RQ5, RQ6- right motor rotation.

Individual solenoid valves are used for each movement of the manipulator:

Solenoid valve 1 – Up arm control;

Solenoid valve 2 - Down arm control;

Solenoid valve 3 - Gripper control.

Solenoid valves receive the command signal from the microcontroller and distribute the air pressure to each pneumatic actuator.

Block number 4 contains pneumatic and electric actuators:

Cylinder 1- Actuates the arm on the vertical axis;

Cylinder 2 - Closes/opens the gripper;

The motor – Moves the manipulator horizontally.

Block number 5 represents the user interface. It is composed of:

- an LCD that displays the current status of the system and the status of commands in manual mode;

- a joystick with 5 positions used for the manual controls of the robot;

- a safety power supply button, which interrupts the supply;

- a button with 3 positions used to activate the states: Automatic/Off/Manual of the system.

All 5 blocks work according to a set schedule.

The electronic handling system consists of three main subsystems:

The subsystem for determining the position, present in the form of a group of sensors related to each axis. For the y-axis, the sensors are mounted along the electric axis used to actuate the manipulator horizontally, for the z-axis, the sensors are mounted at the stroke ends of the cylinder.

The adaptation subsystem. The position signals generated by the sensors are 24V signals which are converted to 5V signals by a block of 9 relays.

The movement of the mobile elements of the system is carried out with of an electromechanical linear actuator and a pneumatic actuator, the tool is a pneumatic gripper.

Solenoid valve control subsystem

The adaptation between the signals generated by the command and control block, the 5V signal generated by the output pins of the microcontroller and the supply voltages of the cylinder control solenoid valves is carried out by means of a block of relays which, when activated, generate a 24V signal**.**

The command and control block receives the signal from the position sensors and from the differentiation sensor and presents the part by means of an input signal receiving module, consisting of a block of nine relays that, when activated, generate a signal of 5V.

The processing unit takes the results from the input port, equivalent to the values of the positions and the tire type, which it processes based on a program written in a memory block.

After processing, through the control signal generation module, the activation signals of the electro valve coils that control the pneumatic actuators and the electromechanical actuator are provided at the output [12].

The user interface system has a 20x4 character LCD display necessary for displaying internal and external parameters and for accessing the menu.

The data entry system consists of a 5-position joystick used for manual robot controls and a three-position button used to select the three system states: Manual, Off, Automatic.

In order to reduce the number of components as well as to benefit from the flexibility of programmable systems [13], the system is designed around an Arduino Mega 2560 microcontroller produced by the Arduino Company [14], which coordinates its entire operation.

The block diagram of the system based on a microcontroller is presented in figure 4.

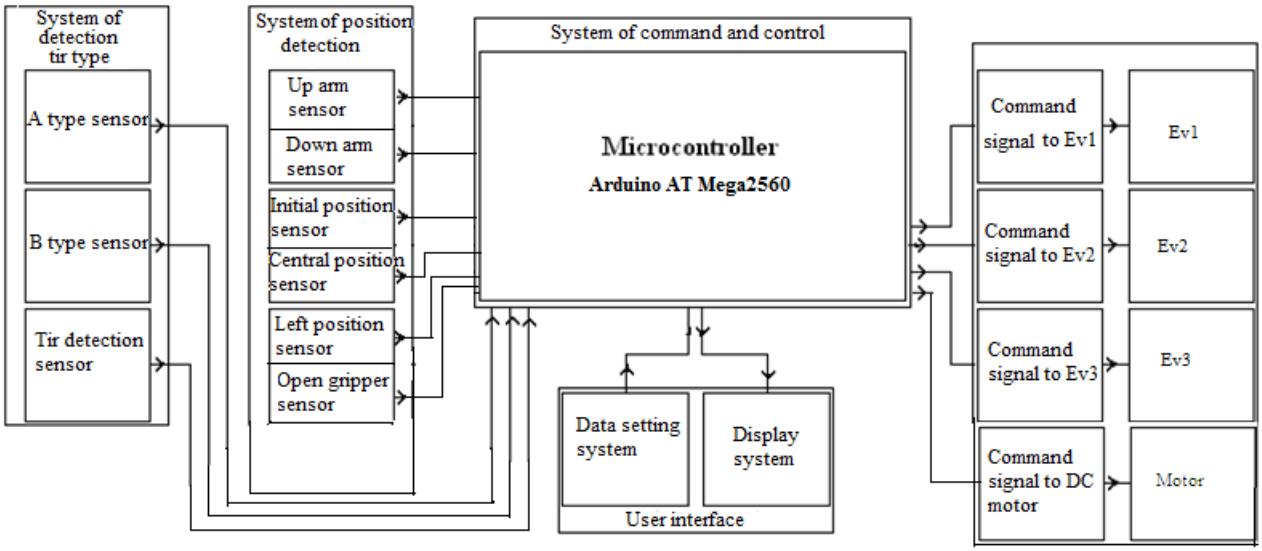

Fig. 4. Detailed block diagram of a educational sorting system.

The following functions will be implemented on the designed system:

- carrying out the cycle entered in the program automatically;

- interruption of the automatic cycle, with the possibility of its continuation;

- movement of robot by manual controls;

- displaying the position of the moving elements;

- determination of the width of the part gripped by the gripper;

- storage of objects in different areas (one for each implemented width);

- training the system regarding the association between the width of the piece and the area where it will be positioned;

III. Implementation Of Automatic Sorting System

A. Implementation of hardware part

One method of verifying the proposed solution is to achieve an experimental model. Based on the structure presented above, an experimental model of the automatic handling and sorting system was developed. System components are represented in figure 5.

The components shown in the figure have the following meanings:

1- DC voltage sources; 2- group of compressed air preparation elements; 3- pieces input stock; 4- sorted pieces of type A; 5- sorted pieces of type B; 6- development system with microcontroller; 7- relay module; 8- handling robot; 9- DC motor for the translation of the robot; 10- sensor of position; 11 - sensor of detecting the presence piece; 12- operator console.

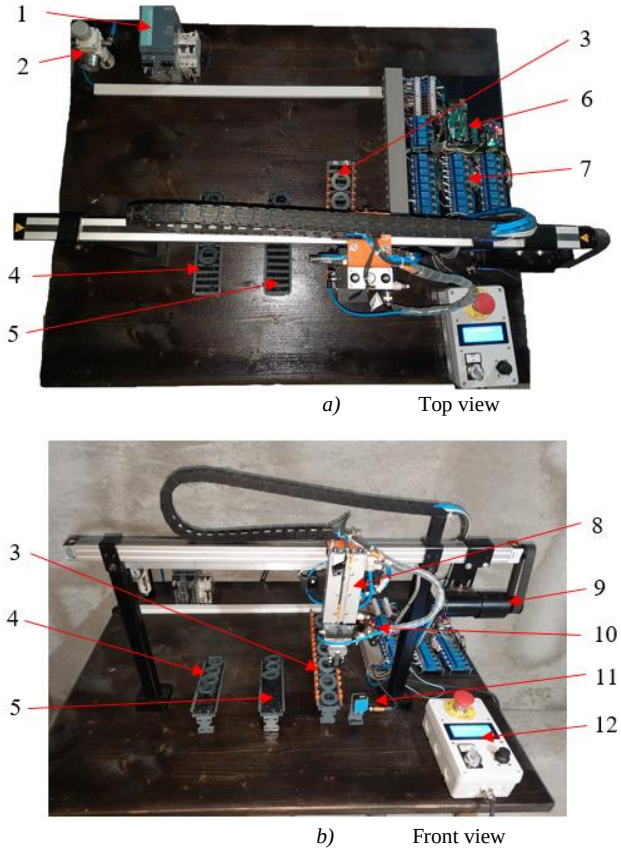

a) Top view

b) Front view

Fig. 5. Experimental model of the automatic sorting system

Within the designed system, the drive is performed by three actuators:

- a C3 linear electromechanical actuator for the translation of the arm;

- a C1 double-acting linear pneumatic actuator for actuating the up-down arm;

- a C2 single-effect pneumatic actuator to actuate the gripper.

The air preparation group is FR type produced by SMC [15] with the coding: AW20-F02-C-X64. This combination minimizes space and pipelines by integrating the two units into one.

Standard features include a regulator that can be quickly locked by pushing the adjustment knob down.

A pressure gauge is mounted on the control group. The filter cartridge provides a filtration rate of up to 5 microns/m.

For the distribution of compressed air to actuators, two types of solenoid valves were used:

• To actuate of the cylinders for robot, lifting and ro arm it used three bistable solenoid valve Festo [16] type: CPE14-M1BH-5J-Q-8;

• For the control of the cylinder that closes / opens the gripper, a Festo type XCPE14-M1BH-3GLS-1/8 monostable solenoid valve is used.

The actuators used to operate the robot and the collecting table is manufactured by Festo [16].

The feed rate is achieved by the pneumatic energy transmitted by the actuating valve; the return is done by eliminating pressure from the circuit and with the help of the spring return.

Waircon URG 5/8 type regulators have been used to control actuator speed. The "URG" series flow regulators are produced in in-line, unidirectional versions.

The "URG" model has a built-in control valve to control the flow in one direction, while the reverse flow is free. They are high precision regulators and can provide a high flow rate ratio and are very compact.

B. Implementation of the command and control system

In the implementation of the command and control system, the following aspects were taken into account:

- simplifying the hardware part and using as few components as possible;
- the possibility of easy system programming;
- providing internal and external parameters to the user interface.

To meet the above-mentioned requirements, a microcontroller development system was developed (Fig. 6).

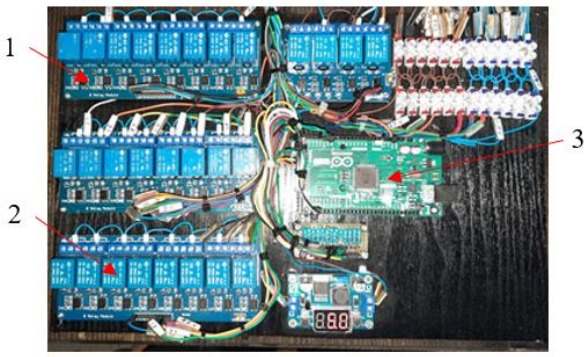

Fig. 6. Command and control system: 1- output relay module; 2- input relay module; 3- microcontroller development system.

For this purpose, the Arduino Mega 2560 microcontroller has been chosen [14].

The Mega 2560 is a development system built around the Atmega2560 microcontroller, which is equipped with numerous communication pins, analogs and PWM, useful for connecting with various elements: monitoring, control, control, etc. (sensors, relays).

It offers a number of facilities including:

- requires a small number of external components;

- has analogue inputs needed to connect the sensors;
- allows direct connection of an LCD display.
- can perform arithmetic and logical operations required in the sorting pieces process.

Arduino Mega 2560 is a ATmega2560 based microcontroller board. It has 54 digital inputs / outputs (of which 14 can be used as PWM outputs), 16 analog inputs, 4 UARTs (hardware serial ports), 16MHz oscillator crystal, a USB connection, a power jack, a ICSP header and a reset button. It contains everything it takes to operate the microcontroller. Simply connects to a computer with a USB cable or AC / DC adapter or battery.

The ATmega2560 has 256 KB flash memory for storing the code (of which 8 KB is used for Bootloader), 8 KB of SRAM and 4 KB of EEPROM (readable and written with the EEPROM Library). Arduino boards have a 1024 byte EEPROM space.

The Arduino Mega2560 has a host of facilities for communicating with a computer, with another Arduino or other microcontrollers. The ATmega2560 offers four hardware UARTs for TTL 5V serial communication.

A Software Serial library allows serial communication on any of the Mega2560's digital systems.

The ATmega2560 also supports I2C (TWI) and SPI communication. The Arduino software includes a Wire library to simplify the use of the I2C bus.

To obtain the 5V input signal in the microcontroller, the 24V sensor signal is passed through a relay block powered at 5V, and which is activated by the sensor signal sends a 5V signal to the input port of the microcontroller.

The sensors system of sorting station enables the acquisition of two distinct types of information:

- information on the internal parameters of the system (the position of each element);

- information about external parameters, in particular the dimension of objects grabbed by the gripper, which is the sorting criterion.

Two MK5100 IFM sensors were used to determine the two positions of the robot arm.

Closed open positions of the gripper are given by a pressure switch type: Festo SDE5-D10-O-Q6-P-M8 inserted into the pneumatic actuator of the gripper.

WF50-60B416 type sensor was used to detect the presence of the piece, and a contrast sensor produced by SICK K3L-P3216 was used to identify the color.

C. Implementation of Software Part

Arduino Mega can be programmed with Arduino ATmega2560 software. Arduino Mega has a preinstalled bootloader that allows you to load a new code without using an external programmer. It has an automatic reset button. It also performs overcurrent protection of the USB. Arduino Mega 2560 has a self-resetting fuse mounted to protect of the computer USB from short-circuit and overcurrent.

The Arduino program can be divided into three main parts: structure, values (variables and constants) and functions [17], [18].

The general structure of software for microcontroller is shown in figure 7.

The program starts with microcontroller initialization and variables used [6]. Implementation of various timings is possible by using a sequence of decrement of all counters used. Then follows acquisition of analog-digital signals, execution of algorithm, then transmitting the synthesized commands.

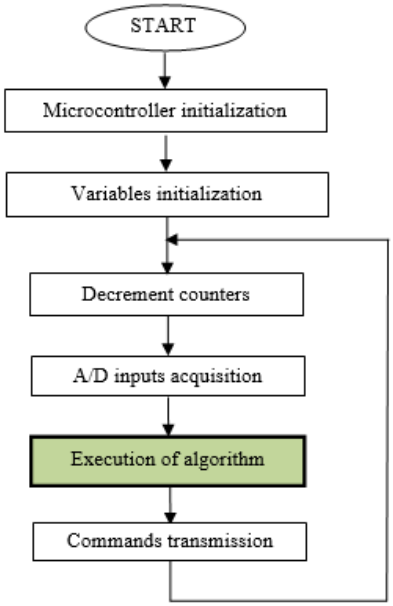

Fig. 7. Flow diagram of microcontroller program.

The main program algorithm for the automatic sorting station cycle is shown in figure 8.

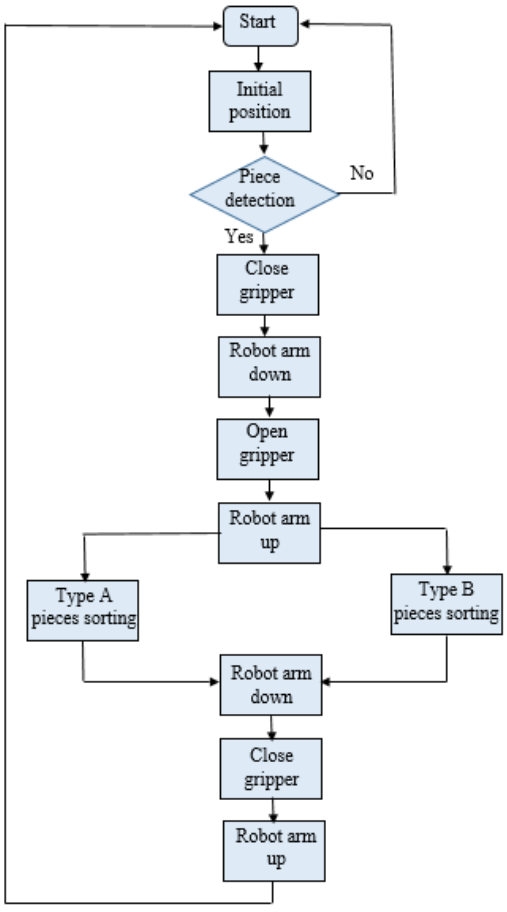

Fig. 8. Flow diagram of proper algorithm – automatic operation mode.

During the automatic sequence, the user cannot execute manual commands.

IV. Testing of Automatic Sorting System

Testing actually consists of correct working verification according to the protocol and conditions imposed by design.

In figure 9 there are captured the operating states in a work cycle of handling-sorting station. These states were predefined in the design stage of automatic handling-sorting system (Fig. 8) for the purpose of verification and easier debugging.

The 6 states of operation are highlighted in the figure by the positions occupied by the manipulating robot (RM).

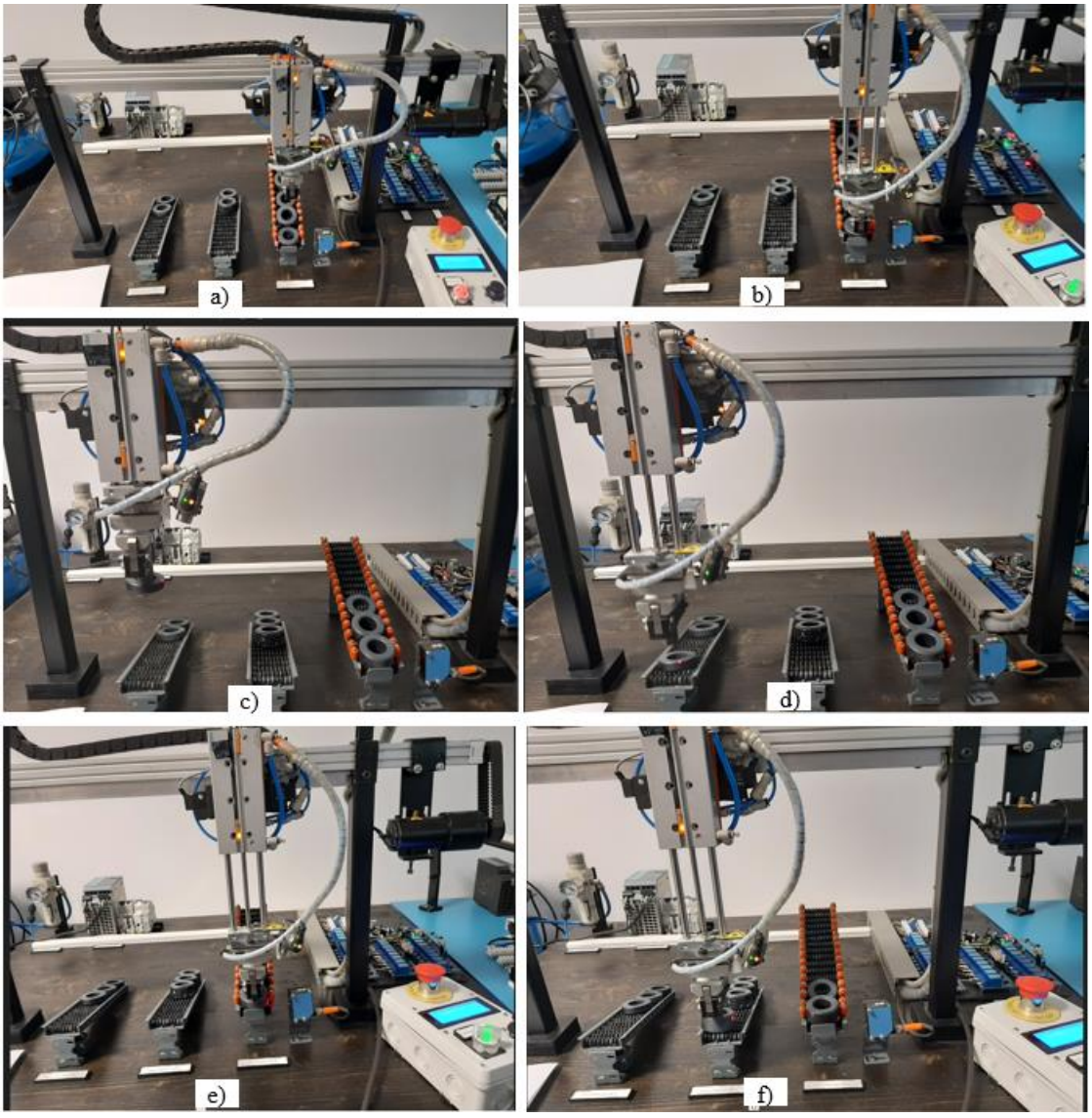

Fig. 9. Testing of experimental sorting system.

The states captured in the figure have the following meaning:

- State 1- the RM is in the initial position (Fig. 9 a);
- State 2 - the detection of B-type piece presence in the input stock, RM displacement for piece pickup (Fig. 9 b);
- State 3 - the RM displacement for storing the piece in the B type output stock (Fig. 9 c);
- State 4- depositing the piece in the B-type stock (Fig. 9. d).
- State 5- picking up the A-type piece from the input stock (Fig. 9 e).
- State 6- depositing the piece in the A-type stock (Fig. 9 f).

Experimental tests have demonstrated the precision of gripping and maintaining parts in the gripper due to the use of a high-performance sensor. Sensors that detect position also have good accuracy and a high response speed.

In the experimental tests, the correct functionality of the system for "manual operation" was checked. This mode of operation has been designed to avoid blockages in case of defects. Also in the "manual mode" the operator can execute the operations in the desired order.

The experimental tests have demonstrated the correct functioning of the system designed and realized in both automatic and manual operating mode.

V. CONCLUSIONS

The main benefits of using an automatic sorting station are:

• Presentation of specific and useful reports at user and management level;

• Exactly, real-time control of the operations carried out on the production line and in the storage area;

• Locating a product within the production flow and in the storage area;

• Real-time knowledge of the situation in the production process and in the storage area;

• Increasing the processing capacity of information and products;

• Optimizing human resources;

• Quality control.

All this benefits offered by the automatic sorting systems are intended to increase the capacity and efficiency of actions and also offer a higher level of process quality, ergonomics and optimization of customer services.

In the paper was designed and developed an automated sorting of pieces system that respond to the requirements of a flexible manufacturing system.

Infrastructure hardware and software used allows monitoring and control of a sorting station.

Sensors, electrical equipment and electronic components used for automatic system design have a high degree of accessibility and performance.

The system designed, developed and tested can be used both in educational applications in electrical engineering and in industrial applications.

ACKNOWLEDGMENT

Source of research funding in this article: Research program of the Electrical Engineering Department financed by the University of Craiova.

Contribution of authors:

First author – 70%

First coauthor – 30%

Received on July 17, 2022

Editorial Approval on November 26, 2022

REFERENCES

[1] *** "About flexible production systems and complex automation", Plant Engineering, XIII Year, no. 11 (118), 2013, pp. 42-45.

[2] T. Tolio, *Design of Flexible Production Systems*, Springer, 2009 ISBN: 978-3-540-85414-2.

[3] Toma L., "Acquisition systems and digital signal processing, "Vest" Publsher, Timişoara, 1996.

[4] W. Nawrocki, "Measurement Systems and Sensors", London, ARTECH HOUSE, 2005.

[5] *** https://www.cognex.com/industries/automotive/tire-and-wheel-systems/tire-tracking-and-sorting-automation

[6] L. Alboteanu, Manolea Gh., Ravigan F., "Automatic sorting and handling station actuated by pneumatic drive" *Annals of the University of Craiova, Electrical Engineering Series*, no 1, 2018, ISSN 1842-4805, pp.1-8.

[7] L. Alboteanu, "Automatic System for Handling Fragile Objects", Hydraulica-Magazine of Hydraulics, Pneumatics, Tribology, Ecology, Sensorics, Mechatronics, No. 4/2020, ISSN 145-7303, pp. 26-32;

[8] L. Alboteanu, "Automatic Processing Station Actuated by Pneumatic Drive", Hydraulica-Magazine of Hydraulics, Pneumatics, Tribology, Ecology, Sensorics, Mechatronics, No. 1/2019, ISSN 145-7303, pp. 16-22;

[9] D. J. Hucknall, Vacuum Technology and Applications, Elsevier, 2013, ISBN 1483103331.

[10] M.A. Drighiciu M.A., "Hydro pneumatic drive and automation", Publishing House of University of Craiova, Craiova, 2003.

[11] B. Robert, van Varseveld and G. M. Bone, ″Accurate Position Control of a Pneumatic Actuator Using On/Off Solenoid Valves″, ″IEEE/ASME Transactions on mechatronics″, vol. 2, no. 3, september, 1997, pp. 195-204;

[12] M. Avram, C. Bucşan, V. Banu, ″Innovative Systems for Incremental Positioning in Pneumatics″, ″Hydraulica″, No. 2/2015, ISSN 145-7303, pp. 52-56;

[13] C. Lazăr, O. Păstrăvanu, F. Schonberger, "Computer-assisted management of technical processes", Matrix Rom Publishing House, Bucharest, 1996;

[14] *** https://www.arduino.cc/

[15] *** https://www.smcworld.com/en-jp/

[16] *** http://www.festo.com/net/startpage/

[17] Ian Gorton. *Essential Software Architecture*. Springer publishing house, 2006.

[18] *** http://www.sei.cmu.edu/architecture/definitions.html

DOI: 10.52846/AUCEE.2022.08

Reactive Energy Compensation Equipment Used in High Power Laboratories

Daniel Constantin Ocoleanu*, Cristian-Eugeniu Sălceanu*, Mihai Ionescu*, Marcel Nicola*, Daniela Iovan* and Sorin Enache†

* Research Department - National Institute for Research, Development and Testing in Electrical Engineering – ICMET Craiova, România, pramlmp@icmet.ro, csalceanu@icmet.ro, mihai_ionescu_romania@yahoo.fr, marcel_nicola@icmet.ro, pdaniela@icmet.ro

† Faculty of Electrical Engineering - University of Craiova, Craiova, Romania, senache@em.ucv.ro

***Abstract* - The power quality covers the means to conserve energy resources, such means consist in improving the power factor and judiciously managing the reactive energy in the power system. Electric grids do not have an unlimited energy transmission capacity, therefore any load on the grid with reactive energy is measured by the energy distributor/supplier and billed to the consumer. On the premise that for industrial consumers, the main consumers of reactive energy are the low-load induction motors and transformers, this paper presents a synchronization equipment for a wound-rotor induction motor with a power of 2000 kW, nominal voltage 6kV, nominal current 210A, which allows the increase of the power factor, significantly reducing the reactive energy consumption. The equipment presented was designed, built, tested and validated by tests carried out in the high-power laboratory.**

Cuvinte cheie: *motor cu inducție, energie reactivă, factor de putere, motor sincron, motor asincron, laborator de încercări de mare putere.*

Keywords: *induction motor, reactive energy, power factor, synchronous-asynchronous motor, high-power testing laboratory.*

NOMENCLATURE

"R" – "L1" phase equivalent;
"S – "L2" phase equivalent;
"T" – "L3" phase equivalent;
"URS" – voltage between phase "L1" and phase"L2";
"URT" – voltage between phase"L1" and phase"L3";
"UTR" – voltage between phase"L3" and phase"L1";
"IR" – current corresponding to phase"L1";
"IS" – current corresponding to phase "L2";
"IT" – current corresponding to phase "L3";
"UR" –voltage corresponding to phase "L1";
"US" –voltage corresponding to phase "L2";
"UT" –voltage corresponding to phase "L3"[1].

I. INTRODUCTION

Electricity consumption is characterized by two quantities: active energy and reactive energy. Active energy is consumed for useful purposes, having useful effects (examples: operation of electric motors, heating, lighting, etc.). Reactive energy only circulates between the consumer and the energy supplier and is not actually consumed.

The power quality is a complex and controversial issue. Its complexity lies in the multitude of factors influencing it, in their interdependence, the lack of methods and means of obtaining expeditious and especially precise information about certain quantities which characterize it. Due to the fact that electricity is a commodity, its quality can be incorporated into a more general concept, related to the activity of its production, and, as a result, more than a hundred definitions can be assigned to the concept of quality without identifying a unanimously accepted one among them [2].

The use of highly efficient energy entailed the creation of extensive networks of transmission lines, transformer and distribution stations, regardless of the power demand, since electricity is readily available. It's only natural for rules to be created, laying down responsibilities for producers, as well as large consumers and the smallest consumers. The European Union (EU) has urged that the transmission and distribution networks be extended, imposing common tasks, laid down by modern rules on environmentally-friendly use and maintaining the power quality.

Asynchronous electric motors exert the greatest influence on the value of the power factor of the circuit they are part of, because they always require a magnetizing current [3].

In terms of the normal operation of electric consumers in general and electric cars in particular, the consumption of active and reactive electricity coexists and is inseparable. Problems arise in the analysis of the transmission of electricity remotely because the simultaneous flow of both active and reactive energy through the transmission lines decreases the transmission capacity of the lines, which can negatively influence the power quality made available by the producer, and this influence will be felt by all energy consumers. Major drawbacks are created by the generation of the reactive electricity in the transmission lines [4].

The value of the power factor of asynchronous motors depends on their degree of loading, in case of insufficient loading, the value of the power factor is considerably reduced.

A low power factor has a number of negative consequences for the operation of the electrical network, including: increased active power losses; additional investments;

increased network voltage drops; reduction of the power equipment output.

A high power factor reduces the flow of reactive power from the power plants to the consumers, reducing the losses of electrical energy to a minimum level determined by the technological consumption. In this way, an increase in the the efficiency of the electricity transmission, transformation and distribution installations, operational safety and a better use of the electrical network is obtained by reducing the apparent power with which it is loaded.

In the case of industrial consumers, the main consumers of reactive energy are induction motors and low-load transformers. Induction electric motors exert the greatest influence on the value of the power factor of the circuit to which they are connected. The value of the power factor depends on the load level of induction motors, in case of insufficient loading, the value of the power factor decreases considerably [5].

The main types of equipment used for the compensation of the power factor are:

- The use of capacitor banks;
- The use of reactors;
- Synchronous compensators;
- Synchronization of induction motors.

This paper presents the synchronization equipment for a wound-rotor induction motor with a power of 2000 kW, powered at a voltage of 6kV, which allows the increase of the power factor from 0.86 to 0.99, mainly aiming to reduce the transfer of reactive energy.

The reduction of the power factor (when transmitting the same active power) leads to the need to increase the apparent power of the generators in the power plants and the transformers of the energy system, due to the increase in current caused by the reduction of the power factor [6].

The diagram in fig.1. shows the change in the apparent power (in kVA) of the transformers, depending on the change in the power factor, when transmitting the same active power of 1000 kW.

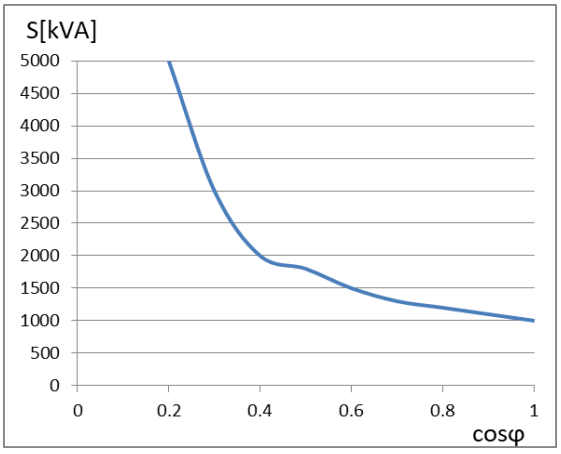

Fig.1 The graph of the power variation of the transformers in the power stations depending on the power factor.

In the case of a decrease in the power factor of the consumers, the capacity of active power transmission the transformers decreases, as a result of the increase in the reactive power. For the transmission to consumers of an active power of l000 kW, to a power factor equal to unity, a transformer of l000 kVA is required [7].

But if the power factor in the circuit decreases to 0.5, then a transformer with a power of 2000 kVA is needed to transmit the same active power (P=1000 kW).

The deterioration of the power factor also leads to the incomplete loading of the primary motors of the generators in power plants (the power of the primary motors is chosen based on the active power of the generators within the power stations).

Through this, the efficiency of the engines decreases and the operating characteristic of the entire installation worsens, leading to an increase in fuel consumption in the power plants.

The rest of the paper is structured as follows: Section II shows the overload behavior of wound-rotor induction motors, and Section III presents the equipment intended to reduce the transfer of reactive energy. The experimental results obtained using the synchronization equipment are presented in Section IV, while the conclusions are presented in the final section.

II. Overload Behavior of Wound-Rotor Induction Motors

Among the shortcomings specific to a synchronous motor, the insufficiency of overload resistance is very important, which represents the ratio between the maximum torque (for synchronous mode) and the nominal torque that corresponds to the catalog power of the motor.

The overload resistance depends on the intensity of the excitation current Iex and the relative value of the idle current (Io/In ratio) of the motor, for asynchronous mode.

The higher the Io/In ratio and also the higher the excitation current Iex, the higher the overload resistance of a synchronous motor [8].

Since the calculated excitation current Iex is limited due to the admissible heating of the rotor, it appears that it is practically not possible to increase the overload resistance by increasing the excitation current Iex.

Under these conditions, the overload resistance for synchronous mode is conditioned by the constructive qualities of the motor, which determine the internal magnetic resistance or the "Io/In" ratio.

$$u_{kr} = \frac{I_0}{I_n}\sqrt{1+\left(\frac{I_n}{I_0}\right)^2} = 1.04 \dots \dots 1.1$$

The "Io/In" ratio usually varies between 0.3 .....0.45.

The maximum torque of the synchronized motor differs very little from the nominal torque. If, in order to create the necessary stability, we start from the reserve coefficient, kreserve=1.5, the limit load coefficient of the synchronized motor, depending on stability, must be:

$$l_{engine\,limit} = \frac{u_{kr}}{k_{rezerve}} = \frac{1.04 \dots \dots 1.1}{1.5} = 0.7 \dots \dots 0.75$$

The power factor (PF) of an AC electricity system is defined in electrical engineering as the ratio of the actual power flowing towards the load to the apparent power

in the circuit, and is a dimensionless number in the range [-1,1];

The expression of the power factor is written as (1) :

$$PF = \frac{P}{S} \quad (1)$$

where: P - active power, S - apparent power.

In the sinusoidal mode, in the case of balanced three-phase circuits, the expression of the power factor can also be written as:

$$PF = \cos\varphi \quad (2)$$

The low power factor causes additional losses in the system: increases the current absorbed from the network to the same active power, increases losses in conductors, causes the increase of losses in transmission lines, reduces the available power in the system, decreases the stability of the energy distribution system. To deter a low-load power factor, most electricity suppliers impose certain forms of penalty [9].

According to national and international energy regulatory authorities, the rules applied in Romania have set a neutral power factor of 0.9 for both the inductive and capacitive mode

In order to comply with the regulations in force, to increase the power factor and minimize the transfer of reactive energy, a synchronization piece of equipment was achieved for a wound-rotor induction motor.

Induction motors exert the greatest influence on the value of the power factor of the circuit to which they are connected, due to the fact that they always require a magnetizing current, operating with a sub unitary power factor [10].

The value of the PF in induction motors depends on the load level, hence, if there is insufficient loading of the motors, there will be a considerable reduction in the power factor. This is due to the following main reasons:

- The magnetizing current of the induction motor, and respectively the reactive power varies in the case of load changes;
- The active power changes proportionally with the mechanical load in the shaft.

A low PF has the following consequences:

- Increased electricity losses due to the heating of cables and conductors of networks and windings of electric machines, because the heat losses are proportional to the square of the current (Joule-Lentz effect);
- Increased section and weight of cables and conductors;
- Increased apparent power of generators in power plants, incomplete use of prime movers, increased apparent power of transformers;
- The reduction of the power factor leads, in the case of the same active power, to the increase of the current and therefore to the increase of the voltage losses, which causes the reduction of the voltage to the consumers [11].

In this way, a low power factor has a negative effect, both for electricity supply companies and for industrial companies Among the specific drawbacks of a synchronized motor, the overload resistance is very important; it represents the ratio of the maximum torque (for the synchronous mode) to the nominal torque corresponding to the list power of the wound-rotor induction motor [12].

When the motor is out-of-step (in case of sudden drops of the power supply voltage or shocks of the load), alternating current begins to flow through the rotor winding with slip frequency, which causes an asynchronous torque. Variations in speed and current variation that occur in this case are undoubtedly damaging for both the motor and the conductors, but the use of automatic circuits for switching the motor to normal asynchronous mode at the time of overload and for returning to synchronous mode when the load has decreased removes these drawbacks [13].

III. Functional Description of a Reactive Energy Transfer Reduction Equipment

The periods of loading to nominal load of induction motors operating in the testing laboratories are intermittent, with a value of less than 1 minute, corresponding to the duration when the impulse generator, with a power of 2500MVA is brought to a state of energization, and the sample itself has a time range between 50ms÷3s, followed by pauses between two consecutive tests lasting between 10 minutes ÷ 30 minutes.

The method used by the test laboratory is intended for the production of equipment for the synchronization of low-load wound-rotor induction motors. This method is applied in situations where it is necessary to increase the power factor in order to reduce energy consumption [14].

The induction motors in the laboratory operate for a long time at low load, triggering shock generators with a power of 2500 MVA; these generators operate most of the time in de-energized state, so the driving motors of these generators operate at low load, generating a high consumption of reactive energy.

The motor actuates the rotor of a 2500MVA synchronous shock generator. Such equipment has been implemented in the testing laboratory for the synchronization of low-load wound-rotor induction motors, hence the optimal conditions are met for laboratory tests for electrical equipment [15].

Fig. 2 shows the diagram of operation of the synchronization equipment. This equipment is used for an induction 2000 kW power motor, 6 kV rated voltage, 2980 rpm rated speed [16].

The equipment for the synchronization of low-load wound-rotor power induction motors consists of a three-phase transformer, a three-phase rectifier with semiconductor diodes and RC filters, closing switches, switches, safety fuses. It is also equipped with control, measuring and signaling devices.

The TTA 20kVA transformer is powered by the 400V AC network via fusible fuses F1, F2, F3, Cs closing switch and RT thermal relay.

The parameters of the transformer, rectifier and devices of the power circuit have been determined according to the power of the wound-rotor induction motor, which is 2000kW.

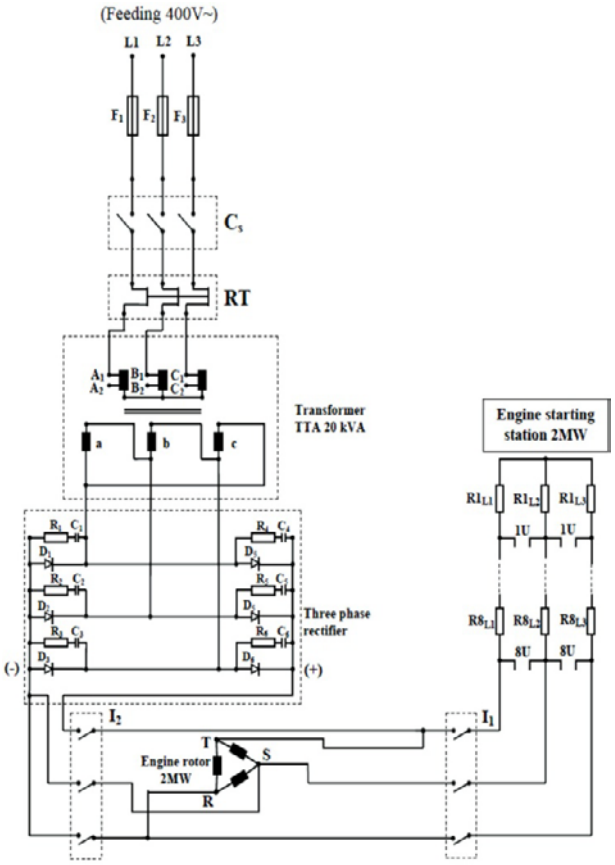

Fig. 2. Synchronization equipment diagram.

In the asynchronous mode, the setting of the devices is as follows: switch I_1 – closed, switch I_2 – open and closing switch C_s – open. In the synchronous mode, the setting of the devices is: switch I_1 – open, contacts $U_1 \div U_8$ related to the closing switches for short-circuiting the resistance steps used to start the wound-rotor induction motor– closed, switch I_2 – closed, closing switch C_s – closed.

The motor starts in the asynchronous mode with the rheostatic feature, using a starting station which consists of 8 resistance steps. As the motor accelerates, one resistance step is short-circuited at a time, until all eight resistance steps are short-circuited, and the motor reaches the rated speed.

In fig.3, the starting current is oscillographed as a function of time, and the time instant and the current value to which each resistance stage is short-circuited can be noted.

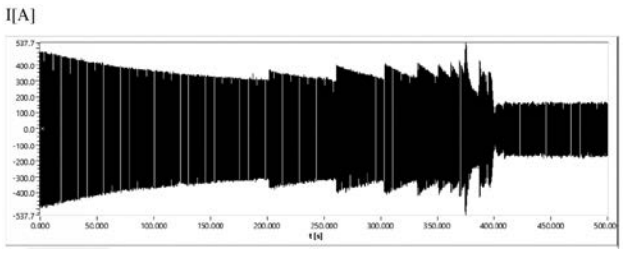

Fig. 3 Starting the asynchronous motor

After the motor has reached the rated speed, the synchronization circuit is automatically powered by the normal open auxiliary contact 8U of the closing switch which short-circuits the last resistance step of the rheostatic starting station, as well as by the normal closed auxiliary contact of the compressed-air operating switch, with high breaking capacity (12kV rated voltage, 120kA RMS breaking current), which is part of the power circuit of the high power laboratory.

The closing of switch I_2 triggers the automatic opening of switch I_1.

Using an auxiliary conditioning circuit, the closing of switch I_2 is initiated when the current crosses zero; this circuit is shown in Fig. 4.

This module is used to limit the maximum currents in the stator when switching from asynchronous to synchronous mode. Basically the transition from one mode to another is performed when the current measured in the stator on phase R crosses zero.

Before performing tests in the high-power laboratory, the closing of the operating switch with high breaking capacity of the laboratory's power circuit triggers the opening of switch I_2, this triggers in turn the closing of switch I_1, hence switching from synchronous mode to asynchronous mode, to protect the induction motor during the tests.

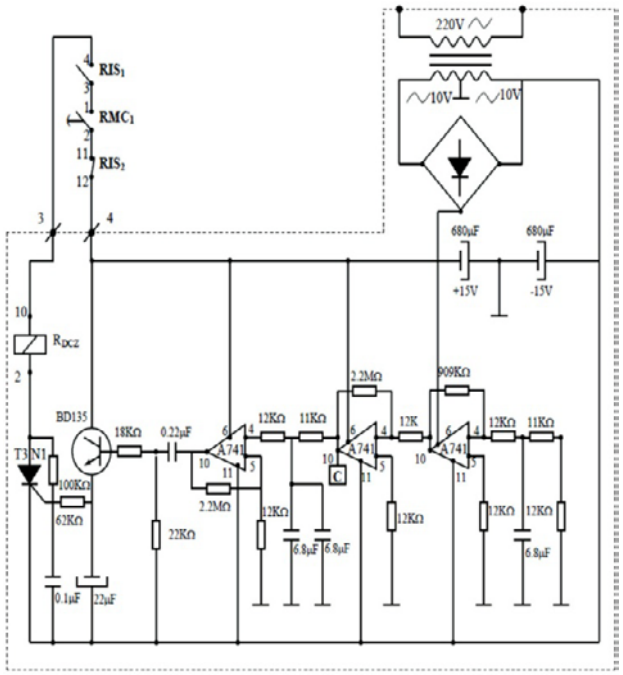

Fig.4. I2 switch conditioning module when the current crosses zero.

Moreover, the transition from synchronous to asynchronous mode is performed automatically when disconnecting the motor from the network as well as during the operation of the induction motor protection (See fig.4).

When the engine is out-of-step (in case of voltage drops or load shocks), alternating current flows through the rotor winding with slip frequency that causes asynchronous torque. Variations in speed and current variation that occur in this case are damaging for both the motor and the conductors.

The implementation of automatic circuits for switching the motor to normal asynchronous mode at the time of overload and for returning to synchronous mode when the load has decreased removes these drawbacks [16].

IV. Experimental Results Obtained Using the DISMAP Synchronization Equipment

Nominal data of the drive motor 2 MW type ATM 2500-2

- Nominal power - 2 MW;
- Nominal voltage - 6 kV;
- Stator current - 210 A;
- Speed - 2980 rpm;
- Engine performance - 95.1%;
- Power factory - cos φ 0.86;
- Rotor voltage - 1330 V;
- Rotor current - 920 A;
- Rotor weight - 3650 kg;
- Total engine weight - 15865 kg;
- Air consumption - 3 m3/second;
- Oil flow through the bearing - 25 liters/minute.

Fig. 5. Asynchronous motor with wound rotor, type ATM 2500 -2

To obtain the experimental data, the high-performance, 8-channel, 16-bit, fiber optic acquisition system *Transient Recorder Tras Mobile* was used, with a sampling rate of 100kS/s (10μs between 2 points), (see Fig. 5).

Fig. 6. TRAS Mobile acquisition system.

HVT 50 RCR 50kV/50V voltage dividers were used for voltage measurement, and CWT15R (500A/V) 3000 A peak Rogowski belts were used for current measurement (see Fig. 6).

Fig. 6. Current and voltage measurement acquisition system.

By closing switch I_2, which is conditioned by the conditioning module shown in Fig. 2 to close when the current crosses zero, the rotor winding of the induction motor is supplied by direct current, obtained from the rectifier of the DISMAP synchronization equipment, and, after several current steps, considered harmless to the motor, the transition from asynchronous mode to synchronous mode is performed.

Fig. 7 shows the currents in the stator of the 2000-kW power induction motor, corresponding to the phases IR, IS, IT when switching from asynchronous to synchronous mode.

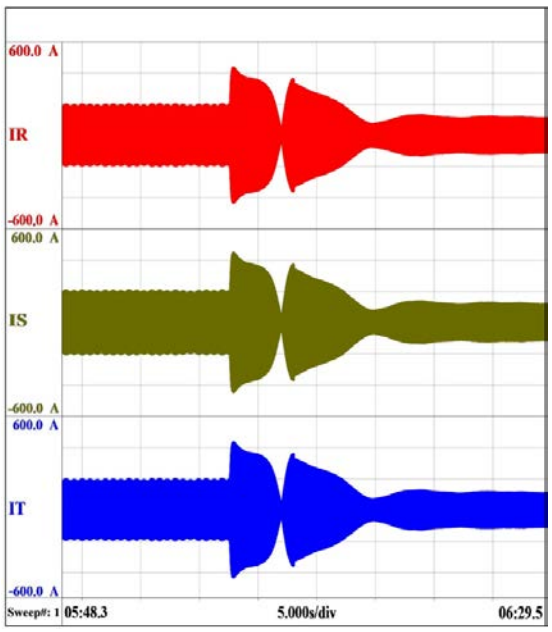

Fig.7. Transition from asynchronous to synchronous mode.

The values of the currents measured in the stator of the motor in asynchronous and respectively synchronous mode are presented in Table I:

TABLE I.
VALUES OF PHASE CURRENTS

	Phase currents in asynchronous mode	**Phase currents in synchronous mode**
IR_RMS	136.589 A	76.6227 A
IS_RMS	142.537 A	80.1198 A
IT_RMS	135.720 A	75.0794 A

The 142.537A peak current in the stator of the motor in asynchronous mode is recorded on phase S. After achieving the synchronism conditions, the peak current value in the stator of the motor is of 80.1198A. This decrease in currents occurs on the three phases, as evidenced by the data in Table I. There is a substantial decrease in the currents measured in the stator of the induction motor when using the DISMAP synchronization equipment.[16]

The values of the average power factor recorded for the asynchronous and synchronous modes are presented in table II.

TABLE II.
POWER FACTOR VALUES

	PF in asynchronous mode	PF in synchronous mode
Phase R	0.65	0.99
Phase S	0.65	0.99
Phase T	0.65	0.99

Fig. 8 and Fig. 9 shows the oscillograms which reveal the phase shift between voltage and current in asynchronous/synchronous mode on the three phases.

Once the synchronization is achieved by using the synchronization equipment, there is an increase in the power factor, from 0.65 (asynchronous mode) to 0.99 (synchronous mode), thus reaching the value imposed by the Romanian energy regulatory authority (0.9).

The use of synchronization equipment for low-load wound-rotor induction motors leads to a substantial reduction of monthly costs. The performance of this DISMAP synchronization equipment led to a reduction of almost 50% in the active energy consumption and also a reduction of almost 60% in the reactive energy consumption, which was determined by comparing monthly invoices before and after the implementation of the equipment.

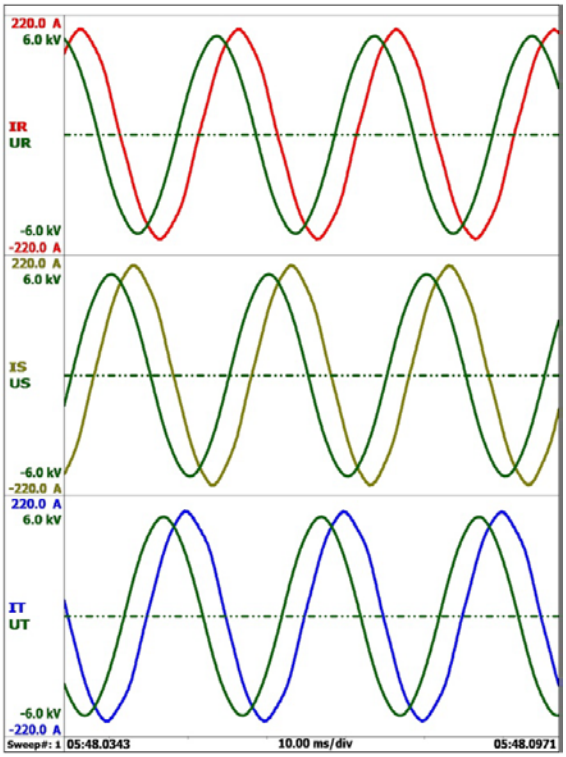

Fig. 8 Voltage – current phase shift in the stator in asynchronous mode.

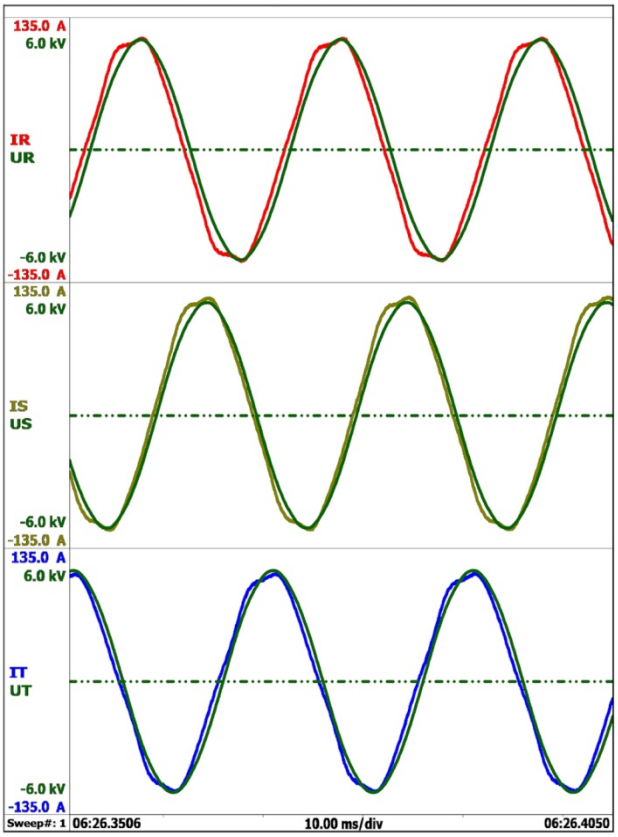

Fig. 9. Voltage – current phase shift in the stator in synchronous mode.

V. CONCLUSIONS

This paper presents the synchronization equipment and its performance, which led to a reduction of almost 50% in the active energy consumption and also a reduction of almost 60% in the reactive energy consumption, and this was determined by comparing monthly invoices before and after the implementation of the equipment.

The implementation of this synchronization equipment for the low-load wound-rotor induction motors allows the increase of the average power factor from 0.65 in asynchronous mode to 0.99 in synchronous mode, substantially reducing both the active energy consumption and the reactive energy consumption.

The equipment has shown high performance in reducing the reactive energy consumption and increasing the power factor, and it was incorporated into the laboratory test circuit for high-power equipment [16].

ACKNOWLEDGMENT

This work was developed with the support of the Ministry of Research, Innovation and Digitization within the national program: Installations and Objectives of National Interest - "Production, measurement and recording system of short-circuit currents - SPMICS".

Contribution of authors:
First author – 50%;
First coauthor – 10%;
Second coauthor – 10%;
Third coauthor – 10%;

Fourth coauthor – 10%;
Fifth coauthor – 10%.

Received on July 31, 2022
Editorial Approval on November 26, 2022

REFERENCES

[1] "IEEE Standard Definitions for the Measurement of Electric Power Quantities Under Sinusoidal, Nonsinusoidal, Balanced, or Unbalanced Conditions", in IEEE Std 1459-2010 (Revision of IEEE Std 1459-2000), pp.1-50, 19 March 2010

[2] EN 50160:2010 - Voltage Characteristics in Public Distribution Systems, https://copperalliance.org.uk/uploads/2018/03/542-standard-en-50160-voltage-characteristics-in.pdf

[3] "IEEE Recommended Practice for the Design of Reliable Industrial and Commercial Power Systems - Redline", in IEEE Std 493-2007 (Revision of IEEE Std 493-1997) - Redline, pp.1-426, 25 June 2007.

[4] "IEEE Draft Guide for Identifying and Improving Power Quality in Power Systems", in IEEE P1250/D6, October 2017, pp.1-67, 1 Jan. 2017.

[5] A. Cataliotti, V. Cosentino, S. Nuccio, "The measurement of reactive energy in polluted distribution power systems: an analysis of the performance of commercial static meters," IEEE Transactions on Power Delivery, vol. 23, no. 3, pp. 1296–1301, July 2008.

[6] B. A. Konstantinov, Cum poate fi îmbunătățit factorul de putere în intreprinderile industriale (Traducere din limba rusă), Editura tehnică, 1961.

[7] D. Comsa, S. Darie, V. Maier, M. Chindriș - Proiectarea instalațiilor electrice industriale, Editura didactică și pedagogică, București, 1979.

[8] V. I. Kotenev, A. V. Kotenev, A. D. Stulov, "Controlling the Reactive Power Factor of a Combined Load Power Supply System and the Correction of Program as a Function of Current Power Consumption", in Proceeding of International Ural Conference on Electrical Power Engineering (UralCon), Chelyabinsk, Russia, 22-24 Sept. 2020, pp. 171-176, DOI: 10.1109/UralCon49858.2020.9216286.

[9] Y. Kabir, Y. M. Mohsin, M. M. Khan, "Automated power factor correction and energy monitoring system", in Proceeding of Second International Conference on Electrical, Computer and Communication Technologies (ICECCT), Coimbatore, India, 2017.

[10] F. Zheng and W. Zhang, "Long term effect of power factor correction on the industrial load: A case study", Australasian Universities Power Engineering Conference (AUPEC), Melbourne, VIC, Australia, 19-22 Nov. 2017, pp. 1-5, DOI: 10.1109/AUPEC.2017.8282382.

[11] C. C. Cămui, V. Petre, V. Boicea, "Power Factor Correction: a Hands-on Introduction for Students", International Conference and Exposition on Electrical And Power Engineering (EPE), 2020, pp. 314-317, DOI: 10.1109/EPE50722.2020.9305625.

[12] V. Sehwag, V. Dua, A. Singh, J. N. Rai and V. Shekhar, "Power Factor Correction Using APFC Panel on Different Loads", 2018 2nd IEEE International Conference on Power Electronics, Intelligent Control and Energy Systems (ICPEICES), 2018, pp. 73-77, DOI: 10.1109/ICPEICES.2018.8897359.

[13] Ahmed A. AbdElhafez, Saud H. Alruways, Yazeed A. Alsaif1, Mutlaq F. Althobaiti, Abdulmohsen B. AlOtaibi, Naif A. Alotaibi, "Reactive Power Problem and Solutions: An Overview", in Journal of Power and Energy Engineering, no 5, pp.40-54, 2017, DOI: 10.4236/jpee.2017.55004 May 26, 2017.

[14] X. Zhou, Y. Ma, Z. Gao and S. Zhang, "Reactive power compensation in motor, 2017 IEEE International Conference on Mechatronics and Automation (ICMA)", 2017, pp. 295-299, DOI: 10.1109/ICMA.2017.8015831.

[15] V. Shestakov, "Application of Complete Factorial Experiment to Optimize Parameters of Frequency-Controlled Asynchronous Motor in Order To Improve Its Energy Indicators", 2020 International Conference on Industrial Engineering, Applications and Manufacturing (ICIEAM), 2020, pp. 1-5, DOI: 10.1109/ICIEAM48468.2020.9111953.

[16] [16] D. Ocoleanu, C. Salceanu, M. Ionescu, M. Nicola, C. Nitu, S. Enache, C.Marinescu, "Reactive Energy Transfer Reduction Equipment for Low-Load Wound-Rotor Induction Motors",International Conference on Electromechanical and Energy Systems (SIELMEN), October 06, 2021, Iasi, Romania and October 07-08, 2021, Chisinau, Rep. Moldova.

DOI: 10.52846/AUCEE.2022.09

Comparative Analysis in the Case of Indirect Current Control in a Shunt Active Filtering System

Mihăiță Daniel Constantinescu, Mihaela Popescu, Cosmin-Ionuț Toma, Constantin Vlad Suru
University of Craiova, Faculty of Electrical Engineering,
mconstantinescu@em.ucv.ro, mpopescu@em.ucv.ro, ctoma@em.ucv.ro, vsuru@em.ucv.ro

Abstract **- In this paper, the performance of a three-phase four wire shunt active power filter (APF) using indirect current control with active load current calculation was compared with that corresponding to using indirect current control with prescribed current calculation from the voltage controller. It is clear that, under balanced and sinusoidal voltage conditions, these two methods give similar results. The variant of the indirect current control with prescribed current calculation from the voltage controller has the advantage of simplicity, but exhibits increased sensitivity to voltage ripples on the compensation capacitor, as they are reflected in the output of the voltage controller. The whole system was modeled using MATLAB-SIMULINK software. The simulation results demonstrate the applicability of both methods for APF control.**

Cuvinte cheie: *Filtru activ de putere, control indirect al curentului, calculul curentului activ al sarcinii.*

Keywords: *Shunt Active Power Filter, Indirect current control, Active Load Current Calculation*

I. INTRODUCTION

After identifying the existence of current and/or voltage harmonics in an electrical system, the problem arises of finding and implementing solutions to solve the problems they generate. In adopting them, the possibility of compensating the reactive power and imbalances generated by the load is also taken into account.

Active Power Filters (APF) are inverter-type static converters, bidirectional in current and voltage, controlled in such a way as to absorb the harmonics that must be eliminated from the network and equipped with a circuit component for energy storage on the DC side [1], [2].

Because of their particular objective of improving the current waveform rather than controlling the transferred power, active power filters have also been called "Active Harmonics Conditioners" (AHC) or "Active Power Line Conditioners" (APLC).

There are many control methods of the current in the shunt APF, so that the current injected into the power supply follows its reference value [3]–[5].

The need to control also the voltage across the compensation capacitor in the DC side must be mentioned [1]–[8].

Clearly, the control system of an APF contains an outer loop for regulating the voltage on the compensation capacitor and an inner loop for regulating the current. The output of the current controller determines the sequences of gate drive signals for APF's semiconductor devices.

On the other hand, the structure of the current control loop is determined by the adopted control algorithm.

The performance of the active filtering is significantly affected, both by the technique adopted for the reference currents generation and by the current control technique [1], [4], [6], [9].

Depending on the controlled current in the regulation scheme, there are two control methods, the direct control and the indirect control, respectively.

The direct current control involves the direct regulation of the current at the output of the inverter.

In this case, the main component of the current prescribed to the current controller is the compensating reference current, to which the active component necessary to cover the losses in the system is added. The latter causes the voltage on the compensation capacitor to be maintained at the prescribed value [1], [10]–[14].

The indirect control consists of controlling the supply current and involves prescribing its waveform that corresponds to the desired supply current.

The advantage consists in the simpler way of calculation and in the fact that the current controller operates with sinusoidal signals having the pulsation of the power supply network [1], [15]–[18].

Referring to the objectives of active filtering, the indirect current control is preferable when zero current distortion or unity power factor is desired after compensation.

In this case, it can lead to a simpler control structure by significantly reducing the computational requirements and time.

There are two ways to obtain the active load current, either based on the output of the voltage controller, or by extracting it from the total load current [1].

Following the numerical simulation study of the two compensating current calculation methods, for a typical nonlinear load topology, some comparative conclusions could be drawn.

The remaining of the paper is organized as follows. Section II presents the algorithm for the indirect current control for the two ways of obtaining the active current of the load. Section III is dedicated to the presentation of the virtual implementation of the whole active filtering system. The simulation results are illustrated in Section IV.

Some final conclusions are formulated at the end of the paper.

II. The Algorithm for the Indirect Current Control

A. The Indirect Current Control Based on the Voltage Controller Output

The first variant of the active power filter control algorithm is the indirect current control based on the voltage controller output [1], [17], [19]. It contains two cascaded control loops, the desired grid current being obtained from the voltage controller (the amplitude) and its waveform and phase is provided by a phase locked loop (PLL) circuit from the supply voltages (Fig. 1). Fig. 1 illustrates:

- The control loop for the DC-voltage across the compensating capacitor, which gives the desired amplitude of the power supply current;
- The power supply current control loop, whose operation determines the necessary gating signals for the APF's semiconductor devices, so as to obtain the desired current absorbed from the network. Therefore, the filter current is obtained intrinsically, not being directly controlled by the current control loop. The following notations are used in Fig. 1:

VC - compensating capacitor voltage (the voltage transducer measured the voltage across both capacitors, connected in series; the central socket is connected to the power grid neutral point;

APF - active power filter power section;

VT - voltage transducer;

CT - current transducer;

i* - prescribed power supply instantaneous current;

i - power supply instantaneous current.

B. The Indirect Current Control with Load Active Current Computation

The control scheme associated to the indirect current control with load active current computation is shown in Fig. 2. In this case, only the component of the prescribed current associated of the power losses (I_{Fa}) is provided by the voltage controller.

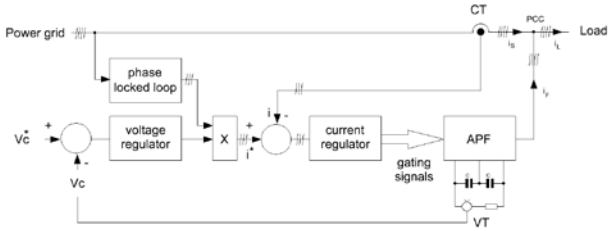

Fig. 1. Diagram of the indirect current control based on the voltage controller output.

Thus, to reduce the negative effect of the voltage controller output ripple on the compensated current shape (given the high value of this signal), the power supply desired current amplitude is computed as the sum of the voltage controller output (I_{Fa}) and the load active current amplitude (I_{La}).

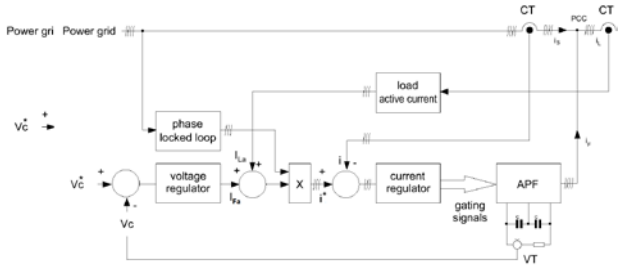

Fig. 2. Diagram of the indirect current control with load active current computation.

The load active current is obtained based on the load active power:

$$I_{LaRMS} = \frac{\sum_{k=1}^{3} \frac{1}{T} \int_{0}^{T} u_{sk} \cdot i_{Lk} dt}{\sum_{k=1}^{3} U_{sk}} \quad (1)$$

where:

- I_{LaRMS} - load current active component, RMS value;
- U_{sk} - power supply voltage RMS value of phase k;
- u_{sk} - power supply instantaneous voltage on phase k;
- i_{Lk} - load instantaneous current on phase k.

For the both current control methods, the voltage controller of PI (proportional-integrative) type is tuned based on the modulus criterion [20], [21].

Considering the adaptive capacitor voltage control, the voltage controller parameters are real-time adapted to the non-active power to be compensated [22].

The power supply current control loop uses hysteresis type controllers which gives the gating signals for the active filter power transistors. The switching frequency is limited by the hysteresis band on one hand and by the time sample (simulation step) on the other hand.

III. Virtual Implementation

For the simulation of the entire active filtering system operation, both variants of the control algorithm were implemented in the Matlab-Simulink environment. The load was the same in all studied cases, namely an uncontrolled three-phase bridge rectifier, with an RLC load. The specific sections of the scheme have been grouped into masked subsystems. The control section was also grouped in a Simulink subsystem, for easy migration from one algorithm variant to the other. The complete active filtering virtual system is illustrated in Fig. 3.

The initialization of the active power filter is done according to the typical steps [1]:

- the power section is connected to the grid by means of current limiting resistors (the capacitor is charged via the power inverter anti-parallel diodes);
- the resistors are short circuited when the compensating capacitor voltage reaches about 80% of the maximum voltage;
- the compensating capacitor is actively charged to the working voltage (the control loops are active), by absorbing from the power grid the necessary active current;

- the initial capacitor voltage is the voltage on the capacitor at the closed loop control system startup time.

The desired power grid current is obtained by multiplying the voltage controller output signal with the voltage template, received from the PLL circuit:

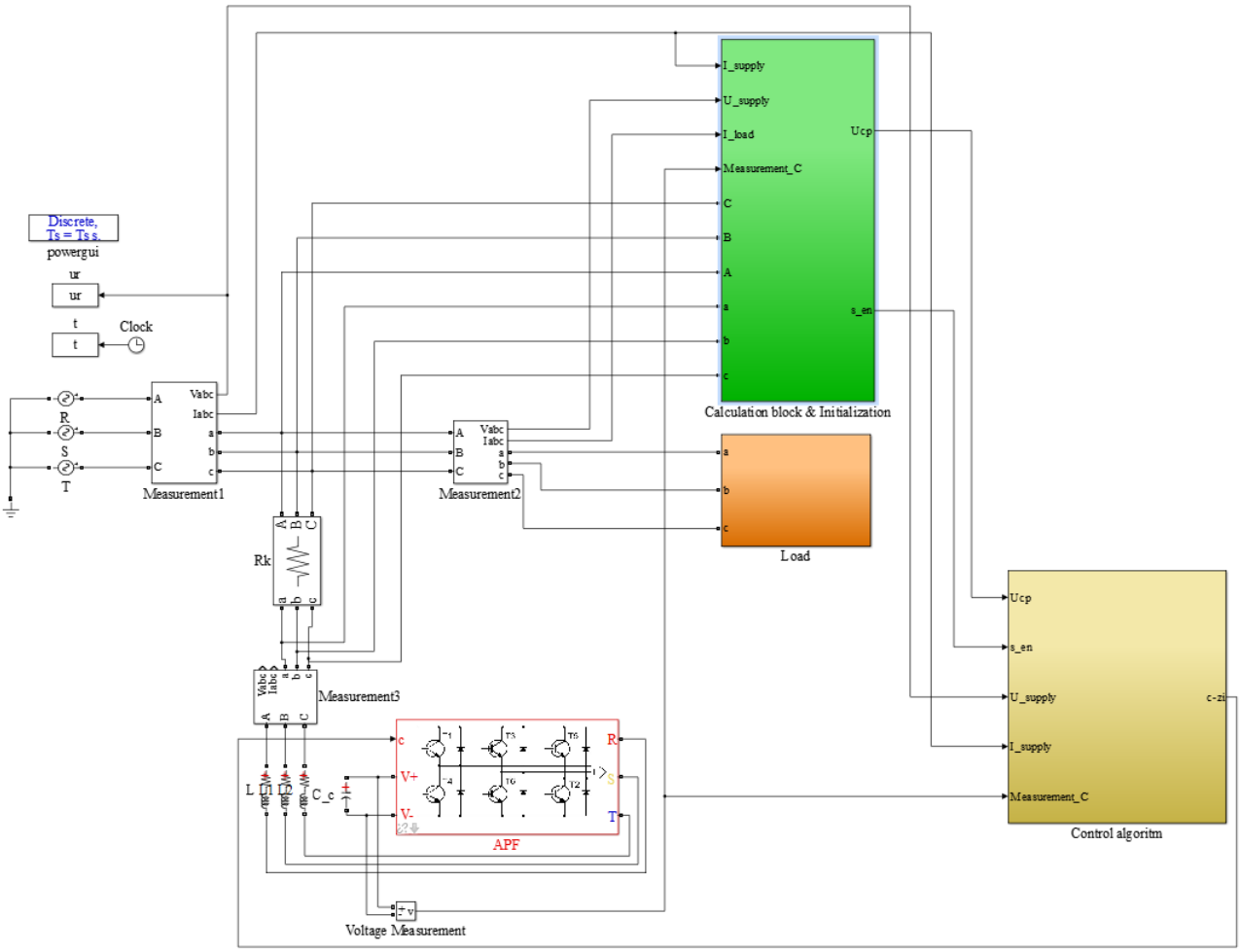

Fig. 3. Virtual model for the active power filtering system.

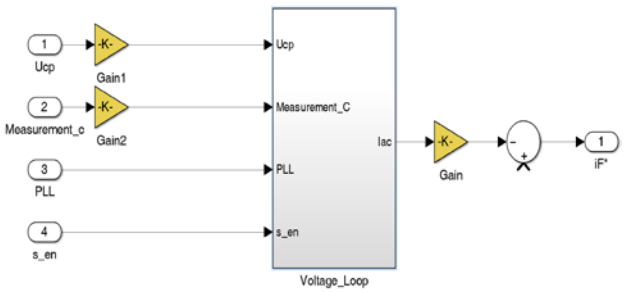

Fig. 4. Indirect current control method based on the voltage controller output.

- for the control method based on the load current active component, the desired power supply current is given by the sum between the load current active component (which is also the desired compensating current) and the voltage controller output (which gives the active current drawn from the power supply to charge the compensating capacitor and to cover the active power filter losses (Fig. 5);

- for the control method based on the voltage controller, the power supply desired current amplitude is given only by the voltage controller (Fig. 4);

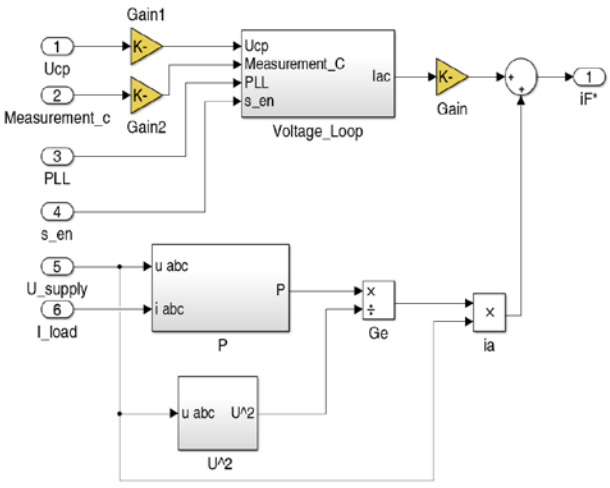

Fig. 5. Indirect current control method based on the load current active component.

The algorithm was modified to allow compensation validation from an external signal for both indirect current control approaches, even though this cannot be done natively.

Fig. 6 (a and b) illustrates the voltage control loop and the current control loop in detail.

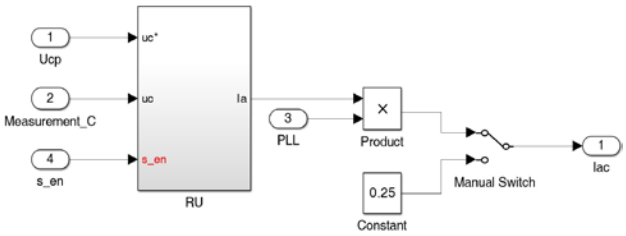

a)

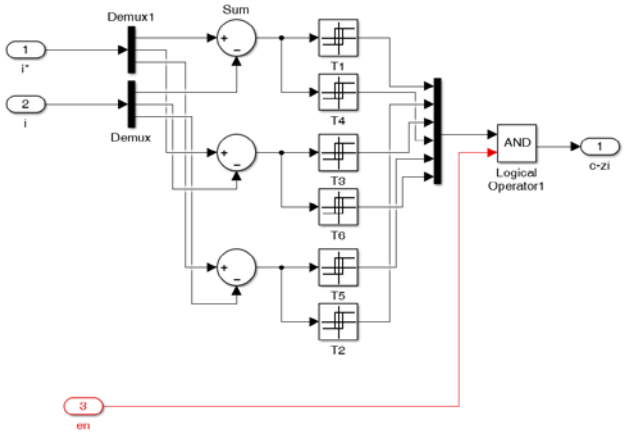

b)

Fig. 6. Virtual model for: a) the compensating capacitor voltage control loop; b) the desired supply current control loop.

IV. Simulation Results

A. *The Indirect Current Control Based on the Voltage Controller Output*

Fig. 7 shows the waveforms of the supply voltage (in black) and the power supply current (in red). It can be seen that the simulation is done for total compensation, the fundamental component of the current being in phase with the voltage.

Fig. 8 shows the waveforms of the real supply current (in blue) and the prescribed supply current (in red).

The evolutions of the voltage on the compensation capacitor (in blue) and its prescribed value (in red) are shown in Fig. 9 for the entire charging process of the capacitor. The same voltages in steady state regime are illustrated in Fig. 10.

Table I shows the energy indicators specific to the simulation in the case of indirect current control with the calculation of the prescribed current from the voltage controller.

The total harmonic distortion factor (THD) is calculated taking into account all harmonics of the current and the partial harmonic distortion factor (PHD) is calculated taking into account the harmonics up to order 51.

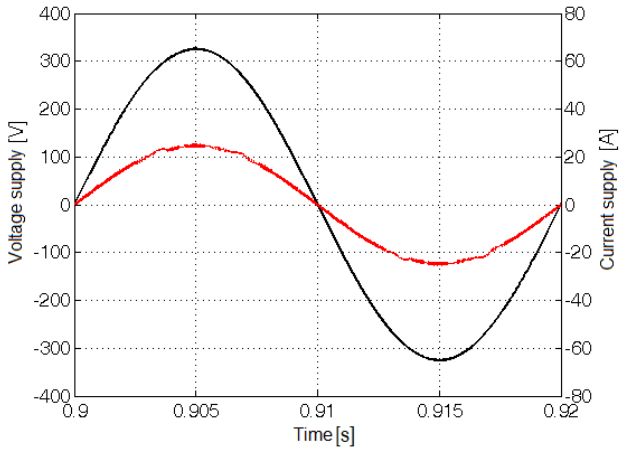

Fig. 7. The waveforms of the supply voltage (in black) and the power supply current (in red) for the indirect current control method based on the voltage controller output.

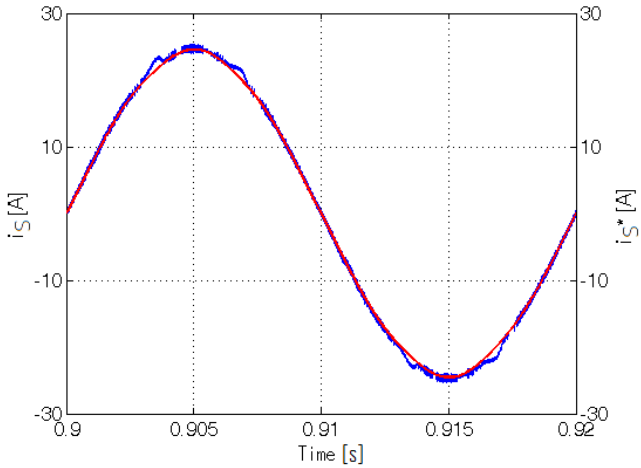

Fig. 8. The waveforms of the obtain supply current (in blue) and the prescribed current (in red) for the indirect current control method based on the voltage controller output.

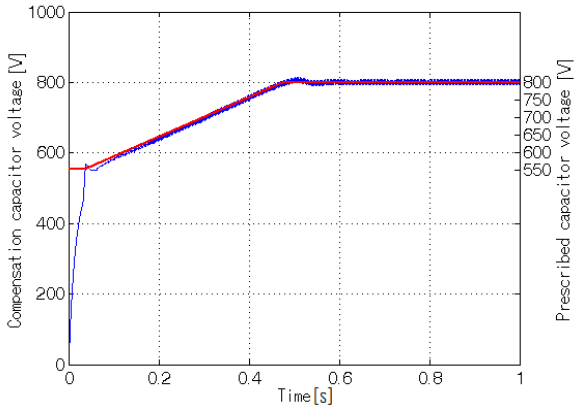

Fig. 9. Waveforms of the compensation capacitor voltage (in blue) and the prescribed capacitor voltage (in red) for the indirect current control method based on the voltage controller output.

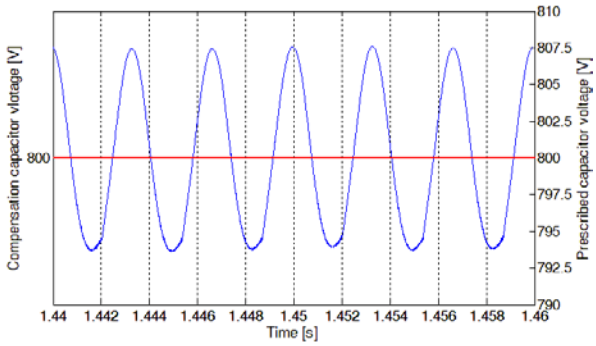

Fig. 10. Waveforms of the compensation capacitor voltage (in blue) and the prescribed DC voltage (in red) for the indirect current control method based on the voltage controller output.

TABLE I.
ENERGY INDICATORS WHEN THE CALCULATION OF THE PRESCRIBED CURRENT IS FROM THE VOLTAGE CONTROLLER

Load current (RMS)	20 A
Power supply current (RMS)	17.49 A
Active power	12.08 kW
Apparent power	12.09 kVA
Load current THD	75.4 %
Power supply current THD	2.04 %
Load current PHD	1.17 %
Power supply current PHD	75.4 %
Efficiency	89.74 %

B. The Indirect Current Control with Load Active Current Computation

In this case, the waveforms of the supply voltage and the power supply current are shown in Fig. 11. It can be seen that the current is almost sinusoidal and in phase with the supply voltage.

Fig. 12 illustrates the real current together with the compensating current.

The time evolution of the voltage on the compensation capacitor compared with the prescribed DC voltage is shown in Fig. 13. Their waveforms in steady state regime are illustrated in Fig. 14.

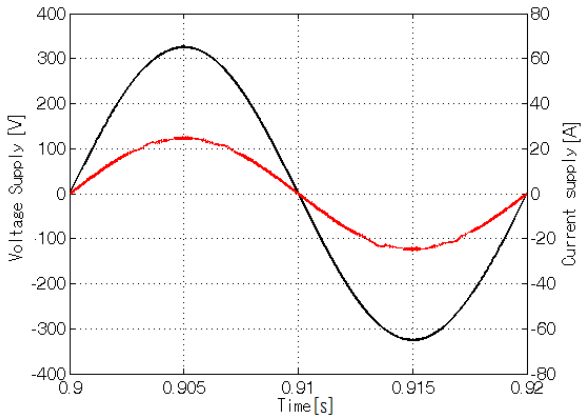

Fig. 11. The waveforms of the supply voltage (in black) and the power supply current (in red) for the indirect current control method based on the load current active component.

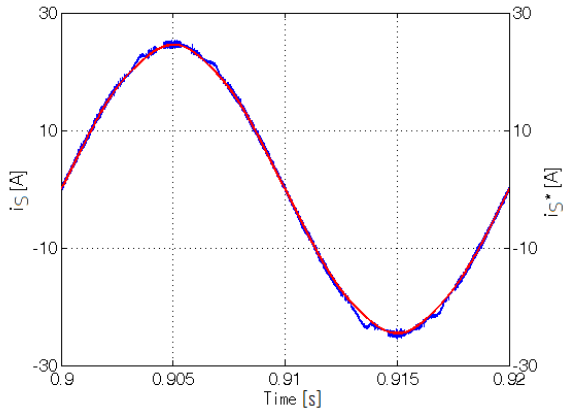

Fig. 12. The waveforms of the obtain supply current (in blue) and the prescribed current (in red) for the indirect current control method based on the load current active component.

Table II synthesizes the energy indicators specific to the simulation in the case of the indirect current control with load active current computation.

TABLE II.
ENERGY INDICATORS WHEN THE CALCULATION OF THE PRESCRIBED CURRENT IS WITH LOAD ACTIVE CURRENT COMPUTATION

Load current (RMS)	20 A
Power supply current (RMS)	17.48 A
Active power	12.051 kW
Apparent power	12.054 kVA
Load current THD	75.4 %
Power supply current THD	2.1 %
Load current PHD	1.29 %
Power supply current PHD	75.4 %
Efficiency	89.98 %

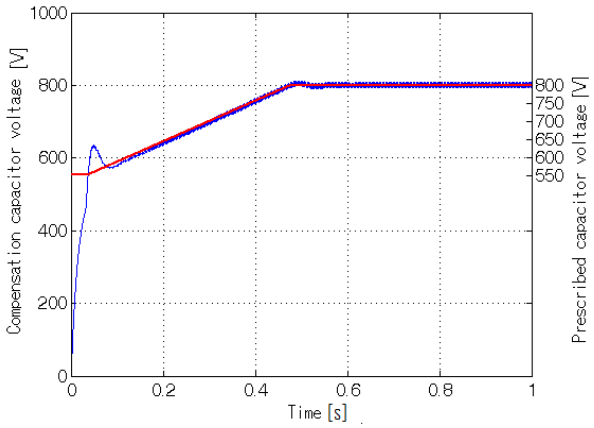

Fig. 13. Waveforms of the compensation capacitor voltage (in blue) and the prescribed voltage (in red) for the indirect current control method based on the load current active component.

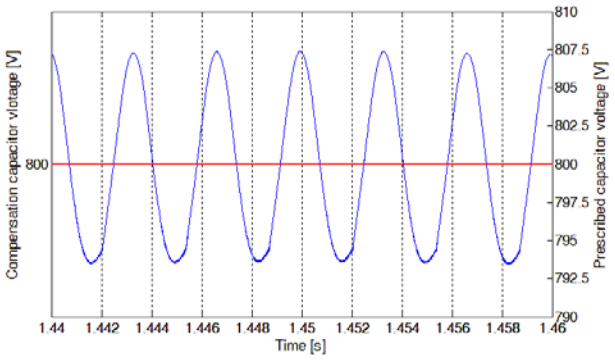

Fig. 14. Waveforms of the compensation capacitor voltage (in blue) and the prescribed DC voltage (in red) for the indirect current control method based on the load current active component.

It can be seen that, the indirect control with the calculation of the prescribed current from the voltage controller leads to a slight increase in active filtering efficiency (36.9, compared to 35.9 in the case of the indirect control with the calculation of the active current of the load). It must be specified that the active filtering efficiency has been calculated as the ratio of the distorted load current THD and supply current THD after compensation.

V. Conclusions

The control algorithm for the three phase four wire active power filter was implemented in the Matlab-Simulink environment for the two indirect current control methods.

Following the numerical simulation study of the two methods of indirect current control, some comparative conclusions could be drawn. From a qualitative point of view, the waveform of the compensated current was almost sinusoidal in both cases. It remains a harmonic current distortion due to the switching operation of the active power filter, specific to the current control with hysteresis controller.

Differences between the performances obtained by the two current control methods could be observed quantitatively based on power quality indicators.

The indirect control without extracting the active load current naturally allows the operation of the active power filter in regeneration mode, sending an active current into the power supply.

Acknowledgment

Source of research funding in this article: This work was supported by the Grant POCU380/6/13/123990, co-financed by the European Social Fund within the Sectorial Operational Program Human Capital 2014 – 2020.

Contribution of authors:
First author – 40%
Second coauthor – 20%
Third coauthor – 20%
Fourth coauthor – 20%

Received on July 20, 2022
Editorial Approval on November 20, 2022

References

[1] A. Bitoleanu, M. Popescu, C. V. Suru, *Filtre active de putere. Fundamente şi aplicaţii*. Ed. Matrix, Bucureşti, 2021.

[2] Z. Salam, T. P. Cheng, A. Jusoh, "Harmonics mitigation using active power filter: A technological review," *Elektrika Journal of Electrical Engineering*, vol. 8, no. 2, 2006, pp. 17-26.

[3] T. C. Green, J. H. Marks, "Control techniques for active power filters," *IEE Proceedings - Electric Power Applications*, vol. 152, issue 2, March 2005, pp. 369- 381.

[4] Y. Hoon, M. A. M. Radzi, M. K.Hassan, N. F.Mailah, "Control algorithms of shunt active power filter for harmonics mitigation: A review," *Energies*, 2017, 10, 2038.

[5] R. Rajagopal, K. Palanisamy, S. Paramasivam, "A technical review on control strategies for active power filters," *2018 International Conf. on Emerging Trends and Innovations in Engineering and Technological Research*, Ernakulam, 2018, pp. 1-6.

[6] K. Kamel, Z. Laid, K. Abdallah, "Mitigation of harmonics current using different control algorithms of shunt active power filter for non-linear loads," *2018 International Conference on Applied Smart Systems (ICASS)*, Medea, Algeria, 2018, pp. 1-4.

[7] M. Popescu, M. Dobriceanu, G. Oprea, "Improving compensation performance in three-phase active power line conditioners by DC-voltage control," *Analele Universităţii "Eftimie Murgu" Reşiţa, Fascicula de Inginerie*, Anul XXI, no. 3, 2014, pp. 167-176.

[8] M. Popescu, A.Bitoleanu, D. Marin, "On the DC-capacitance and control of voltage across the compensating capacitor in three-phase shunt active power filters," *Annals of the University of Craiova, Electrical Engineering Series*, no. 34, 2010, pp. 53-58.

[9] V. M. Moreno, A. P.Lopez, R. I. D. Garcias, "Reference current estimation under distorted line voltage for control of shunt active power filters," *IEEE Trans. Power Electronics*, vol. 19 , issue 4, 2004, pp. 988 – 994.

[10] S. Charles, G. Bhuvaneswari, "Comparison of three phase shunt active power filter algorithms," *International Journal of Computer and Electrical Engineering*, vol. 2, no. 1, Feb., 2010, pp. 175-180.

[11] H. Nalla, H.Djeghloud, "A novel time-domain reference-computation algorithm for shunt active power filters," *ACSE Journal*, vol.6, issue 2, June 2006, pp. 30-40.

[12] A. Bitoleanu, M. Popescu, M. Dobriceanu, F. Nastasoiu, "Analysis of some current decomposition methods: Comparison and case studies," *Revue Roumaine des Sciences Techniques-Serie Electrotechnique et Energetique*, tome 55, issue 1, 2010, pp. 13-22.

[13] A. Bitoleanu, M. Popescu, "Shunt active power filter: Overview on the reference current methods calculation and their implementation," *4th International Symposium on Electrical and Electronics Engineering (ISEEE 2013)*, 11-13 Oct. 2013, Galati, pp. 1-12.

[14] A. Chebabhi et al. "Comparative study of reference currents and DC bus voltage control for three-phase four-wire four-leg SAPF to compensate harmonics and reactive power with 3D SVM," *ISA Transactions* 2015, 57, pp. 360–372.

[15] C. V. Suru, M. Popescu, M. Linca, A. Stanculescu, "Fuzzy logic controller implementation for the compensating capacitor voltage of an indirect current controlled active filter," *2020 International Conference and Exposition on Electrical and Power Engineering (EPE)*, Iasi, Romania, 2020, pp. 039-044.

[16] M. Popescu, A. Preda and V. Suru, "Synchronous reference frame method applied in the indirect current control for active DC Traction substation," *Proc. Annual International Conference on Transportation*, 8-11 June 2015, Athens, Greece.

[17] A. Bitoleanu, M. Popescu, C. V. Suru, "Theoretical and experimental evaluation of the indirect current control in active filtering and regeneration systems," *Proc. Optimization of Electrical & Electronic Equipment (OPTIM) and Aegean Conference on Electrical Machines and Power Electronics (ACEMP)* 2017, May 23-25, 2017, Brasov, Romania, pp. 759-764.

[18] M. Popescu, A. Bitoleanu, V. Suru, "Indirect current control in active DC railway traction substations," *2015 Int. Aegean Conference on Electrical Machines & Power Electronics (ACEMP), 2015 Intl Conference on Optimization of Electrical & Electronic Equipment (OPTIM) & 2015 Intl Symposium on Advanced Electromechanical Motion Systems (ELECTROMOTION)*, Side – Turkey. 2-4 Sept. 2015, pp. 192 - 197.

[19] A. Bitoleanu, M. Popescu, C. V. Suru, "Optimal controllers design in indirect current control system of active DC-traction substation," *The Power Electronics and Motion Control (PEMC)* 2016, Varna, Bulgaria, Sept. 25-30, 2016, pp. 904-909.

[20] M. Popescu, A. Bitoleanu, M. Dobriceanu, M. Lincă, "On the cascade control system tuning for shunt active filters Based on Modulus Optimum criterion," *Proc. of European Conference on Circuit Theory and Design*, August 23-27, 2009, Antalya, Turkey, pp. 137-140.

[21] A. J. J. Rezek et al. "The modulus optimum (MO) method applied to voltage regulation systems: modeling, tuning and implementation," *Proc. International Conf. on Power System Transients*, 24-28 June 2001, Rio de Janeiro, Brazil.

[22] M. Popescu, A. Bitoleanu, C. V.Suru, M. Linca, G. E. Subtirelu, "Adaptive control of DC voltage in three-phase three-wire shunt active power filters systems," *Energies* 2020, 13, 3147.

DOI: 10.52846/AUCEE.2022.10

Application of Electrical Substation, Ring Topology versus Star Topology

Cosmin-Ionuț Toma, Mihaela Popescu, Mihăiță Daniel Constatinescu, Popa Ion Cristian
University of Craiova, Faculty of Electrical Engineering, Craiova, Romania,
ctoma@em.ucv.ro, mpopescu@em.ucv.ro, mconstatinescu@em.ucv.ro, cristip77@yahoo.com

***Abstract* – In order to solve the problem of analyzing network performance of SCADA (Supervisory Control And Data Acquisition) system communication of power grid in effective and practical way, this paper proposes to change the star topology with ring topology, specifically method rapid spanning tree protocol (RSTP), in an electrical substation. The paper discusses about SCADA architecture, main equipment like remote terminal unit, intelligent electronic device, server, server network time protocol, HMI (human machine interface), router and their role in the electrical substation. Also, the levels of the command hierarchy in the SCADA system are discussed. Each level has certain tasks set for the optimization and reliability of the electrical substation. The data flow describes the types of information that are transmitted between hierarchical levels. In the last part the paper the topologies of the system are described.**

Cuvinte cheie: *topologie SCADA, arhitectura SCADA, Rapid spanning tree protocol, topologie stea, flux de informații, stație electrică.topologie inel.*

Keywords: *SCADA topology, SCADA architecture, Rapid spanning tree protocol, star topology, data flow information, electrical substation, ring topology.*

I. INTRODUCTION

SCADA is a technology which provides the ability to collect data from one or more remote equipment and transmit a limited set of control instructions to this equipment. With SCADA it is no longer necessary for an operator to stay or frequently inspect those remote controlled locations if they are working normally.

SCADA includes the operator interface and the handling of concrete application data, but it is not limited to that. Some manufacturers offer software packages that they call SCADA and although these are suitable to operate as parts of a SCADA system, as they provide communication links with other necessary equipment, they are not a complete SCADA system [1].

In [2], the authors presented architecture topologies for substation automation system applications with protection, control, monitoring data flows and their performance requirement.

A modern SCADA system (hardware and software) with specific characteristics for electrical substations is presented in [3].

Communication network is a fundamental element in all electrical substation and network performances can have important role on the control process. The automation using IEC 61850 communication protocol is described in [4], [5], [6].

This paper is organized as follows. Section II presents the SCADA architecture, including the main components. The next section is dedicated to the command hierarchy of in the SCADA system. In section IV, the data flow is introduced. The presentation of the star topology is the subject of section V. It is followed by the presentation of the ring topology. A case study with the implementation of the rapid spanning tree protocol in an electrical substation from Romania is described. Finally, some conclusions are formulated.

II. SCADA ARHITECTURE

Although the equipment components of the entire SCADA system is located in various locations, they are connected as a unified whole, a single system.

As such, the SCADA system concept approach is unitary, not limited to a specific piece of the system.

The SCADA system are presented in Fig. 1 with next components [12]:

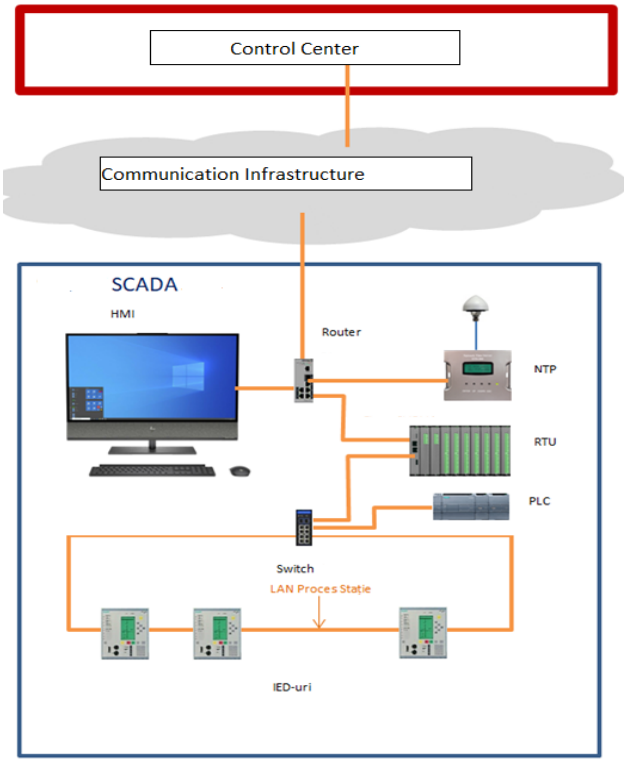

Fig. 1 A typical SCADA system architecture.

- Server
- Router

- Server NTP
- HMI
- Remote Terminal Unit (RTU)
- Intelligent electronic device (IED)
- Control Center
- Communication infrastructure
- PLC

Servers are used in SCADA systems for multi-tasking and real-time database functions. It is responsible for gathering and handing data, providing trends and diagnostic information regarding the operation. Depending on the features, there may also be options to set up predictive maintenance schemes, logistic information and other option [7].

A router which meets the cybersecurity requirements for this type of connection is used for the remote connection to Control Center. The router has a firewall implemented and makes an encrypted VPN tunnel connection to the remote correspondent equipment.

A human-machine interface (HMI) is a user interface that allows the human operator to interact with a system. HMIs are used all over the world in various technologies, ranging from smartphones to power plants.

The HMI running on the SCADA server connects to the SQL database managed by that server.

PLC (Programmable Logic Controller) is still one of the most widely used control system in industry. As the needs to control more devices in the electrical substation, PLCs became distributed and systems became smarter and smaller [8].

To apply the time stamp to all telegrams in the system, a time server is installed which will transmit time signals to the entire system via the network time protocol (NTP). Time stamp resolution applied to all events is 1ms.

The GPS signal will be received by an external antenna, connected with a coaxial cable to the respective time server. This equipment is installed in the SCADA cabinet and is connected to the central system through Ethernet switches. It will provide the necessary NTP telegrams for the synchronization of all SCADA equipment.

Communication infrastructure represents the nodes of a SCADA system which are interconnected through communication buses, constituted in data transmission networks, depending on the surface they cover. The procedures and standard interfaces used are called local networks (LAN- Local Area Network) or networks extended (WAN- Wide Area Network).This equipment related to a certain technological process or a management center that occupies a relatively small area (for example a building or a group of buildings) are interconnected through LANs that use shielded cables with twisted wires as a data transmission medium, coaxial cables or fiber.

The transfer is made through the telecommunications networks based on the generally accepted rules that form the so-called telecommunications protocol. This protocol specifies receiver selection modes, command codes, transmission rates, structure and timing of transmitted messages, etc.

Intelligent electronic device use numerical measurement techniques. Fully digital signal processing provides high measurement accuracy and long-term consistency.

Digital filtering techniques and dynamic stabilization of the measured values ensure the highest degree of security in the determination of protection responses. Device errors are quickly recognized and indicated by integrated self-monitoring [9].

Remote terminal unit is a stand-alone data acquisition and control unit, generally microprocessor based, that monitors and controls equipment at a remote location. Its primary task is to control and acquire data from process equipment at the remote location and to transfer this data back to a central station. It generally also has the facility for having its configuration and control programs dynamically downloaded from some central station.

The Control Centre is the dispatcher's work point for operating SCADA system.

III. Command Hierarchy of in the SCADA System

The command to the primary equipment can be initiated from multiple locations such as local panel, BCU/BCPU, HMI station, control center, depending on the position chosen for the LOCAL/REMOTE switch. The command hierarchy of primary switching equipment can be illustrated by means of Fig. 2 [12].

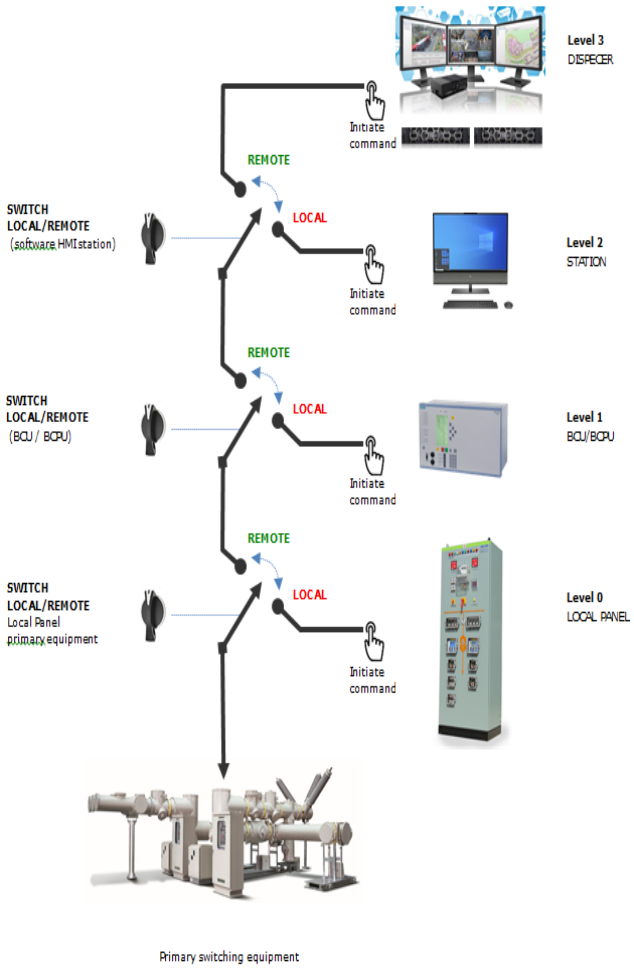

Fig. 2 Hierarchy of command in the SCADA system.

The interconnection between the components of the SCADA system is subject to a philosophy based on four hierarchical levels of the SCADA architecture.

Monitoring of states, measures, alarms will be able to be found and accessed at any of the four levels mentioned.

Also, the commands of the switching equipment is done independently, but not simultaneously from the four levels:

• Level 0 – PROCESS;
• Level 1 – FEEDER – through the BCUs or BCPUs installed in each high voltage or medium voltage;
• Level 2 – STATION – from the operator interface (HMI) installed in the station;
• Level 3 – CONTROL CENTER – from the SCADA dispatcher system – via a remote connection.

The selection between hierarchical levels is made by using the Local/Remote switches (physical or software) provided for this purpose. Besides the three command levels, in order to illustrate the system philosophy, we consider level 0 as the technological process level, i.e. the primary equipment [3].

- Level 0 – PROCESS

At this level, there is the equipment that directly participates in the production, transport and distribution of electricity, forming the group of primary equipment (separators, switches, current transformers, voltage transformers, etc.).

- Level 1 – FEEDER

This level includes all the digital devices intended to ensure the signaling of alarms and measures from the process equipment, the implementations of the protection functions as well as the control of these equipment where appropriate. In this level, there are different types of digital relays (IEDs) that have specific inputs/outputs/analog for voltage, current, signaling, alarms, protection functions and controls, as needed.

- Level 2 – STATION

At this level, the station RTU collects all the signals from station via the communication network (LAN Process).

Also, through the same LAN, the process can be received for the primary equipment from hierarchical levels higher than the feeder equipment BCU or BCPU respectively HMI station or Control Center.

- Level 3 – Control Center

At the level of the dispatcher, there is the Control Center SCADA system interconnected with the Station SCADA system.

IV. The Data Flow

In the SCADA system, the information is transmitted on several flows, in a predetermined way, making possible analysis or diagnosis easy. There are three information flows:

• monitoring information – the signals from the process (signals, alarms, etc.). This information is the most numerous and is transmitted from the process to the Control Center – respectively from level 0 to level 3.

• control information – command signals. This information is less and is transmitted from the operating interface (HMI, Control Center, Station or IED) to the process – that is, from level 3 (or 2, or even 1) to level 0.

• GOOSE type information – the signals are transmitted directly (within the Process LAN) from one IED to another. As a rule, certain information necessary for the interlocking logic is transmitted through this information.

V. Star Topology

Star networks, presented in Fig. 3, are well known for their nodes being located in a shape of a star. There are one of the most commonly network topologies. The way such networks look reminds of a star as there is a central node which is illustrated in the very middle of the network schematics and from this central hub there are other nodes all around this hub connected to it. The central hub is there to transmit the messages to the other nodes and it is the server itself when the peripheral nodes are the clients [8].

The main function of the hub is to control and message all of the functions of the network. It can also be in charge for repeating the data flow. Such configuration can be made with use of the twisted pair cable as well as the optical fiber cable. A coaxial cable can also be used.

The reason of using the star topology is to reduce the impact of a failure for a line in a way of connecting all existing systems to one central node or hub. All of the peripheral, but central nodes can be connected with each other only through the very central node which is the hub in the middle of the star topology drawing.

They all transmit and receive data only in a way of using the central node, there is no other way of their communication.

If there is a fault in a transmission line connecting any of the peripheral nodes to the very central node, it will lead to a result of the isolation of that peripheral node from all other nodes. In this case, all of the rest of the systems will not be affected.

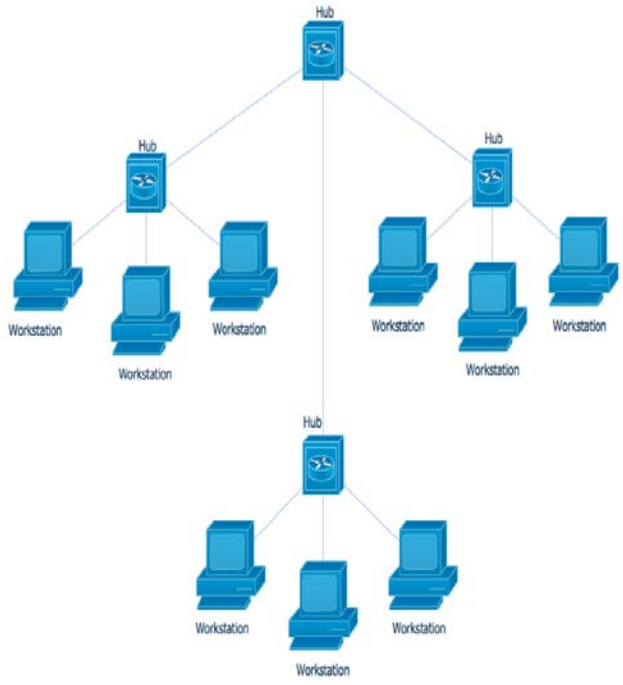

Fig. 3 Star topology.

Extended star is a type of network topology, where a network, based upon the physical star topology, has one or

more repeaters between the central nodes, which also can be called the “hub” of the “star”.

In this network topology, the peripheral or so called “spoke” nodes, the repeaters, are being used for extending the maximum transmission distance of the point-to-point links between the central node and the peripheral nodes.

If these repeaters are replaced with hubs or switches, then so called hybrid network topology is created.

Distributed star is a commonly used type of network topology that has individual networks based on the physical star topology and connected in a linear fashion with no central or top level connection point [10].

VI. RING TOPOLOGY

The protection and control system in modern substations is becoming more and more digital: therefore the performance of the protection and control system depends on successful communication of data between devices.

This requires that the communications network is highly reliable and highly available.

Just as with the protection and control system, the communications network needs to eliminate single points of failure.

Bypassing or accounting for the failure of a network element should introduce as short a time delay in message transmission and reception as possible, with zero delay ideal.

The traditional network method for availability, presented in Fig. 4, is to use a ring topology, so any network node has two paths to communicate around the network [13].

Network switches are connected to create a physical ring. Networks are composed of Ethernet switches that use a store and forward method to pass data, forming a virtual connection between switch ports.

Ethernet switching does not permit a virtual connection that forms a complete ring, so there are always specific ports on switches configured to be virtually open.

These specific “open” ports therefore won’t forward any data. This means for any data transmission there is a normal point-to-point path through the network.

On the failure of a network link in this point-to-point path, the network will reconfigure to a new point-to-point path through the network by closing virtually open ports as appropriate [11].

Rapid Spanning Tree Protocol is a ring topology communication method.

The basic protocol behind this is Spanning Tree Protocol (STP) as defined by IEEE 802.1D.

Network reconfiguration time using STP may take minutes. IEE 802.1w (2) defines Rapid Spanning Tree Protocol (RSTP), which speeds up reconfiguration time to seconds.

Continuous supervision of power equipment/machinery is provided by SCADA systems implemented in the power systems and which are computer-based tools, using power dispatchers to assist them in controlling the operation of complex power systems [11].

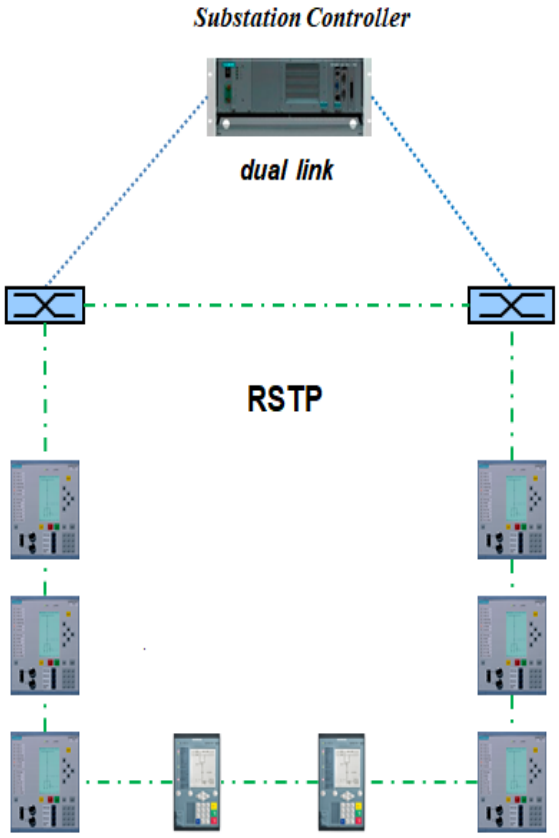

Fig. 4: Ring topology.

Fig. 5 is associated to a case study in an electrical substation from Romania. It presents a screen capture in real-time with ring topology.

It is shown how it works when there is one single fault in the communication system.

In the electrical substation, if any device is fault, the ring topology operates normal, without problems, but with star topology, the electrical substation can’t be operated (if the central workstation is unavailable). This is one of the main advantages of the ring topology.

In Fig. 5, the blue line means the link is good and the telegrams go to each device (switch, bay control unit, bay control protection unit).

The white line indicates that the link is broken between devices and one of these is faulty.

Such a situation is illustrated in the Fig. 5, where the unavailable device is red and the communication is failed. In this case, the telegrams change the direction communication with the rest of available devices.

Another situation is where the bay control unit is red in the 20 kV station, but the line is blue (communication is ok). In this case, the device was removed physically and the optical fiber was extended to the next device.

The reason for the red device is that this one was not deleted by software from the graphical interface.

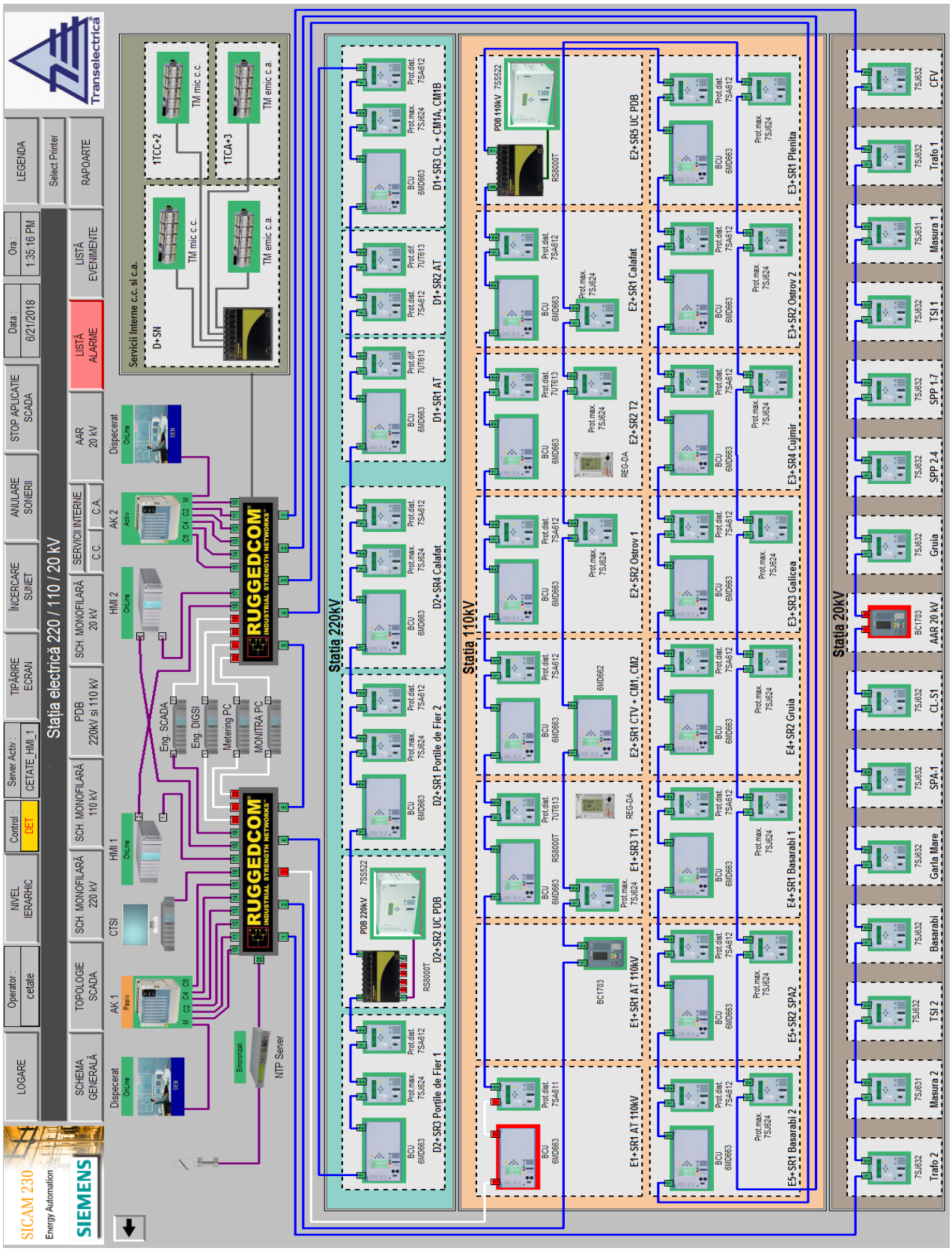

Fig. 5 RSTP implemented in an electrical substation.

VII. CONCLUSIONS

This paper shows that, by replacing the star topology with ring topology using the rapid spanning tree protocol in a SCADA system, there are many advantages.

By means of a case study in an electrical substation from Romania, the proper real-time operation of the system is illustrated when there is a fault in the communication system.

The availability of the system is higher using the ring topology than the star topology, and the fundamental function of a SCADA system to guarantee and remotely control the installations and power networks in order to ensure its maintenance and reliability is achieved.

ACKNOWLEDGMENT

Source of research funding in this article: Research program of the Electrical Engineering Department financed by the University of Craiova.

Contribution of authors:
First author – 25%
First coauthor – 25%
Second coauthor – 25%
Third coauthor –25%

Received on July 28, 2022
Editorial Approval on November 22, 2022

REFERENCES

[1] V. Ivanov, *SCADA-Control Supervizor si Achiziții de Date*, Craiova, Romania, 2001.

[2] J.-C. TAN, W. Luan, "IEC 61850 Based substation automation system architecture design," *IEEE Power and Energy Society General Meeting*, Detroit, MI, USA, July 2011.

[3] V.-C. Georgescu, "Optimized SCADA Systems for Electrical Substations," *the 8th International Symposium on Advanced Topics in Electrical Engineering*, București, Romania, 2013.

[4] S. Roostaee, R. Hooshmand, M. Ataei, "Substation automation system using IEC 61850," *5th International Power Engineering and Optimization Conference*, Shah Alam, Malaysia, 2011.

[5] C. Hoga, G. Wong, "IEC 61850: open communication in practice in substations," *IEEE PES Power Systems Conference and Exposition*, New York, USA 2004.

[6] C. Brunner, "IEC 61850 for power system communication," *IEEE/PES Transmission and Distribution Conference and Exposition*, Chicago, IL, USA, 2008.

[7] https://info.panelshop.com/blog/how-do-scada-systems-work

[8] https://www.conceptdraw.com/How-To-Guide/star-network-topology

[9] C. Gordon, D. Reynders, E. Wright "*Practical Modern Protocols*,", Newness,,pp 10-30, ,2004.

[10] https://www.conceptdraw.com/How-To-Guide/star-network-topology

[11] R. Hunt, B. Popescu, "Comparison of PRP and HSR Networks for Protection and Control Applications," *Western Protective Relay Conference*, Washington, USA, 2015.

[12] Descriere funcțională a unui sistem SCADA, Mihai Enache, Exstart s.a.

[13] Network Redundancy in Substation Automation, Siemens AG all rights reserved, 2012.

DOI: 10.52846/AUCEE.2022.11

Analyzing the Influence of Harmonic Parameters on Accuracy Indices When Applying Wavelet Transform

Dusan Kostic*, Ileana Diana Nicolae†, Iurie Nuca*, Petre Marian Nicolae*

* Univ. of Craiova, Dept. of Electr. Eng., Aeronautics and Energetics, dusan.v.kostic@gmail.com, nuca.iurie@gmail.com, npetremarian@yahoo.com

† Univ. of Craiova, Dept. of Computer Science and Information Technology, ileana_nicolae@hotmail.com

Craiova, Romania

***Abstract* - The paper deals with the evaluation of root mean square deviations and maximum absolute relative errors associated to the decomposition followed by recomposition based on Wavelet Packet Transform (WPT) of signals polluted with harmonics. Subtrees associated to sets of harmonics presenting practical interest for industrial applications are addressed. The study uses artificial signals generated through the superposition of perfect sinusoids with pairs of harmonics which proved to be related in an almost exclusive manner to pairs of nodes from the bottom level of a WPT tree. 4 parameters had to be considered when determining the maximum and minimum values of errors for each set: the clustered harmonics' magnitudes and their phase-shifts relative to the component of fundamental frequency. The decomposition/recomposition are time-efficient due to an original system of flags labeling each node from the WPT tree. For each analyzed set of harmonics, 3d graphical representation of minimum and maximum errors along with the associated 3d graphical representation of the phase-shifts are provided. At the same time, per set limits of errors ranges were established and discussed while specific patterns were deduced for the context in which extreme errors appear (phase-shifts and harmonic magnitudes). The results were commented, and conclusions were drawn.**

Cuvinte cheie: *calitatea puterii, analiză Wavelet cu arbori binari, estimarea erorilor. analiza asistata de calculator.*

Keywords: *power quality, wavelet analysis with binary trees, errors estimation, computer aided analysis.*

I. Introduction

Defining the best signal analysis method is a never-ending battle. Each of the methods has its own virtues and flaws which make their applicability limited to certain cases. Fast Fourier Transform (FFT) is a very popular method because it gives full harmonic spectrum, has a short runtime, and has low computational effort. But this method is more precise when analyzing signals that have stationary nature. Because FFT assumes the asymmetry between half-periods of a signal, it shows poor results when computing signals of non-stationary nature.

Short-Time Fourier Transform (STFT) is another popular and fast method that uses a window for diving a signal into smaller parts, thus making the analysis more precise. On the other hand, the window length is fixed so the resolution will be constant for all frequencies. Therefore the analysis with STFT will provide good results for either low-frequency (LF) or high-frequency (HF) spectrum, but not for both.

Wigner-Ville Distribution (WVD) and Pseudo-WVD are methods that are both bilinear in nature and artificial cross terms appear in the decomposition results rendering the feature interpretation problematic.

For all the above-mentioned methods the common flaw is that they are non-reversible [1]. Many of these problems can be solved using Wavelet transform (WT). Wavelet transform is considered to be a significant breakthrough in mathematical analysis. It can be applied to various fields. For example, signal processing, image processing, pattern recognition, speech analysis and many applications could introduce wavelet analysis [2]. It is a timescale transform that uses a variable-length window so it provides good resolution for both LF and HF spectrum, while preserving both time and frequency information. The authors have previously studied a specific type of WT called Wavelet Packet Transform (WPT) that was proposed in 1992 [3]. WPT provides full harmonic spectrum but suffers from decimation phenomenon [4]-[7]. Detailed analysis of wavelet binary tree shown the best parameters (number of levels, wavelet mother, filter length) when applying WT.

The authors extensively studied a specific case of a wavelet tree with seven levels (T7) that uses a wavelet mother from Daubechies family and filter length of 28 ("db14") [6]. One of the important conclusions was that nodes from the bottom level of the wavelet tree exhibits cluster patterns [7]-[10]. This means that nodes can be grouped in clusters of 2, 4 or 8 nodes where each group is affected by 2, 4 and 8 harmonics respectively.

II. Nodes-Harmonics Pairing Patterns and Run-time Saving Decompositions and recompositions Relying on WPT Tress

The Wavelet binary tree (T7) used in this paper was tested in many different operational contexts [6…9]. It has the following characteristics: 7 levels of decomposition, Daubechies wavelet mother with filters of 28 components (called "db14" in Matlab) and 512 components in the signal hosted by the root node.

The artificial test signals used for the decomposition/recomposition relying on T7 were generated by

TABLE I.
CHARACTERISTICS OF HARMONIC MAGNITUDES USED FOR ANALYSIS

Parameters for harmonic magnitudes variation	Harmonic order			
	3	5	7	≥9
Step [%]	2	1	1	0.5
Max [%]	20	10	10	5

superposing a perfect sinusoid with the maxim magnitude of 800 and frequency of 50 Hz with 2 harmonic signals, characterized by their harmonic orders (H1 and H2), magnitudes (M1 and M2) and phase-shifts (phi1 and phi2).

phi1 and phi2 were cycled within the range [-π,π] with the step π/6 whilst M1 and M2 were cycled considering 11 equidistant values such as to cover ranges from 0 to the maximum value (weight from the perfect sinusoid magnitude) as mentioned in Table I.

Clustering properties of T7 trees [8] allowed the authors to reconstruct certain harmonic components associated to clustered harmonics polluting the decomposed signal. The goal is to isolate only certain clusters of harmonics that affect the associated clustered of nodes in an almost exclusive manner [10] and to analyze how those clusters affect the accuracy of wavelet decomposition (WD) and recomposition by varying their phase shifts and magnitudes. Table II shows the 4 sets of harmonic orders (HO) that were used for this analysis as well as the nodes that were affected by those sets of harmonics. The dominant harmonics and nodes [7] are represented with bold fonts.

The WPT recomposition was made in the following way [7]:

- Only the first 32 "terminal nodes" (nodes from the 7-th level) were considered because only the nodes from that range are affected by HOs from the studied sets;

- Those nodes were associated with flags whose values are 0 or 1 whether the nodes were affected by the specific HO or not, respectively;

- In case the terminal node has a value of 1 for a certain set of HOs it is considered in the decomposition, and opposite in case it has 0;

- Flags were given to the nodes from the other levels in upwards direction of the wavelet tree depending on the flags of the nodes in the adjacent lower level. For example, if in level j:

  - Both nodes 2 X (k-1) and 2 X k have a value 1, then the node k from level j-1 that decomposes into nodes 2 X (k-1) and 2 X k in level 7 will have a flag value of 3 - full decomposition;
  - Node 2 X (k-1) has a value of 1 and node 2 X k has a value of 0, then the flag value is 2 - left decomposition;
  - Node 2 X (k-1) has a value of 0 and node 2 X k has a value of 1, then the flag value is 1 - right decomposition;
  - Both nodes 2 X (k-1) and 2 X k have a value of 0, then there will be no decomposition.

TABLE II.
PROPERTIES OF ANALYZED CLUSTERS OF NODES AND HARMONICS

Properties	Set ID			
	1	2	3	4
Harmonic orders	**3**,5	**7**,9	**15**,17	31,**33**
Nodes	**2**,4	**3**,7	**5**,13	9,**25**
Weight of dominant harmonic energy in the dominant node energy	0.9824	0.8487	0.6964	0.6012

During recompositions a similar technique (flags and simplified recomposition functions) was successfully used to save runtime.

The goal of the decomposition/recomposition is to inspect spectral leakages. In other words, even though the WD revealed clustering pattern of nodes that contain certain HOs, not all the weights of harmonics are distributed between those clusters. The analysis will reveal how much do parameters of HOs affect the spectral leakages and to determine for which parameters does WD perform the best or the worst.

The difference D between the synthetically generated harmonic signal *yh* and the harmonic signal (*yhr*) obtained through WPT recomposition was computed for every set and every combination of the 4 parameters (harmonic weights and phase-shifts). Afterward maximum absolute relative percentage errors (MAR) were computed as: *max(abs(D))*/*max(abs(yh))**100.

Another index of accuracy that was used was the Root Mean Square Deviation (RMSd) , computed with the formula:

$$RMSd = \sqrt{\frac{\sum_{i=1}^{512}(yh_i - yhr_i)^2}{512}} \quad (1)$$

In the following sections the phase-shifts may be expressed as IDs (e.g. 1 for - π, 2 for - π + π/6 a.s.o.). Also, the harmonic magnitudes may be expressed as IDs (e.g. 1 for M1=0, 2 for M1=step, …, 11 for the maximum value of M1), according to Table I.

Examples of artificial signals, results of decomposition/recomposition and curves of differences (that are actually instantaneous errors) obtained as *yh*-*yhr*, are depicted by Figs. 1 and 2.

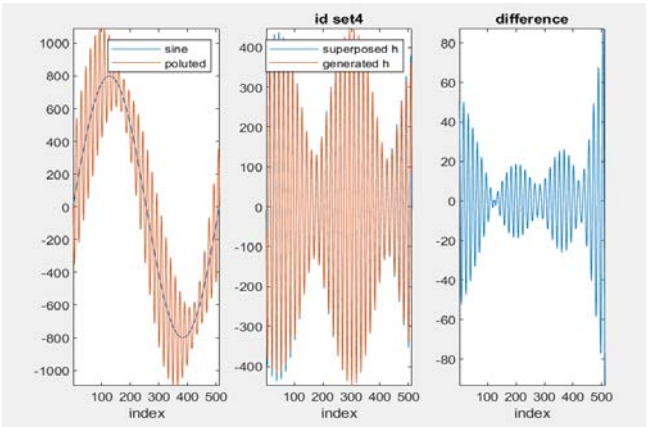

Fig. 1. Example of polluted signal before decomposition (left), harmonic signals before and after recomposition (middle) and the difference between the initial and recovered harmonic signals (right) for the 4-th set.

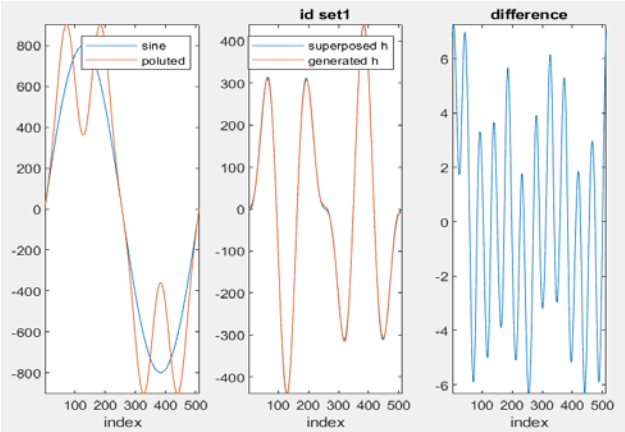

Fig. 2. Example of polluted signal before decomposition (left), harmonic signals before and after recomposition (middle) and the difference between the initial and recovered harmonic signals (right) for the 1-st set.

III. Study of Root Mean Square Deviations

The minimum and maximum values of RMSd were computed, graphically represented and interpreted for each of the 4 sets of 2 harmonics. Surfaces (S1 and S2) were built considering on the horizontal axis Ox the 11 values of the dominant harmonic magnitudes (M1) and on Oy the 11 values of the paired harmonic magnitudes (M2). M1 was allways associated to the dominant harmonic. S1 corresponds to minimum values whilst S2 corresponds to maximum values of RMSd, the difference between the same (x,y) values from them being provided by different phase-shifts phi1 and phi2.

The phase shifts corresponding to S1 and S2 were als represented and interpreted.

A. *Study of extreme values of RMSd*

When none of the paired harmonics is polluting the test signal, constant values were obtained for RMSd , as follows: 1.7 for the 1-st set, 0.65 for the 2-nd, 0.27 for the 3-rd and 0.13 for the 4-th set respectively. These values correspond to residual errors, are specific to the non-ideal feature of the wavelet filter and are highly acceptable as related to the maximum value of the fundamental component (they represent at most 0.2% from it).

The values computed for RMSd when only the dominant harmonic is 0 whilst its pair in the set is non-zero revealed the influence of phase-shifts. Table III gathers the extreme values on each surface of extreme values.

Table IV gathers the counterpart of the data from Table III, but for the case when only the dominant harmonic within the analyzed sets is non-zero . The influence of phase-shifts was revealed again.

Table III.
Extreme Values of RMSd when the Dominant Harmonic is Zero and the Secondary Harmonic is non-Zero

Set ID	Minimum RMSd		Maximum RMSd	
	S1	S2	S1	S2
1	1.708	1.71	2.33	2.43
2	0.6567	0.6584	0.86	0.99
3	0.28	0.3	0.9	1.33
4	0.21	0.26	1.71	2.27

Table IV.
Extreme Values of RMSd when the Dominant Harmonic is non-Zero and the Secondary Harmonic is Zero

Set ID	Minimum RMSd		Maximum RMSd	
	S1	S2	S1	S2
1	1.7027	1.7028	1.88	1.9
2	0.66	0.68	0.98	1.8
3	0.27	0.33	0.79	2.02
4	0.22	0.3	1.76	2.67

For both Tables III and IV, the indices of magnitudes within the analyzed set of harmonics were as follows: 2 for the minimum values and 11 for the maximum values. Therefore one can conclude that when a single harmonic from an analyzed set is non-zero, the RMSd is increasing with the value of that harmonic magnitude.

The extreme values reached by RMSd when both harmonics within the analyzed sets were non-zero are gathered by Table V.

The minimum values for the RMSd were reached for all sets for the combination of indices associated to harmonic magnitudes equal to (2,2) within each set. It means that the lowest values for RMSd in this case are associated to the lowest non-zero magnitudes of paired harmonics.

As for the maximum values for the RMSd, two possible combinations of indices associated to harmonic magnitudes were identified. The 1-st combination, corresponding to values marked with star is (11,2) and its meaning is „highest magnitude for the dominant harmonic combined with lowest magnitude for the paired harmonic order". The 2-nd one is (11,11) and it means „highest magnitudes for both harmonic orders".

The maximum RMSd as compared to the highest value of the harmonic magnitude (11-th from the set) is equal to 5.72% and is recorded for the 4-th set, which is known as having the worst filtering propertie of all sets (lowest weight of energy in the dominant node). Again one can consider that highly acceptable errors are generated by the analyzed original algorithm.

B. *Study of phase-shifts associated to extreme values of RMSd*

Table VI gathers the values of phi1 and phi2 associated to the cases when one of the harmonics in the set is zero (when the associated harmonic of a phase-shift was zero, the symbol „-" was used).

The analysis of these results revealed that:

- identical values but with oppposite signs were obtained for the sets with IDs 1 and 4;
- at the second set, 2 identical values but with oppposite signs can appear for S1 for different phase-shifts;
- at the 3-rd set, the differences (S1 vs S2) between the counterpart phase-shifts are always $\pi/2$.

Table V.
Extreme Values For RMSd When Both Harmonics Are Non-Zero

Set ID	Minimum RMSd		Maximum RMSd	
	S1	S2	S1	S2
1	1.708	1.7115	2.34	2.76
2	0.66	0.68	0.98*	1.8
3	0.27	0.33	0.79*	2.02
4	0.16	0.47	1.62*	4.58

TABLE VI.
VALUES OF PHASE-SHIFTS ASSOCIATED TO EXTREME VALUES OF RMSD WHEN ONLY ONE OF THE PAIRED HARMONICS IS ZERO

Set ID	Condition	phi1		phi2	
		S1	S2	S1	S2
1	M1=0	-	-	- π/2	0
	M2=0	- π/2	0	-	-
2	M1=0	-	-	- π or π	- π
	M2=0	- π or π	- π/2	-	-
3	M1=0	-	-	–2π/3	- π/6
	M2=0	5 π/6	π/3	-	-
4	M1=0	-	-	π/2	0
	M2=0	π/2	0	-	-

A more detailed study was needed for the case when both harmonic orders are non-zero and its results are presented below.

1) First set

Fig. 3 depicts S1 (left), S2 (middle) and S1-S2 (rigth) for the 1-st set.

Fig. 4 depicts the associated phase-shifts for S1 (top) and S2 (bottom) . Left – phi1, middle – phi2 and right , phi1-phi2 for the 1-st set.

phi1 for S1 is usually equal to 2 when M1>=M2, with few exceptions and 3 otherwise. A sort of separation „above and below" the main diagonal of the matrix in which the magnitudes of dominant harmonic determine the raws and those of the paired harmonic determine the columns can be noticed, as in Table VII.

Phi2 for S1 is usually equal to 8 below the main diagonal (M1>M2) , equal to 9 on the main diagonal of the matrix similar to that from Table VII or in its strict vicinity and is 10 over the main diagonal , with few exceptions.

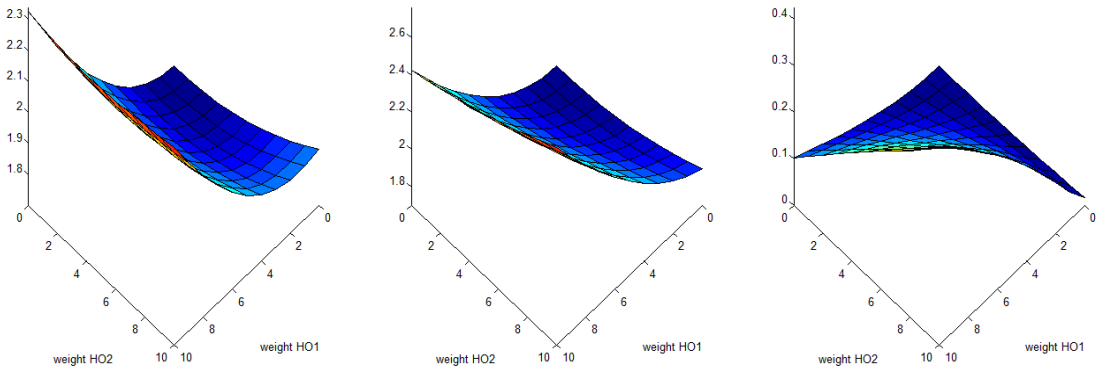

Fig. 3 RMSd deviation of S1 (left), S2 (middle) and S1-S2 (rigth) for the 1-st set.

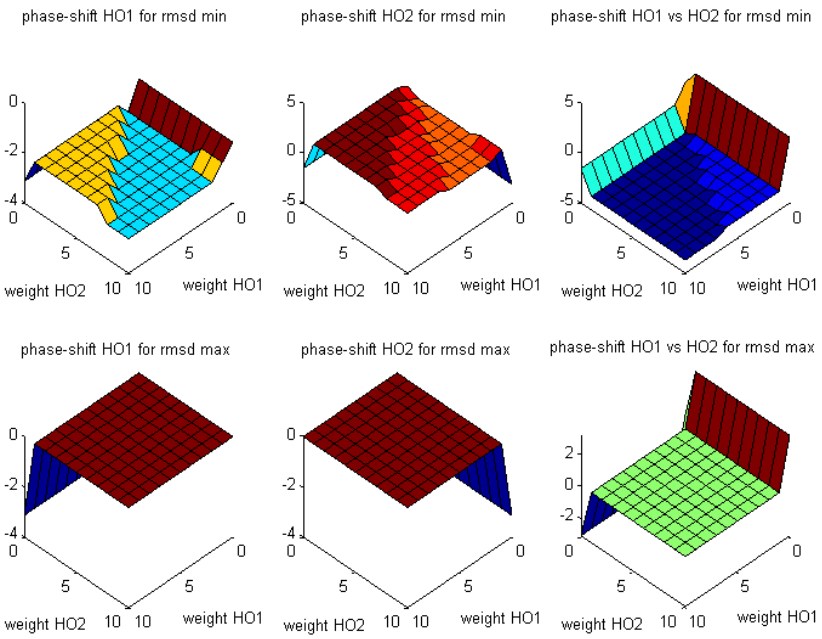

Fig. 4. Associated phase-shifts for S1 (top) and S2 (bottom) . Left – phi1, middle phi2 and right , phi1-phi2. 1-st set.

TABLE VII.
IDENTIFIERS OF PHI1 FOR S1, 1-ST SET

Dominant harmonic / Secondary harmonic	1	2	3	4	5	6	7	8	9	10	11
1	1	1	1	1	1	1	1	1	1	1	1
2	4	2	3	3	3	3	3	3	3	3	3
3	4	2	2	3	3	3	3	3	3	3	3
4	4	2	2	2	3	3	3	3	3	3	3
5	4	2	2	2	2	2	3	3	3	3	3
6	4	2	2	2	2	2	2	3	3	3	3
7	4	2	2	2	2	2	2	2	3	3	3
8	4	2	2	2	2	2	2	2	2	3	3
9	4	3	2	2	2	2	2	2	2	2	2
10	4	3	2	2	2	2	2	2	2	2	2
11	4	3	2	2	2	2	2	2	2	2	2

As for the difference (phi1-phi2) associated to S1, only 2 values were noticed: 1 below the main diagonal and -1 (corresponding to the value - π - π /6) over it.

Usually when M1>M2, the phase-shift between H1 and H2 (phi1-phi2) is - π - π /6 and otherwise is - π + π /6.

Both phase-shifts had the value 7 over all S2 and therefore (ph1-phi2) is always 0.

2) ***Second set***

Fig. 5 depicts the S1, S2 and S1-S2 surfaces whilst Fig. 6 depicts the corresponding surfaces with phase-shifts for the 2-nd set.

For S1, phi1 is usually 7 above the main diagonal (fewer values) and 1 or 13 nearby and below it. On the contrary, phi1 is usually 7 below and nearby the main diagonal and 1 or 13 above it (fewer values).

It is why (phi1-phi2) is mapped either in - π or in π for S1.

Both phase-shifts had the value 4 over all S2 and therefore the phase-shift (ph1-phi2) is allways 0.

3) ***Third set***

Fig. 7 depicts the S1, S2 and S1-S2 surfaces whilst Fig. 8 depicts the corresponding surfaces with phase-shifts for the 3-rd set.

phi1 for S1 can take 3 values: 9 above the main diagonal, 11 on it and close to it and 12 below it.

phi2 for S1 can take 3 values: 3 above the main diagonal, 4 on it and close to it and 6 below it.

Under these circumstances, most of the values of (phi1-phi2) for S1 are equal to π and a small number of them is π + π /6 .

For S2, phi1 takes the value 6 over the main diagonal, more values 7 nearby it, one value 8 near the main diagonal and close to it and few values 9 under the main diagonal.

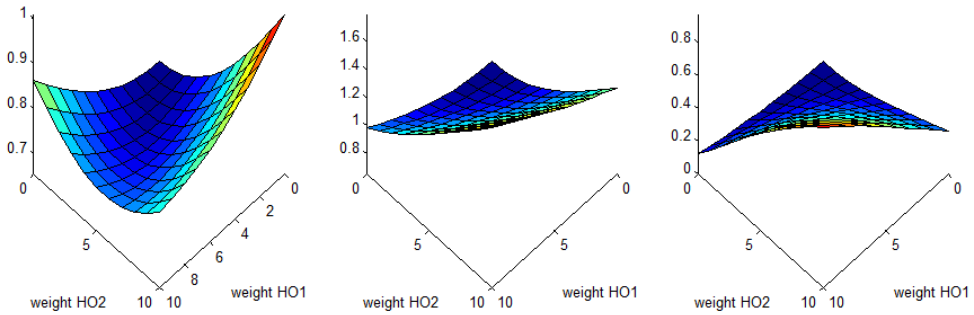

Fig. 5. RMSd deviation of S1 (left), S2 (middle) and S1-S2 (rigth) for the 2-nd set.

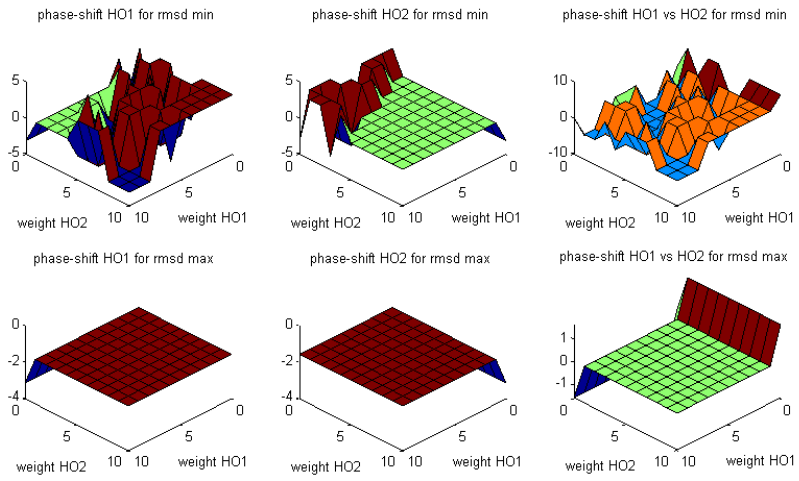

Fig. 6. Associated phase-shifts for S1 for RMSd. (top) and S2 (bottom) . Left – phi1, middle phi2 and right , phi1-phi2. 2-nd set.

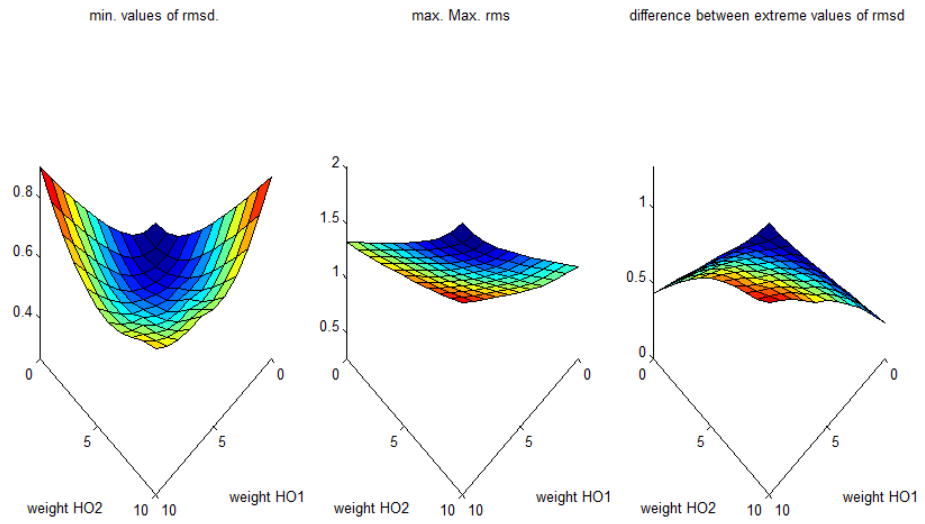

Fig. 7. RMSd deviation of S1 (left), S2 (middle) and S1-S2 (rigth) for the 3-rd set.

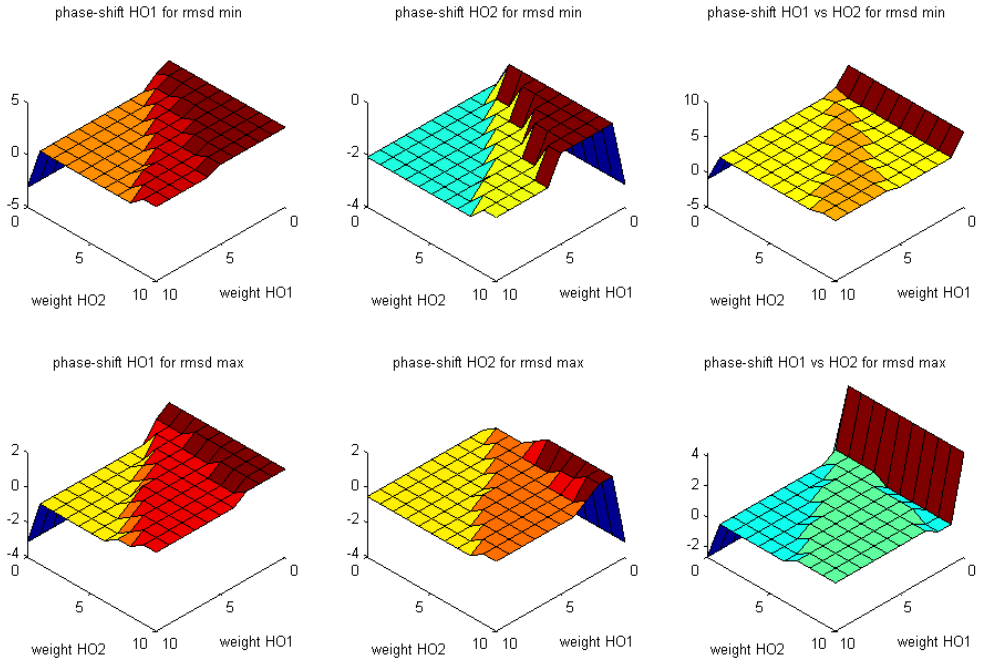

Fig. 8. Associated phase-shifts for RMSd. S1 (top) and S2 (bottom) . Left – phi1, middle phi2 and right , phi1-phi2. 3-rd set.

diagonal, 7 on it and nearby it, 4 values 8 for high values of M1 and small values of M2 and few values of 9 nearby the main diagonal, under it for high values of M1.

Accordingly, (phi1-phi2) for S2 has many values of 0 far from the main diagonal and the remaining ones are associated to the index 8 (which is associated to $\pi/6$).

4) ***Fourth Set***

Fig. 9 depicts the S1, S2 and S1-S2 surfaces whilst Fig. 10 depicts the corresponding surfaces with phase-shifts. For S1, phi1 can take 3 values: 4 above the main diagonal, many values of 10 and only few values of 11 under the main diagonal. For S1, phi2 can take 3 values: 10 above the main diagonal, many values of 4 and only few values of 5 under the main diagonal.

Therefore phi1- phi2 can take only 2 values: - π above the main diagonal and π under it.

For S2, phi1 and phi2 have all values equal to 7 and therefore (phi1-phi2) is 0.

IV. Study of Maximum Absolute Relative Errors

The variation of MAR with harmonic magnitudes and phase-shifts is approached in this section.

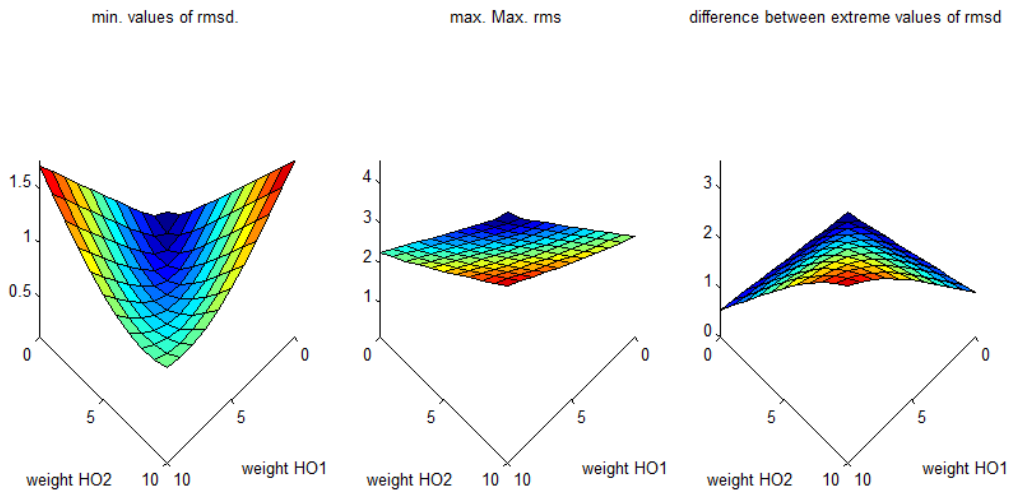

Fig. 9. RMSd deviation of S1 (left), S2 (middle) and S1-S2 (rigth) for the 4-th set.

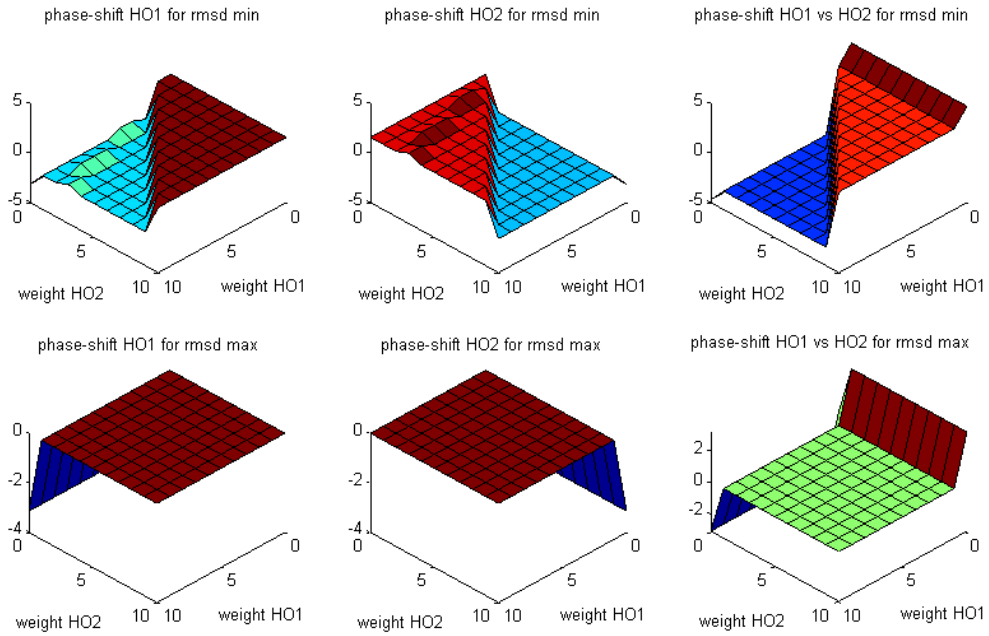

Fig. 10. Associated phase-shifts for RMSd. S1 (top) and S2 (bottom) . Left – phi1, middle phi2 and right , phi1-phi2. 4-th set.

Figs 11...14 depict the surfaces with extreme values of MAR for each of the analyzed sets, following the same rule applied in the previous section. Left – surface S1 with minimum values, middle – surface S2 with maximum values and right – difference between S1 and S2.

The extreme situations (when one of the harmonic from set is 0) were analyzed for MAR as well. In this aim, Table VIII gathers the extreme values for MAR when only the dominant harmonic is 0. In Table VIII, all minimum values were found to be associated to the maximum magnitude of the secondary harmonic, except for the value 17.87% computed for the 4-th set, S1, which is associated to the harmonic with ID 4, despite an usual „descending" trend of the rest of values observed toward the maximum magnitude of the 2nd harmonic.

On the other hand, the maximum values were found to be associated to the minimum magnitude. It means that a sort of „reversed dependence" is established in this case between the values of MAR and harmonic magnitudes.

TABLE VIII.
EXTREME VALUES FOR MAR WHEN ONLY THE DOMINANT HARMONIC IS 0

Set ID	Minimum MAR [%]		Maximum MAR [%]	
	S1	S2	S1	S2
1	6.85	9.43	50.44	52.55
2	7.79	11.02	48.27	55
3	9.69	14.41	18.53	27.82
4	17.87	22.51	19.96	27.36

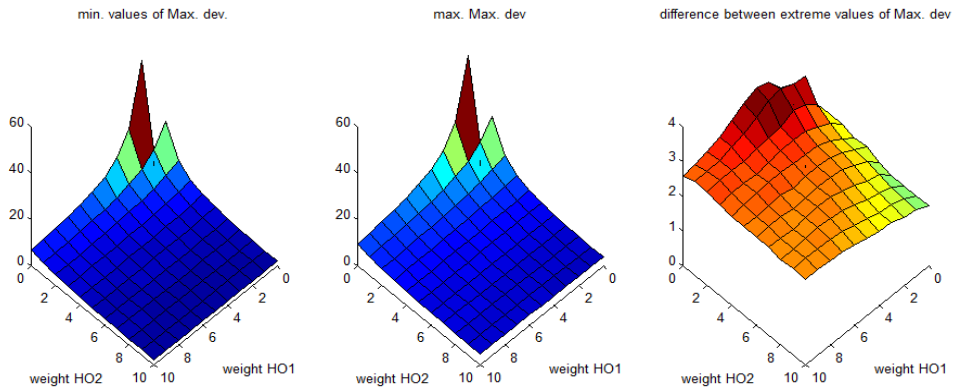

Fig. 11. Surfaces with extreme values of MAR for the 1st set. S1-left, S2- middle, S1-S2 – right.

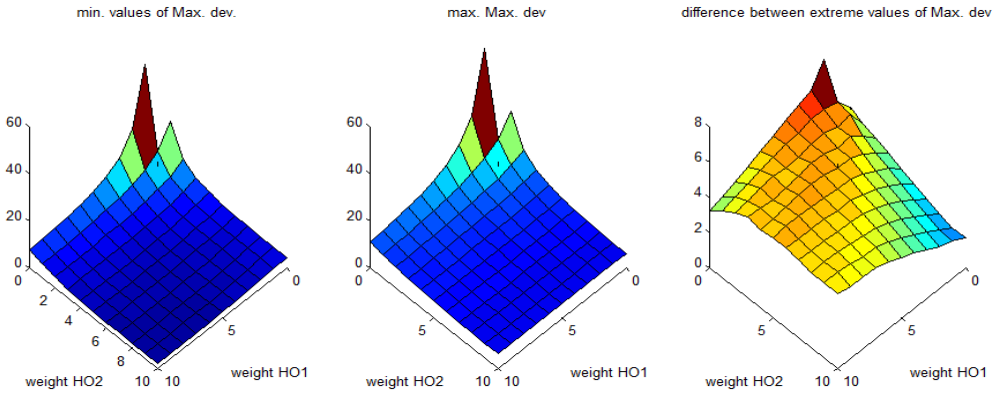

Fig. 12. Surfaces with extreme values of MAR for the 2nd set. S1-left, S2- middle, S1-S2 – right.

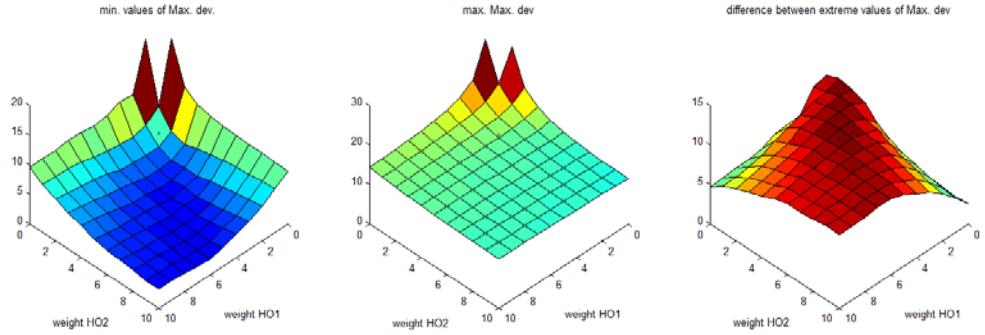

Fig. 13. Surfaces with extreme values of MAR for the 3rd set. S1-left, S2- middle, S1-S2 – right.

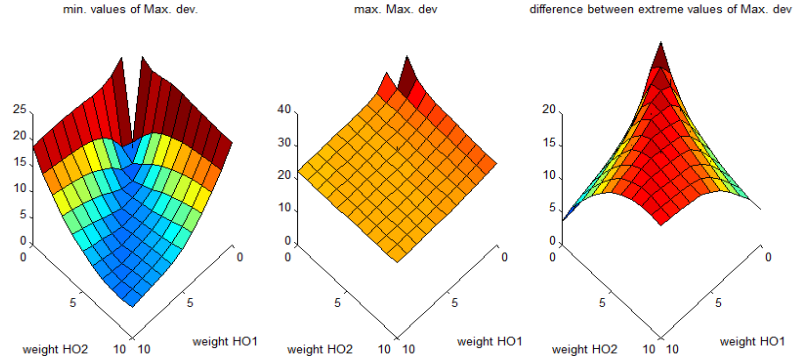

Fig. 14. Surfaces with extreme values of MAR for the 4th set. S1-left, S2- middle, S1-S2 – right.

TABLE IX.
EXTREME VALUES FOR MAR WHEN ONLY THE DOMINANT HARMONIC IS NON-ZERO

Set ID	Minimum MAR [%]		Maximum MAR [%]	
	S1	S2	S1	S2
1	2.22	3.94	24.24	26.34
2	4.56	6.25	24.28	28.31
3	8.99	11.57	18.6	25.9
4	19.27	25	20.26	32.5

One can also notice smaller differences between the extreme values of sets with higher IDs (e.g. the difference between the minimum and maximum values of the 1-st set is higher than 46%, whilst its counterpart for the 4-th set is 13%). Actually the MARs associated to the smallest harmonic magnitudes correspond to small absolute values and therefore cannot be considered as significant in these contexts.

Table IX gathers the extreme values for MAR when only the dominant harmonic is non-zero.

Unlike the conclusions drawn for the values of RMSd, in the case of MAR computed when one of the harmonics in the pair is 0, the indices of magnitudes within the set of the polluting harmonic were as follows: 11 for the minimum values (except for the value 19.27% of S1, 4-th set, where the ID is 4) and 2 for the maximum values respectively. Therefore, one can conclude that when a single harmonic from an analyzed set is non-zero, the MAR is usually decreasing with the value of the harmonic magnitude.

Computations were also made for cases when both harmonics in a set are non-zero. The results are gathered by Tables X and XI.

One can conclude based on the data from Tables X and XI that when both harmonics from a set act jointly, usually the minimum values of MAR are associated to the highest magnitudes of the dominant harmonic, except for the 4-ts set. On the other hand, the maximum values of

TABLE X.
MINIMUM VALUES FOR MAR FOR BOTH SURFACES ALONG WITH THE INDICES OF MAGNITUDES IN THE SET WHEN BOTH HARMONICS IN THE SET ARE NON-ZERO

	Minimum of MAR – S1		Minimum of MAR – S2	
Set ID	Value [%]	Combination of IDs	Value [%]	Combination of IDs
1	1.9	(11,9)	3.87	(11,3)
2	1.75	(11,11)	5.97	(11,10)
3	2.64	(11,7)	11.7	(11,2)
2	5.03	(3,3)	22.58	(2,11)

TABLE XI.
MAXIMUM VALUES FOR MAR FOR BOTH SURFACES ALONG WITH THE INDICES OF MAGNITUDES IN THE SET WHEN BOTH HARMONICS IN THE SET ARE NON-ZERO

	Maximum of MAR – 1-st surface		Maximum of MAR – 2-nd surface	
Set ID	Value [%]	Combination of IDs	Value [%]	Combination of IDs
1	16.18	(2,2)	19.39	(2,2)
2	15.89	(2,2)	20.77	(2,2)
3	8.57	(2,2)	18.58	(2,2)
4	16.03	(11,2)	25.22	(2,2)

MAR are ussualy associated to the smallest values for both harmonic magnitudes, except for the 4-th set, 1-st surface. Considering the high and close orders of the harmonics clustered in the 4-th set (33-rd harmonic is dominant and paired with the 31-rd harmonic), one can explain the „special" behavior of the error surfaces for this set.

V. CONCLUSION

The extended study presented in this paper addresses the errors which characterize the determination of 4 types of harmonic signals, generated from the following pairs of harmonic orders: (3,5), (7,9), (15,17) and (31,33).

The main conclusions relative to the values of RMSd are:

- when none of the paired harmonics is polluting the test signal, small values were obtained for RMSd , representing at most 0.2% from the fundamental harmonic;
- when a single harmonic H from the set is non-zero, simulations revealed that the RMSd is increasing with the magnitude of H;
- when the harmonics acted jointly, the lowest values for RMSd were associated to the lowest non-zero magnitudes of paired harmonics. As for the maximum values for the RMSd, two possible combinations of indices associated to harmonic magnitudes were identified. The 1-st combination can be translated into „highest magnitude for the dominant harmonic combined with lowest magnitude for the paired harmonic order" whilst the 2-nd one has the meaning „highest magnitudes for both harmonic orders".

Therefore one can consider that highly acceptable RMSd errors were generated.

The main conclusions relative to the phase-shifts associated to the extreme values of RMSd when one of the harmonics is zero are:

- identical values but with oppposite signs were obtained for the sets with IDs 1 and 4;
- at the second set, 2 identical values but with oppposite signs can appear for S1 for different phase-shifts;
- at the 3-rd set, the differences (S1 vs S2) between the counterpart phase-shifts are always $\pi/2$.

When both harmonics were non-zero, many times a sort of separation „above and below" the main diagonal of the matrix in which the magnitudes of dominant harmonic determine the raws and those of the paired harmonic determine the columns could be noticed with respect to phase-shifts. Behavioral patterns could were deduced for each set, being more obvious for sets where the weigth of the dominant harmonic is closer to 1, thus providing better filtering properties.

The analysis of MAR when a single harmonic is non-zero revealed that:

- a sort of „reversed dependence" is established between the values of MAR and the harmonic magnitude;
- smaller differences were noticed between the extreme values of sets with higher IDs (e.g. the difference between the minimum and maximum values of the 1-st set is higher than 46%, whilst its counterpart for the 4-th set is 13%). Actually the MARs associated to the smallest harmonic magnitudes correspond to small absolute values and therefore cannot be considered as significant in these contexts;
- unlike the conclusions drawn for the values of RMSd, the MAR is usually decreasing with the value of the harmonic magnitude.

The analysis of MAR when both harmonics were non-zero revealed that usually the minimum values of MAR are associated to the highest magnitudes of the dominant harmonic, except for the 4-ts set. On the other hand, the maximum values of MAR are usually associated to the smallest values for both harmonic magnitudes, except for the 4-th set, 1-st surface.

Future work will be concerned with the study of errors accompanying the composition/recomposition focusing on clusters of 4 harmonics.

Acknowledgment

Source of research funding in this article:

This paper has received support from the European Union „ Horizon 2020 research and innovation programme" under the Marie Sklodowska-Curie grant agreement No. 812753.

Contribution of authors:
First author – 35%
Second coauthor – 35%
Third coauthor – 20%
Fourth coauthor – 10%
……
Received on July 17,2022
Editorial Approval on November 15, 2022

References

[1] T. Loutas and V. Kostopoulos," Utilising the wavelet transform in condition-based maintenance. A review with applications." Available at https://cdn.intechopen.com/pdfs/ 34959/InTech/Utilising _the_wavelet_transform_in_condition_based_maintenance_a_review_with_applications.pdf, 2012. Retrieved Aug. 2020.

[2] T. Guo, T. Zhang, E. Lim, M. López-Benítez, F. Ma and L. Yu, "A Review of Wavelet Analysis and Its Applications: Challenges and Opportunities," in IEEE Access, vol. 10, pp. 58869-58903, 2022

[3] A. K. Soman and P. P. Vaidyanathan, "Paraunitary filter banks and wavelet packets," in Proceedings of ICASSP-92: 1992 IEEE International Conference on Acoustics, Speech, and Signal Processing, vol. 4, 1992, pp. 397–400 vol.4

[4] I.D. Nicolae, P.M.Nicolae, I.D. Smărăndescu and M.Ş. Nicolae , Wavelet packet transform, a reliable and fast method to obtain the fundamental components required for active filtering in power plants, Proceedings of PEMC 2016, Varna, Bulgaria, Sept. 2016.

[5] I.D. Nicolae, P.M.Nicolae, C.D. Maria and L. Scărlătescu „Evaluating RMS of Linearly Variable Magnitude Waveforms by Using FFT and WPT. Theory and Practice.", Annals of the University of Craiova, Series: Electrical Engineering, no. 40, 2016.

[6] I. D. Nicolae, P. -M. Nicolae and K. Dusan, "Analyzing Electromagnetic Interferences in Power Applications by Using Time-Efficient Joint Analysis Based on DWT and WPT Trees," 2020 International Symposium on Electromagnetic Compatibility - EMC Europe, 2020, pp. 1-6

[7] I.D. Nicolae, P.M. Nicolae, D. Cîrstea, I. Gheorghe, "Optimized use of Wavelet Packet Trees for the analysis of electrical waveforms", DOI: 10.1051/itmconf/20224901006, ITM Web of Conferences, 2022/11/16

[8] S. L. Cristian, M. Ş. Nicolae, P. M. Nicolae, I. D. Nicolae and D. M. Purcaru, "Computational Aspects Concerned with the Optimized Use of Wavelet Package Trees," 2019 International Conference on Electromechanical and Energy Systems (SIELMEN), 2019, pp. 1-6

[9] I. D. Nicolae, K. Dusan, P. –. M. Nicolae and R. -F. Marinescu, "Using Time-Efficient Wavelet Packet Transform Decompositions to Analyze EMC Issues in Transportation Systems," 2021 IEEE International Joint EMC/SI/PI and EMC Europe Symposium, 2021, pp. 597-602

[10] I.D. Nicolae and P. -M. Nicolae, "Practical aspects related to paired nodes and paired harmonics in WPT analysis," IECON 2016 - 42nd Annual Conference of the IEEE Industrial Electronics Society, 2016, pp. 1010-1015